

UCLA

UCLA Electronic Theses and Dissertations

Title

Tuning Magnetic Properties of Soft Ferromagnetic Thin Films for High Frequency Applications

Permalink

<https://escholarship.org/uc/item/4vz5435c>

Author

Rementer, Colin Richard

Publication Date

2017

Peer reviewed|Thesis/dissertation

UNIVERSITY OF CALIFORNIA

Los Angeles

Tuning Magnetic Properties of Soft Ferromagnetic Thin Films for High Frequency Applications

A dissertation submitted in partial satisfaction of the
requirements for the degree Doctor of Philosophy
in Chemical Engineering

by

Colin Richard Rementer

2017

© Copyright by

Colin Richard Rementer

2017

ABSTRACT OF THE DISSERTATION

Tuning Magnetic Properties of Soft Ferromagnetic Thin Films for High Frequency Applications

by

Colin Richard Rementer

Doctor of Philosophy in Chemical Engineering

University of California, Los Angeles, 2017

Professor Jane Pei-Chen Chang, Chair

This work focuses on the design, synthesis, characterization and integration of soft ferromagnetic multilayer structures for their applications in high frequency applications. Presently, the form factor of current telecommunication devices, i.e., antenna, is fundamentally limited by the wavelength it is designed to transmit or receive. In order to adapt to new technologies, a method for subverting this paradigm has been developed by use of magnetoelectric, strain-coupled multiferroic systems, which requires optimized ferroic materials, especially ferromagnetic thin films. Two approaches were considered to achieve this goal, doping (boron) and multilayer (NiFe) heterostructures, where FeGa was selected as the reference phase for both approaches. Doping magnetic materials with boron has been shown to enhance the magnetic softness while maintaining magnetostriction. Multilayer heterostructures offer the possibility of tuning magnetic responses by taking advantage of materials with complementary magnetic properties.

Iron-gallium-boron (FeGaB) was synthesized via co-sputtering of Fe₇₅Ga₂₅ and boron. The addition of boron to Fe₇₅Ga₂₅ reduced the magnetocrystalline anisotropy energy, enhancing the high frequency properties. Magnetometry studies showed that the coercivity was reduced by 70% with 15% boron (at. %) while maintaining 90% of the magnetization of FeGa. Fixed frequency FMR studies showed that the addition of boron reduced the linewidth by up to 70% to a value of 210 Oe. Electrically poled hysteresis measurements showed that the film has a saturation magnetostriction of 50 $\mu\epsilon$. FeGaB's properties were shown to be tunable and can be optimized by controlling the boron concentration within 11-15% but this approach did not yield the desired FMR linewidth.

Multilayers of sputtered Fe₈₅Ga₁₅/Ni₈₁Fe₁₉, or FeGa/NiFe, were examined to tailor their magnetic softness, loss at microwave frequencies, permeability, and magnetoelasticity, leveraging the magnetic softness and low loss of NiFe, and the high saturation magnetostriction (λ_s) and magnetization (M_s) of FeGa. A systematic change was observed as the number of bilayers or interfaces increases: a seven-bilayer structure results in an 88% reduction in coercivity and a 55% reduction in FMR linewidth at X-band compared to a single phase FeGa film, while maintaining a high relative permeability of 700. The magnetostriction was slightly reduced by the addition of NiFe but still maintained up to 70% that of single phase FeGa. Analyses of the domain size revealed that this effect is a function of the layer thicknesses: thinner layers have larger in-plane domains, leading to lower coercivity. The depth-dependent composition and magnetization of these heterostructures as a function of magnetic and electric fields were assessed via polarized neutron reflectometry and the rotation of magnetization of the individual layers with applied strain was found to be deterministic. The tunability of these

magnetic heterostructures makes them suitable candidates for RF magnetic applications requiring strong magnetoelastic coupling and low loss.

Device functionality was assessed by integrating multilayer samples into two different antenna architectures. A surface acoustic wave (SAW) structure was used to determine the magnitude of absorption of acoustic wave energy from piezoelectric LiNbO_3 . Samples with the optimized 5 BL structure, 5 $\text{BL}_{(\text{SAW}1)}$ (50 nm) and 5 $\text{BL}_{(\text{SAW}2)}$ (100 nm), were fabricated and evaluated and absorbed 17 % of the acoustic energy from the strain wave. A bulk acoustic wave (BAW) structure was used to study how the material could convert the energy from an electromagnetic wave into an acoustic wave. A thick 12 $\text{BL}_{(\text{BAW})}$ sample was integrated into a device and showed a low FMR linewidth and high permeability.

This work provided the proof of concept that both doping and interfacial engineering are viable approaches for tuning the magnetic properties of FeGa, and could be extended to other magnetoelastic systems. Multilayer magnetic materials are a promising alternative to single-phase ferromagnetic materials as well as doped material systems for resonator or sensor applications. The low coercivity, high permeability, and high strain sensitivity of these samples make them promising candidates for high frequency, strain-coupled multiferroic systems.

The dissertation of Colin Richard Rementer is approved.

Selim Senkan

Yuanxun (Ethan) Wang

Jane Pei-Chen Chang, Committee Chair

University of California, Los Angeles

2017

TABLE OF CONTENTS

Chapter 1 : Motivation and Background.....	1
1.1 Motivation.....	1
1.2 Antenna Theory and Design	3
1.3 Ferromagnetism	9
1.4 Multiferroic Composites	22
1.5 RF multiferroic systems.....	26
1.6 Scope and Organization	31
Chapter 2 : Experimental Setup	32
2.1 Synthesis	32
2.2 Material Characterization.....	42
2.3 Magnetic Characterization	51
2.4 Multiferroic Device Characterization	68
Chapter 3 : Growth and Characterization of Iron-Gallium-Boron.....	73
3.1 FeGa.....	73
3.2 FeGaB	79
Chapter 4 : Growth and Characterization of FeGa/NiFe Multilayers.....	87
4.1 Growth and Composition.....	87
4.2 Magnetic Properties of FeGa and NiFe Multilayers	92
4.3 Interfacial Magnetism of FeGa and NiFe Multilayers	100
Chapter 5 : Multiferroic Device Characterization	123
5.1 Integration into Surface Acoustic Wave Antenna	123
5.2 Integration into Bulk Acoustic Wave Antenna.....	126
Chapter 6 : Summary	129
Appendix.....	132
A. Operating Procedures.....	132
A.1: Ulvac JSP 8000 Sputtering Tool.....	132
A.2 SQUID Magnetometry	140
A.3 Magneto-optic Kerr Effect (MOKE) spectroscopy.....	144
A.4. Electron Spin Resonance (ESR) Spectroscopy	145
A.4.4. Sample removal and shutdown	147
B. Data Fitting and Extraction	149
B.1. Polarized Neutron Reflectivity.....	149
B.2 Magnetostriction.....	152
Bibliography	156

LIST OF TABLES

Table 1-1. Pertinent functional properties of various ferromagnetic material candidates are summarized for comparison and material selection for integration into a multiferroic antenna. .	29
Table 2-1. Relevant technical specifications of sputter targets used in this work	36
Table 2-2. Description of bilayer configurations of the FeGa/NiFe samples characterized to optimize the structures. All samples were grown on Si and PMN-PT.	38
Table 2-3. Description of the bilayer samples measured via PNR with applied strain. All samples were grown on Si/PMN-PT.	40
Table 2-4. Description of the bilayer samples integrated into the BAW and SAW antenna structures. Samples were grown on Si/PMN-PT as well as the respective antenna structure.	41
Table 2-5. Binding energies and R.S.F factors for Fe 2p, Ga 2p, B 1s, C 1s and O 1s	44
Table 3-1. Changing Fe:Ga ratio with increasing boron content.....	79

LIST OF FIGURES

Figure 1-1. (Left) Radio tower antenna (center) cell phone antenna (right) and nano-scale motor device next to red blood cell (diameter ~micron) for size comparison. A micron-sized antenna would have a frequency of 100s of THz, which is not yet attainable.	2
Figure 1-2. Diagram of in-phase and orthogonal oscillating magnetic and electric components of electromagnetic radiation.....	3
Figure 1-3. Current pattern in (left) a full-wavelength antenna (right) and a half-wavelength antenna with maximum current indicated.....	5
Figure 1-4. Schematic of (left) quarter-wavelength monopole and (right) half-wavelength dipole antennas.....	7
Figure 1-5. Schematic of surface acoustic wave (SAW) device on a piezoelectric substrate with two sets of interdigital transducers (IDTs).....	8
Figure 1-6. Magnetic hysteresis of a ferromagnetic material, showing the coercivity (H_c), remnant magnetization (M_r), permeability (μ), saturation field (H_s) and magnetization (M_s) adapted from (Cullity 2009).....	11
Figure 1-7. Diagram of the magnetic precession of a single domain around the axis of an applied magnetic field (O'Handley 2000).....	14
Figure 1-8. Shape change of a ferromagnetic material having positive magnetostriction with applied field, H	18
Figure 1-9. Crystal structure for Terfenol-D ($Tb_{0.3}Dy_{0.7}Fe_{1.92}$), where the Tb and Dy atoms can occupy the same lattice position.	18
Figure 1-10. Interactions between ferroelectricity, ferromagnetism and ferroelasticity, and the route to control of magnetization through strain polarization. Electric field polarizes a ferroelectric phase (1), which generates a strain in the ferroelectric via the piezoelectric effect (2), which then strains a ferromagnetic phase (3), resulting in a net magnetization (Spaldin 2005).	23
Figure 1-11. Electric-field-induced precessional switching of magnetization in a magnetic tunnel junction (MTJ) (Amiri 2012).....	25
Figure 1-12. Structure of strain-mediated coupled in composite multiferroic systems (Wang 2010).....	26
Figure 2-1. Schematic of the sputtering phenomena where the bias between the substrate and the target combined results in the ionization of argon atoms.	33

Figure 2-2. Schematics of the bilayer structures used to 1) determine the optimal bilayer structure and 2) determine the origin of the thickness-dependent tunability of these structures.....	39
Figure 2-3. Schematics of the four samples grown to study the depth-dependent magnetization rotation with applied strain. The three samples on the left were used to analyze the thickness-dependence of the strain effect and the sample on the right is a super lattice, like what would be incorporated into a device.....	40
Figure 2-4. Bilayer samples measured in (left) surface acoustic wave (SAW) measurements and (right) bulk acoustic wave (BAW) measurements.....	41
Figure 2-5. A schematic illustration of emission of a photoelectron by the x-ray with an incident kinetic energy of $h\nu$, from the 1s orbital.....	42
Figure 2-6. XPS survey scan from 1200 – 0 eV of a 100 nm $\text{Fe}_{76}\text{Ga}_{22}\text{B}_{12}/\text{Si}$ film with major elemental peaks identified.....	43
Figure 2-7. XPS detail spectra of Ga 2p peak with increased sputtering time, resulting in the removal of native Ga_2O_3 oxide for a FeGa/NiFe multilayer sample with the structure (20 nm $\text{FeGa}/15$ nm NiFe) ₃ /20 nm FeGa/Si	45
Figure 2-8. (Left) Schematic of Bragg diffraction in a single crystal and (right) XRD scan of a 100 nm $\text{Fe}_{60}\text{Ga}_{25}\text{B}_{15}$ with the Fe [110] peak indicated.	47
Figure 2-9. Schematic of contact profilometry of a thin film.	47
Figure 2-10. Normalized thickness data taken using profilometer for $\text{Fe}_{75}\text{Ga}_{25}/\text{Si}$ corresponding to a thickness of 50 nm.	48
Figure 2-11. Illustration of atomic force microscopy, where the small deflections in the position of the cantilever are captured by the change in position of a laser.	49
Figure 2-12. (Left) Normalized AFM image of a 50 nm FeGaB film deposited on Si over a $1 \mu\text{m}^2$ area and (right) an extracted line scan.	50
Figure 2-13. Schematic of a room temperature MOKE spectroscopy system set up for measuring in-plane magnetization.....	52
Figure 2-14. Normalized magnetic hysteresis for 200 nm $\text{Fe}_{60}\text{Ga}_{22}\text{B}_{18}/\text{Si}$, with the coercivity H_C and saturation field H_S indicated on the plot.	53
Figure 2-15. Image of the magnetic domains in a (5.5 nm $\text{FeGa}/6.3$ nm NiFe) ₈ /5.5 nm FeGa/Si sample indicating domain size of 100 μm or larger.....	54
Figure 2-16. SQUID loop made of a superconductor with two Josephson junctions separated by thin insulators.....	55

Figure 2-17. Normalized in-plane magnetic hysteresis for a 100 nm Fe ₆₅ Ga ₂₀ B ₁₅ /Si with H _c , H _s and M _s indicated.	58
Figure 2-18. Schematic of vibrating sample magnetometry with sample centered between pickup coils placed on the faces of the poles of the magnet.....	59
Figure 2-19. Normalized in-plane hysteresis measurement of a 25 nm FeGa/50 nm NiFe/25 nm FeGa/Si sample measured by VSM with coercivity, saturation magnetization and field indicated.	60
Figure 2-20 Precessional motion of an electron under an applied magnetic field.....	61
Figure 2-21. ESR spectra for Fe ₆₅ Ga ₂₀ B ₁₅ (100nm)/Si, where the resonance field is around 600 Oe and linewidth is 350 Oe.....	63
Figure 2-22. Schematic of stripline measurement system for frequency-dependent permeability measurements.....	64
Figure 2-23. Individual permeabilities of the cavity/substrate/film in terms of an effective permeability.	65
Figure 2-24. Schematic of polarized beam reflectometry setup at the National Institute for Standards and Technology's Center for Neutron Research (NCNR) <i>image courtesy of NCNR</i> . .	66
Figure 2-25. Schematic sample position (left) non-spin flip (center) and spin-flip scattering (right) occurring in PNR experiments. Each layer has a nuclear and magnetic scattering length density (ρ or SLD) and the angle of magnetization ($\theta_{\text{magnetization}}$) is determined by fitting the model.....	67
Figure 2-26. (Left) Fitted reflectivity for a 25 nm FeGa/50 nm NiFe/25 nm FeGa sample and (right) the corresponding scattering length density profile generated from the fit.	68
Figure 2-27. (Left) Schematic of ferromagnetic thin film deposited on PMN-PT (011) substrate and (right) normalized strained and unstrained hysteresis loops for a 25 nm FeGa/50 nm NiFe/25 nm FeGa sample.	69
Figure 2-28. (Left) Schematic of ADFMR in a ferromagnetic material grown on LiNbO ₃ and (right) a plot of the absorption of that acoustic wave as a function of applied magnetic field in the X and Y directions (Labanowski 2016).....	70
Figure 2-29. (Left) Schematic of cross-section of BAW stack in an antenna and (right) a top down SEM image of the BAW resonator device.....	72
Figure 3-1. XPS survey scan of a 100 nm Fe ₇₅ Ga ₂₅ /Si sample with elemental peaks indicated.	74
Figure 3-2. In-plane and out-of-plane magnetic hysteresis of a 200 nm Fe ₇₅ Ga ₂₅ /Si (right is magnified to show coercivity).	75

Figure 3-3. ESR spectra of a 200 nm Fe ₇₅ Ga ₂₅ /Si film with a FMR linewidth of 750 Oe.	76
Figure 3-4. FMR linewidth as a function of sputtering pressure of argon for 35 nm Fe ₇₅ Ga ₂₅ /Si films.	77
Figure 3-5 Magnetic hysteresis measured by MOKE of Fe ₇₅ Ga ₂₅ (70 nm)/Ta (10 nm)/PMN-PT [001]/ Ni (20 nm) with applied voltages.	77
Figure 3-6. Strained and unstrained hysteresis of a 300 nm Fe ₈₅ Ga ₁₅ sample with (left) a residual stress of +40 MPa and (right) a residual stress of +800 MPa.	79
Figure 3-7. In-plane and out-of-plane magnetic hysteresis of 200 nm Fe ₆₈ Ga ₂₆ B ₁₄ /Si (the right plot is magnified to show coercivity).....	80
Figure 3-8. Magnetic hysteresis of 100 nm thick FeGaB films at 11%, 15%, and 19% boron content.	81
Figure 3-9. Magnetic hysteresis of Fe ₆₅ Ga ₂₀ B ₁₅ at 30, 50, and 100 nm thicknesses.	82
Figure 3-10. Summarized composition and thickness dependent magnetic hysteresis properties for FeGaB (B=11-19%) thin films (30-100nm).....	83
Figure 3-11. ESR spectra of 100 nm FeGaB/Si with 11%, 15% and 19% boron concentration..	84
Figure 3-12. Summary of FMR linewidth data for FeGaB samples with boron doping at 11%, 15% and 19% at film thicknesses of 30, 50 and 100 nm.	85
Figure 3-13. Strained and unstrained hysteresis of a 100 nm Fe ₆₅ Ga ₂₀ B ₁₅ corresponding to a saturation magnetostriction of 50 $\mu\epsilon$	86
Figure 4-1. Residual stress optimization for (left) sputtering pressure and (right) power for 60 nm FeGa and NiFe films grown on Si (100).....	88
Figure 4-2. Growth rates for FeGa and NiFe as a function of (left) sputtering pressure and (right) power.....	89
Figure 4-3. XPS spectra for 3 BL FeGa/NiFe sample with increasing etch time, showing the appearance of the Ni 2p peak and attenuation of the Ga 2p peak.	90
Figure 4-4. X-ray diffraction data for the 1 – 7 BL FeGa/NiFe samples with major peaks for FeGa and NiFe identified.....	91
Figure 4-5. Grain size (left axis) of the major FeGa (110) and NiFe (111) peaks and layer thickness (right axis) as a function of the number of bilayers in 100 nm samples.	92
Figure 4-6. Hysteresis loops of single phase FeGa, NiFe and a 5 BL sample with the structure (8.5 nm FeGa/10 nm NiFe) ₅ /8.5 nm FeGa.....	93

Figure 4-7. ESR spectra of single phase FeGa, NiFe and a 5 BL sample with the structure (8.5 nm FeGa/10 nm NiFe) ₅ /8.5 nm FeGa.	94
Figure 4-8. Coercivity and FMR linewidth at X band as a function increasing number of bilayers (decreasing layer thickness).	95
Figure 4-9. Extracted (left) real and (right) imaginary permeability for a 5 BL sample (8.5 nm FeGa/10 nm NiFe) ₅ /8.5 nm FeGa multilayer with increasing magnetic bias.	96
Figure 4-10. Saturation magnetostriction (left axis) and saturating field (right axis) as a function of number of FeGa/NiFe bilayers (decreasing layer thickness).	97
Figure 4-11. (Left) ESR spectra for a 3 BL sample and (right) FMR linewidth and resonant field as a function of electric field.	99
Figure 4-12. (Left) ESR spectra of 2 BL sample and (right) FMR linewidth and resonant field as a function of electric field.	100
Figure 4-13. (Left) In-plane magnetization and (right) ESR spectra for a 3 BL sample with 1:1 FeGa:NiFe ratio.	101
Figure 4-14. (Left) In-plane magnetization and (right) ESR spectra for a 3 BL sample with 4:1 FeGa:NiFe ratio.	102
Figure 4-15. (Left) In-plane magnetization and (right) ESR spectra for a 3 BL sample with 9:1 FeGa:NiFe ratio.	103
Figure 4-16. In-plane sample orientations measured for 1 B _(PNR) and 8 BL _(PNR)	104
Figure 4-17. (Left) Fitted reflectivity and (right) ρ_{magnetic} and ρ_{nuclear} profiles for a 1 BL _(PNR) sample with a 1000 Oe magnetic field applied in plane.	105
Figure 4-18. (Left) Fitted reflectivity and (right) ρ_{magnetic} and ρ_{nuclear} profiles for a 1 BL _{PNR} sample rotated 90° with respect to the applied field of 1000 Oe in plane.	106
Figure 4-19. (Left) In-plane magnetic hystereses for 1 BL _(PNR) sample showing in-plane anisotropy (center) domain size in 1 BL _(PNR) sample in original orientation on the order of 10s of μm and (right) domain size of the sample rotated 90° on the order of 100s of μm , indicating in-plane anisotropy.	107
Figure 4-20. (Left) Fitted reflectivity (right) and ρ_{magnetic} and ρ_{nuclear} profiles for an 8 BL _(PNR) sample with a 1000 Oe magnetic field applied in plane.	107
Figure 4-21. (Left) Fitted reflectivity (right) and ρ_{magnetic} and ρ_{nuclear} profiles for an 8 BL _(PNR) sample rotated 90° with respect to the applied field of 1000 Oe in plane.	108

Figure 4-22. (Left) In-plane magnetic hystereses for 8 BL _(PNR) sample showing similar coercivities, (center) domain size in 8 BL _(PNR) sample in original orientation and (right) rotated 90° with domain sizes on the order of 100s of μm.	109
Figure 4-23. Deviation in angle of magnetization from the applied magnetic field for the (left) 1 BL _(PNR) sample and (right) 8 BL _(PNR) sample for both orientations.	110
Figure 4-24. Unstrained and strained magnetic hysteresis of (left) 7 nm NiFe sample, (center) 20 nm NiFe sample, and (right) 40 nm NiFe sample with a base layer of 20 nm FeGa, all deposited on pre-poled 50 nm Pt/5 nm Ti/PMN-PT (011)/10 nm Ti/125 nm Au substrates	111
Figure 4-25. Out-of-plane magnetization measurements for the bilayer sample with (left) 7 nm NiFe, (center) 20 nm NiFe, and 40 nm NiFe (right) with a base layer of 20 nm FeGa grown on Si (100).	112
Figure 4-26. (Left) Fitted reflectivity (right) and the corresponding ρ _{magnetic} and ρ _{nuclear} profiles for 7 nm NiFe, 20 nm NiFe and 40 nm NiFe samples with a base layer of 20 nm FeGa grown on 50 nm Pt/5 nm Ti/PMN-PT (011)/10 nm Ti/125 nm Au substrates	113
Figure 4-27. (Left) Fitted remnant reflectivity (right) the corresponding magnetization rotation at 0 and 400 V for the 7 nm NiFe, 20 nm NiFe and 40 nm NiFe bilayer samples.	115
Figure 4-28. Magnetic hysteresis of a 3 BL sample with the structure (20 nm FeGa/7 nm NiFe) ₃ /20 nm FeGa/Si.....	116
Figure 4-29.(Left) Non-spin flip reflectivity measurements for (20 nm FeGa/7 nm NiFe) ₃ /20 nm FeGa/Si and (right) the corresponding ρ _{magnetic} and ρ _{nuclear} profiles.	117
Figure 4-30. Spin-flip (R ₊₋ and R ₋₊) and non-spin flip (R ₊₊ and R ₋₋) spectra and fits (left) and a schematic of the rotation of the magnetization vector at 10 Oe.	118
Figure 4-31. (Left) Reflectivity measurements on (20 nm FeGa/7 nm NiFe) ₃ /20 nm FeGa/50 nm Pt/5 nm Ti/PMN-PT (011)/10 nm Ti/125 nm Au) (right) and the corresponding ρ _{magnetic} and ρ _{nuclear} profiles.	119
Figure 4-32. Poled magnetic hysteresis measurements with (left) strain parallel to the applied magnetic field and (right) perpendicular to the applied magnetic field.	120
Figure 4-33. (Top) Spin-flip scattering for FeGa (20 nm FeGa/7 nm NiFe) ₃ /20 nm FeGa superlattice as a function of applied voltage (bottom) and the corresponding magnetization rotation in two different sample positions.	121
Figure 4-34. Degree of magnetization of rotation with electric field for the cases of (left) strain parallel to the applied magnetic field and then (right) rotated by 45°.	122
Figure 5-1. (Left) In-plane and (right) out-of-plane hysteresis loops for a (4.2 nm FeGa/5 nm NiFe) ₅ /4.2 nm FeGa (5 BL _(SAW1)) sample that shows perpendicular magnetic anisotropy.	124

Figure 5-2. In-plane (left) and out-of-plane (right) hysteresis loops for a (8.3 nm FeGa/10 nm NiFe)₅/8.3 nm FeGa sample (5 BL_(SAW2)) that shows exchange-spring behavior. 124

Figure 5-3. Absorption of acoustically driven FMR spectra as a function of X and Y components of magnetization for a (4.2 nm FeGa/5 nm NiFe)₅/4.2 nm FeGa sample. 125

Figure 5-4. Absorption of acoustically driven FMR spectra as a function of X and Y components of magnetization for a (8.3 nm FeGa/10 nm NiFe)₅/8.3 nm FeGa sample. The dashed lines are a visual guide for the 4-fold lobes. 126

Figure 5-5. In-plane magnetic hysteresis of a (25 nm FeGa/5 nm NiFe)₁₂/25 nm FeGa with a coercivity of 4 Oe and a saturation magnetization of 1180 emu/cc. 127

Figure 5-6. Broadband permeability measurement of a (25 nm FeGa/5 nm NiFe)₁₂/25 nm FeGa sample at a bias field of 93 Oe (left) and a variable field measurement at 3.5 GHz (right). 128

ACKNOWLEDGEMENTS

I would like to start by thanking Professor Chang for her mentorship over the past five years. She provided a unique Ph.D. experience that has made me a capable researcher. Her insight and intuition have shaped the way that I approach research and how I am able to communicate it. Thank you to Professor Wang, Professor Senkan and Professor Segura for serving on my committee.

I've been very lucky to have labmates that are not only incredibly smart, but also incredibly kind. Ryan and Ernest, I'm very impressed by both the depth and breadth of your knowledge – I've no doubt you will have great success in your doctoral work. Jeff, thank you for numerous discussions about magnetism over the years – I always end up learning something new after talking to you. Nick, you're a rare combination of intelligence and charisma – don't forget that. Kevin, thank you for all of your help with my project. Your dedication to research as well as education and mentoring are unparalleled. You've got a special mind. To Dr. Vladan Jankovic, Dr. Jay Cho, Dr. Taesung Kim, Dr. Jack Chen, and Dr. Younghee Kim – thank for your mentorship and friendship. Finally, to my good friend, Cyrus: going through this process with you made everything bearable, and dare I say, fun.

Thank you to all of my collaborators over the years. Professor Carman, Professor Wang, and Professor Tolbert – your intelligence combined with ability to teach helped me immensely while learning about magnetism. Thank you to all of my collaborators at the National Institute of Standards and Technology's Center for Nuclear Research, specifically Dr. Michelle Jamer, Dr. Brian Kirby, Dr. Julie Borchers, Dr. Alex Grutter and Dr. Daniel Gopman. Thank you all for sharing your extensive knowledge with me and helping me develop a more thorough understanding of my project.

I couldn't have done this without the support of my friends. John and Nako – you've been with me from the beginning and I couldn't ask for better friends. To my good friend Kevin J – from the bottom of my heart, thank you for everything. To Lily, my partner, you've helped me in ways I don't have the ability to convey. Thank you.

I dedicate this dissertation to my family. My parents, Richard and Victoria, who put me before themselves at every opportunity, thank you for the sacrifices you made. To my best friend, my brother Cameron – thank you for your support and friendship. I know I couldn't have done this without you. To my uncle, Stan – thank you for everything, and I love you.

VITA

2012 B. Sc., Chemical Engineering
B. Arts, Women's and Gender Studies
Lafayette College
Easton, PA

2012-2017 Graduate Student Research
Department of Chemical Engineering
University of California, Los Angeles
Los Angeles, CA

AWARDS

2012 Luther F. Witmer Prize in Materials Science
Carl J. Staska Prize in Chemistry
Lafayette College

PUBLICATIONS AND PRESENTATIONS

C.R. Rementer, K. Fitzell, Q. Zu, P. Nordeen, Y. Wang, G.P. Carman, J.P. Chang, "Tuning the static and dynamic properties of FeGa/NiFe multilayers," *Applied Physics Letters* **110**, 242403 (2017).

C.R. Rementer, M. Jamer, J. Borchers, A. Grutter, B.J. Kirby, Q. Zu, P. Nordeen, G.P. Carman, Y. Wang J.P. Chang, "Probing the depth dependent magnetization of FeGa/NiFe multilayers using polarized neutron reflectometry," in *Magnetism and Magnetic Materials Conference*, New Orleans, Louisiana, USA, Nov 2016.

C.R. Rementer, Q. Zu, P. Nordeen, Y. Wang, G.P. Carman, and J.P. Chang, "Tuning static and dynamic magnetic properties of FeGa/NiFe multilayer heterostructures via magnetic anisotropy dispersion," in *American Vacuum Society Conference*, Nashville, Tennessee, USA, Nov 2016.

C.R. Rementer, Q. Zu, P. Nordeen, Y. Wang, G.P. Carman, and J.P. Chang, "Tuning static and dynamic magnetic properties of FeGa/NiFe multilayer heterostructures," in *International Materials Research Congress*, Cancun, Quintana Roo, MX, Aug 2016.

C.R. Rementer, K. Fitzell, Q. Zu, P. Nordeen, Y. Wang, G.P. Carman, and J.P. Chang, "Tuning static and dynamic magnetic properties of FeGa/NiFe multilayer heterostructures," in *Joint MMM-Intermag Conference*, San Diego, CA, USA, Jan 2016.

C.R. Rementer, K. Fitzell, Q. Zu, P. Nordeen, Y. Wang, G.P. Carman, and J.P. Chang, "Tuning static and dynamic magnetic properties of multilayer composites," in *American Vacuum Society Conference*, San Jose, CA, USA, Oct 2015.

C.R. Rementer, Y. Kim, D. Shuminer, and J.P. Chang, “Thickness Dependence of High Frequency Magnetic Properties for Thin Films of Iron-Gallium-Boron,” in American Vacuum Society Conference, Baltimore, MD, USA, Nov 2014.

Chapter 1 : Motivation and Background

The prospect of reducing the size of modern antennas by converting an incident electromagnetic wave to an acoustic wave using the strain-coupled multiferroic effect was motivated. A background of the fundamental physics, including electromagnetic radiation as well as different architectures and parameters of modern antennas was introduced. The concepts important for understanding these magnetoelectric systems, such as ferromagnetism and multiferroic materials, specifically high frequency multiferroic systems, were introduced and discussed. Finally, a literature review of applications of both doped and multilayered ferromagnetic materials was presented, motivating the integration of such materials into strain-coupled multiferroic systems.

1.1 Motivation

Since the first computer message was sent in 1969, from UCLA to Stanford, the internet has served a variety of purposes, from a means of communication, to data storage for vast quantities of information. However, the ability of the internet to connect people to that data, or people to each other, is reliant on the antenna. This device has existed in many forms since its invention in the late 19th century, such as the radio tower or the cell phone antenna, and arguably the largest innovation since then has been the integration of antenna onto circuit boards. The reason that antennas have not undergone a scaling revolution similar to transistors following Moore's law is that their size is dictated by the wavelength of the electromagnetic wave, as shown in Figure 1-1.

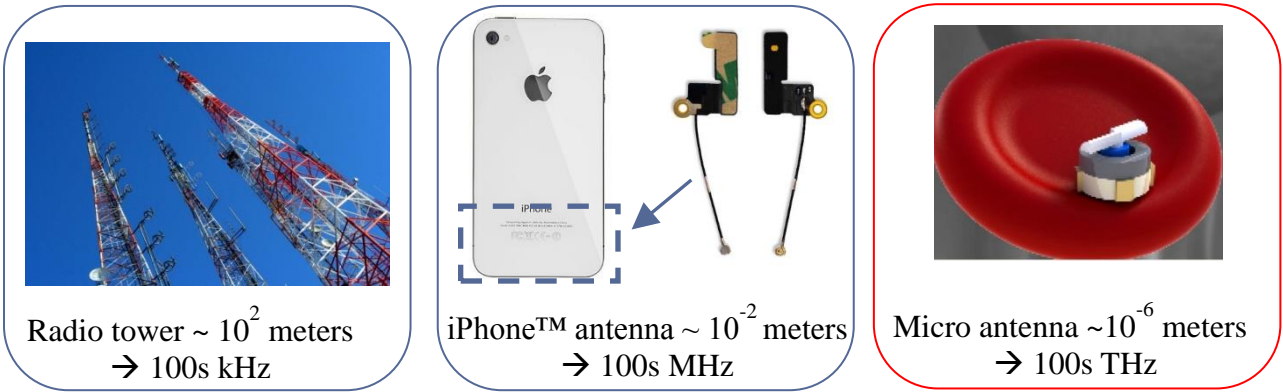


Figure 1-1. (Left) Radio tower antenna (center) cell phone antenna (right) and nano-scale motor device next to red blood cell (diameter \sim micron) for size comparison. A micron-sized antenna would have a frequency of 100s of THz, which is not yet attainable.

Electrically small micro or nano-antennas are an exciting prospect, especially with the development of the idea of the Internet of Things, where small devices, such as wearable technology, could be connected to create an ecosystem of information. Bluetooth antennas would be the likely point of connection for such devices, which operate at a frequency of 2.4 GHz, corresponding to a wavelength of 12.5 cm, much larger than a red blood cell. In fact, for an antenna smaller than 10^{-6} meters the corresponding frequency is 300 THz, which is readily absorbed by the Earth's atmosphere.

The approach described in this chapter subverts that fundamental limitation by using the speed of sound in a solid, rather than the speed of light in a vacuum as the controlling factor, which allows for a 1 GHz wave (0.3 meter wavelength) to be converted into an acoustic wave, reducing the wavelength by five orders of magnitude. The approach utilizes materials that can interact with the wave via strain-coupling, which is the focus of this work.

1.2 Antenna Theory and Design

Electromagnetism, one of the fundamental natural forces, describes the interaction between electricity, the flow of electrons, and magnetism, and their spins. Electromagnetic radiation (EMR) is a fundamental property that describes wave-particle duality of photons. Figure 1-2 shows a linearly polarized EM wave, with the magnetic and electric components lying in phase and 90 degrees of one another.

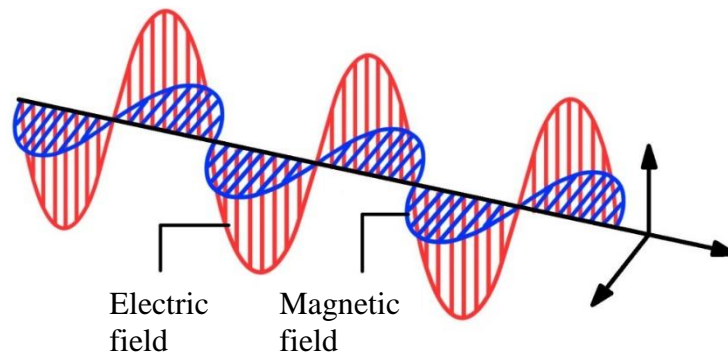


Figure 1-2. Diagram of in-phase and orthogonal oscillating magnetic and electric components of electromagnetic radiation.

EMR can be described fundamentally in terms of its wavelength and frequency, which are inversely related, as shown in equation (1.1), where c is the speed of light.

$$c = f\lambda \quad (1.1)$$

The EMR spectrum ranges from radio waves, which are long wavelength (meters) and low frequency (kHz), to gamma rays, which are short wavelength (picometers) and high frequency (10^{19} Hz), as well as the spectrum of visible light, which ranges from a wavelength of 400-700 nm.

Global communications uses a subset of these frequencies called the radio frequency (RF) spectrum. The RF spectrum includes frequencies below 300 GHz, or 1 mm wavelength, because at higher frequencies, the EMR is absorbed by the Earth's atmosphere. Within this range

of frequencies, there are subsets that have different uses. For instance, radios most commonly operate in the kHz to MHz range, a cell phone operates in the MHz range, and a home Wi-Fi connection operates in the GHz range. Antennas enable the transmission and reception of EM waves of various frequencies across the globe.

1.2.1 Antenna Design

The first antenna was developed by an Italian engineer, Guglielmo Marconi, in 1895. His device, a monopole antenna, consisted of an elevated copper sheet connected to RF signal generator, which was powered via induction coil and was used to transmit Morse code. This discovery revolutionized the way in which people across the globe could communicate, as previously, communication was dependent upon long stretches of cables, such as in the transatlantic cable laid in 1858.

Most antennas are sized at half of the wavelength or less because the current flow in a full wavelength antenna would change in direction along the length and have a maximum towards the end of the antenna, as shown in Figure 1-3. For this reason, half-wavelength antennas are more efficient than full-wavelength antennas, and this can be extended down to even fractions of the wavelength, though there is some loss of bandwidth as the volume is decreased.

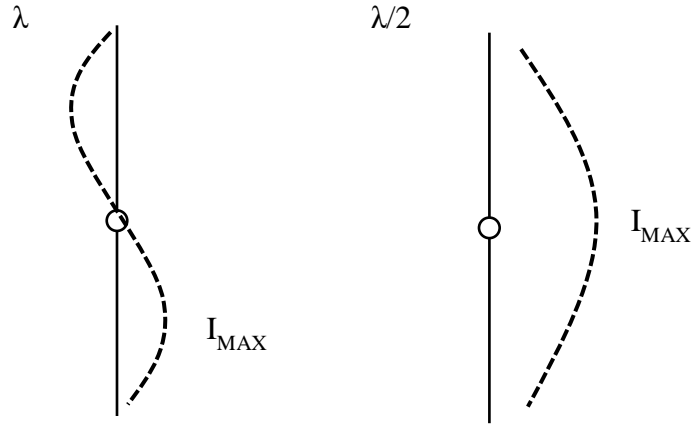


Figure 1-3. Current pattern in (left) a full-wavelength antenna (right) and a half-wavelength antenna with maximum current indicated.

Most antenna power (P) characteristics are represented in log scale (L_P), which is useful for representing the ratio of very large and very small power quantities. For example, a power ratio of 0.5 would correspond to 3 dB and a power ratio of 0.0000005 would correspond to -63 dB. Since this quantity is determined by a ratio, there are several specific units in dB that indicate a reference value: dBm has a reference value of 1 mW and dBi uses an isotropic reference source.

$$L_P = 10 \log_{10} \left(\frac{P}{P_0} \right) \quad (1.2)$$

The quality of an antenna (E_R) is determined by several governing parameters that influence the design considerations. The efficiency of an antenna is determined by the ratio of the power radiated (P_{radiated}) from the antenna to the input power (P_{input}). Efficiency for a half-wavelength dipole antenna measured in an anechoic chamber is over 90%.

$$E_R = \frac{P_{\text{radiated}}}{P_{\text{input}}} \quad (1.3)$$

The directivity of an antenna (D) is a measure the angle-dependence of the antenna's radiation pattern. It is represented by the ratio of the angle-dependent radiation intensity (U) to

the total power emitted by the antenna (P_{tot}). Higher directivity would be desirable for satellites, where the direction and position have a large impact on the strength of the signal. On the other hand, a cell phone antenna should have less directionality, as it should be able to receive a signal from many different angles (Stutzman 2013).

$$D(\theta, \phi) = \frac{U(\theta, \phi)}{P_{tot}/(4\pi)} \quad (1.4)$$

The directionality and efficiency together dictate the gain of an antenna (G), which indicates how well an antenna can convert an input power to a directed EM wave. It combines the antenna's directivity, the ability to transmit a wave in a specific direction, with its electrical efficiency, how much of the input power can be converted to the wave. The gain of an antenna is most commonly reported in dBi, relative to an isotropic radiator. A half wave monopole antenna has a gain of 2.15 dBi.

$$G = E_R \cdot D(\theta, \phi) \quad (1.5)$$

The bandwidth of an antenna refers to the range of frequency bands it can receive. This value is largely dependent on shape of the antenna, which influences its characteristics. For instance, a dipole antenna with a center frequency of 1000 MHz could have a bandwidth of 8%, meaning that usable range of frequencies is 960 – 1040 MHz. A spiral antenna with a center frequency at 1000 MHz could have a bandwidth as high as 180%, corresponding to a frequency range from 95 – 1900 MHz. The difference between these two is based on the design: due to the shape of a spiral antenna, the polarization, radiation pattern and impedance remain constant for a larger range of frequencies compared to a dipole antenna. Changing the design of the antenna impacts its bandwidth, but another approach is to adjust the size. As the antenna size shrinks,

both bandwidth and efficiency decrease, so the design of antennas is a compromise of size, bandwidth, efficiency, and therefore, gain.

Frequency-modulated (FM) radio operates within the frequency band ranging from 88 - 108 MHz (3.4 – 2.7 meters). The most recognizable antenna, the whip antenna commonly found on cars, is an example of a monopole antenna, consisting of a straight, conductive rod attached to a ground plane, shown in Figure 1-4. The monopole antenna is a resonant antenna, meaning that it receives the signal and creates standing waves of current and voltage throughout the length. A half-wavelength dipole antenna, shown on the right, has the advantage of having a larger radiation pattern compared to the monopole antenna.

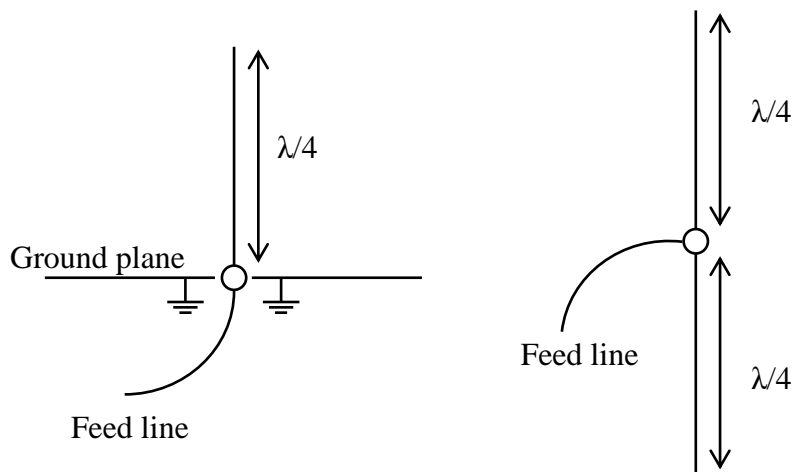


Figure 1-4. Schematic of (left) quarter-wavelength monopole and (right) half-wavelength dipole antennas.

There are currently over seven billion cell phones in use in the world with at least one antenna in each phone. Cell phones utilize a dipole antenna, where the signal is received or transmitted at the center of the conductive rod. More specifically, they use an off-center dipole antenna to be able to cover two distinct frequency bands. The lower frequency band, usually around 800 MHz, corresponds to a wavelength of 37 cm and a half wavelength of 16.5 cm. This means that the low band (~700 MHz) antenna has to be spread over the entire device, while the

high band (>2000 MHz) fits in a smaller area. The footprint of these antennas is a large design consideration of the phone and because of this, there is a strong drive to explore alternative methods for reducing the size of antennas. One potential candidate relies on strain-coupled multiferroic materials, where a magnetostrictive ferromagnet is coupled to a piezoelectric material.

1.2.2 Surface Acoustic Wave Antennas

The fundamental operation of the multiferroic antenna depends on the conversion of an electromagnetic wave to an acoustic wave. A surface acoustic wave (SAW) was first proposed by Lord Rayleigh in 1895 to describe the propagation of the surface acoustic mode, specifically called Rayleigh waves. These are waves that propagate along the surface of solids. The most common way to produce an acoustic wave in a solid is via electric field applied to a piezoelectric substrate, such as quartz or LiNbO₃. A common application for SAW devices are filters, where an applied EM wave can be converted into an electrical signal (Stutzman 2013). A simple diagram of this can be seen in Figure 1-5.

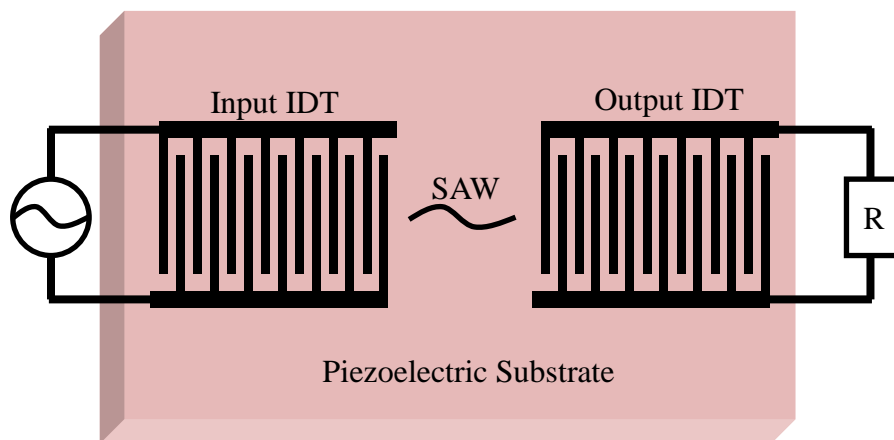


Figure 1-5. Schematic of surface acoustic wave (SAW) device on a piezoelectric substrate with two sets of interdigital transducers (IDTs).

Interdigital transducers (IDTs) on the surface are spaced to match the wavelength of the SAW in the material. The wavelength of the SAW is dictated by the speed of sound in the material and the frequency of the incident EM wave.

$$\lambda_{AW} = \frac{v_{substrate}}{\lambda_{EM}} \quad (1.6)$$

Using equation (1.6), for a piezoelectric material LiNbO_3 , with a 1 GHz EM wave with a full wavelength of 30 cm, the acoustic wavelength is $3.97 \mu\text{m}$, which is 5 orders of magnitude smaller than the EM wave. SAW devices are currently used as filters in cell phones, where an electrical signal can be delayed via transduction into a mechanical wave in the piezoelectric material. A multiferroic SAW antenna would operate in a similar manner with one set of IDTs replaced with a magnetic material that would strain when excited by incident electromagnetic wave.

1.3 Ferromagnetism

The ferromagnetic properties discussed in this section are critical to the operation of a multiferroic antenna, separated into two broad categories: magnetic loss/softness and magnetomechanical coupling. The ideal material for a strain-coupled multiferroic antenna would have low loss, high magnetomechanical coupling, and be magnetically soft. These properties are discussed in the following sections.

1.3.1 Magnetic Ordering

The origin of magnetic ordering lies in the orbital arrangement of individual atoms. The valence shell of an electron is commonly associated with bonding when they lie in the outermost

shell. However, for some elements, the valence electrons lie in second-most outer shell, and it is these elements that exhibit a strong magnetic moment. Elements in the 3d and 4f groups, select transition metals and lanthanides, respectively, tend to exhibit large magnetic moments. Ferromagnetism broadly describes the phenomena where a material undergoes a spontaneous magnetization. A material is ferromagnetic if all of the magnetic moments of the atoms contribute to the positive magnetization. If some of the magnetic moments contribute negatively, but there is still a net magnetization, the material may be called ferrimagnetic. These types of magnetic ordering are temperature dependent: for ferro/ferromagnetic materials, the Curie temperature (T_C) is the temperature above which the material loses its magnetic ordering. Magnetic hysteresis is a property of ferromagnetic materials, where a magnetization induced by an applied field does not reduce to zero as the applied field does (Spaldin 2003). An example of a hysteresis loop for a ferromagnetic material can be seen in Figure 1-6.

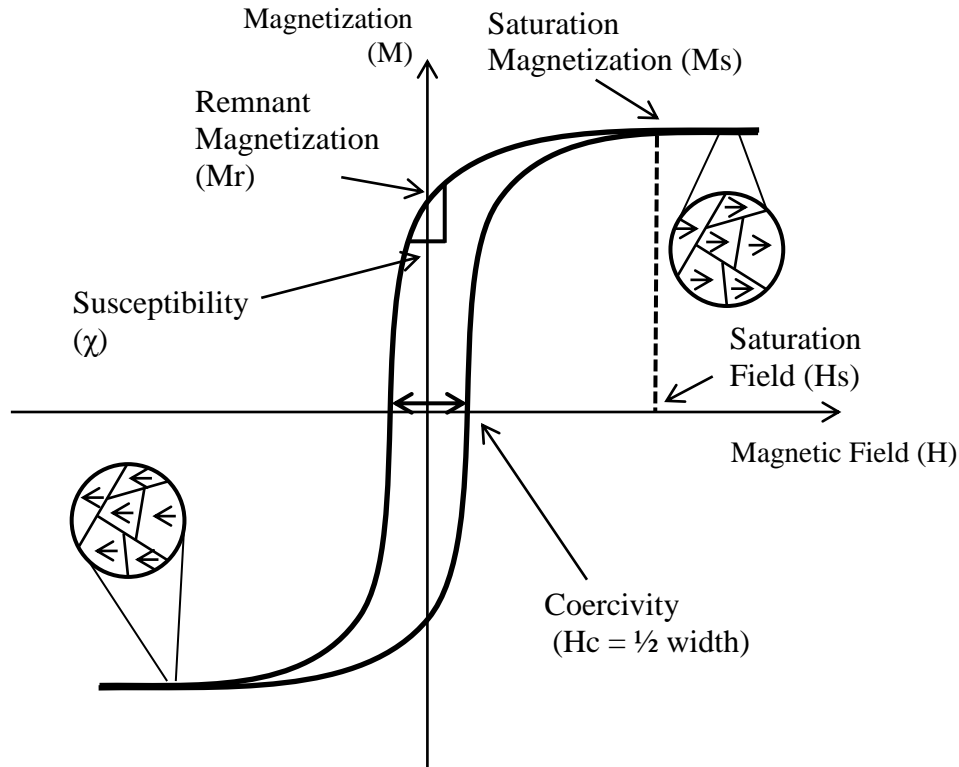


Figure 1-6. Magnetic hysteresis of a ferromagnetic material, showing the coercivity (H_c), remnant magnetization (M_r), permeability (μ), saturation field (H_s) and magnetization (M_s) adapted from (Cullity 2009).

To generate a hysteresis loop, a magnetic field (H), must be applied to a material, and then either the magnetic induction (B) or the magnetization (M) is measured. Magnetic induction and magnetization are both functions of the applied field and equations (1.7) and (1.8) describe the relationships between B , M , and H :

$$B = \mu H \quad (1.7)$$

$$M = \chi H \quad (1.8)$$

The relative permeability (μ) represents the materials ability to sustain a magnetic field in its interior, while the susceptibility (χ) indicates how responsive the magnetization of the material is when a magnetic field is applied. These quantities are related by equation (1.9).

$$\frac{\mu}{\mu_0} = 1 + \chi \quad (1.9)$$

The permeability of free space, represented by $\mu_0 = 4\pi \times 10^{-7} \text{ V}\cdot\text{s}/(\text{A}\cdot\text{m})$, is a fundamental quantity in Maxwell's equations. In SI units, the susceptibility is unitless and permeability has units of H/m.

Saturation magnetization represents the point where all magnetic domains have flipped their states, and \mathbf{M} no longer increases with increasing fields. The saturation field is the field value at which saturation magnetization lies. It should be noted that although the magnetization does not increase, the induction continues to increase according to the following equation.

$$\mathbf{B} = \mathbf{H} + 4\pi\mathbf{M} \quad (1.10)$$

The coercivity is the field required to reduce the magnetic induction to zero. It is represented by half the width of the hysteresis loop at zero induction. The value of coercivity determines whether a material is considered a hard or soft magnet. A hard magnet requires a large field for saturation, and thus harder to demagnetize, while a soft magnet is easily saturated, but easily demagnetized (Cullity 2009).

1.3.2 Exchange Interactions

Exchange interactions in ferromagnetic materials describe several ways in which identical domains in different materials can influence each other over short distances on the order of the exchange length ($\sim \text{nm}$). Exchange-coupling of ferro- or ferri- magnetic materials is a phenomena that occurs when two magnetic materials are interfaced with one another. There are several mechanisms for these interactions, governed by the Coulomb repulsion of electrons in the materials. Direct exchange is the overlap of two atomic orbitals, giving rise to anti-parallel coupling when interatomic distances are small, and parallel coupling when the distances are

large. This type of coupling is effective only for short distances, however, it elucidates the interactions between magnetic domains in ferromagnetic transition metals and their alloys. These interactions allow for the spontaneous magnetization of a ferromagnetic material with a relatively small magnetic field (Spaldin 2003).

The origin of magnetism in rare earth materials is in the 4f shell, which is shielded by the 5d and 4s shells when forming bonds, so the inter-orbital distance is too great for direct exchange. The RKKY interaction (named after Ruderman, Kittel, Kasuya and Yoshida) has a much longer range because it originates from the conduction electrons. A magnetic ion induces a spin polarization in the conduction electrons, which in turn is felt by magnetic ions over a certain distance and couples them either parallel or antiparallel. The distance over which it can affect the spins of other magnetic ions is the exchange length, which is material dependent (Spaldin 2003).

1.3.3 Ferromagnetic Resonance

A ferromagnetic material consists of magnetic domains, which is a collection of atoms whose individual magnetic moments are aligned with one another, resulting in a uniform magnetization. The aligned spins of the electrons of the atoms results in a magnetization in the material. The frequency at which this resonance occurs under an applied, parallel magnetic field is given by the Kittel equation:

$$f = \frac{\gamma}{2\pi} \sqrt{\mathbf{B}(\mathbf{B} + \mu_0 \mathbf{M})} \quad (1.11)$$

The gyromagnetic ratio (γ) is the ratio of a material's magnetic dipole moment to its angular momentum and is defined for any charged particle by the following equation, where q is the charge of the particles, and m is its mass.

$$\gamma = \frac{q}{2m} \quad (1.12)$$

Precessional motion of magnetic moments is controlled by an external magnetic field. The aligned spins in the magnetic domain precess at a frequency specific to domain size and material, known as the Larmor frequency, as seen in Figure 1-7. The individual spin of the electron is coupled to the orbital angular momentum in this manner.

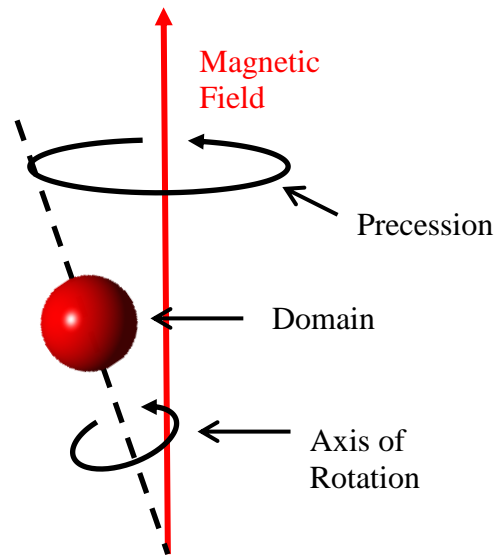


Figure 1-7. Diagram of the magnetic precession of a single domain around the axis of an applied magnetic field (O'Handley 2000).

As the applied field increases, the torque on the magnetic moment increases, causing the precessional frequency to increase as shown by the following equation, where Γ is the torque on the magnetic moment and J is the angular momentum vector:

$$\Gamma = \gamma J \times B \quad (1.13)$$

Because of the frequency-dependence of magnetization, a time dependent approach was developed to more accurately model such systems. The Landau-Lifschnitz-Gilbert (LLG) equation describes the precession of magnetic moments in a solid, and is given by the following equation.

$$\frac{d\mathbf{M}}{dt} = -\gamma \left(\mathbf{M} \times \mathbf{H}_{\text{eff}} - \eta \mathbf{M} \times \frac{d\mathbf{M}}{dt} \right) \quad (1.14)$$

The dynamic magnetization (\mathbf{M}) is dependent on the effective magnetic field (\mathbf{H}_{eff}) the gyromagnetic ratio and the damping parameter, η . This damping parameter, known as the Gilbert damping, is a material specific property, usually experimentally determined. The development of the LLG relation shows that there is a time-dependence of the magnetization of the material on the applied field, and so it has influenced the modeling work in the field of dynamic magnetics greatly (Kittel 2004).

The ferromagnetic resonance (FMR) linewidth of a material indicates the magnetic fields or frequencies at which the material absorbs energy. It is quantified by measuring the energy of a microwave signal orthogonal to the applied magnetic field that is absorbed by the material. Physically, it represents the frequency distribution of the magnetic domains in the material, and so a narrow range, or linewidth, is desirable. Traditionally, magnetic oxides were favored for high frequency applications because their high resistivity mitigates the dissipation of the magnetization in the material in the form of eddy currents. However, functional oxides can be more difficult to grow and their properties depend on the induced crystal structure.

1.3.4 Magnetic Anisotropy

Within a magnetic material, there are interactions between the electron spin, orbitals as well as the crystal lattice. A crystal lattice is composed of bonds, which are formed by orbital overlap, and the lattice-orbital interactions are very strong. The spins of the electron are not influenced very strongly by the lattice of the materials, however, both spin-spin and spin-orbit interactions can be influenced by a magnetic field (O'Handley 2000).

Spin-spin interactions occur when the spin of one electron influences the spin of another, to be either parallel or anti-parallel and are referred to as exchange interactions. Similarly, spin-orbit interactions, commonly referred to as spin-orbit coupling, describe the interactions between the spin and the magnetic field generated by the motion of the orbital around the nucleus. These interactions have a strong influence on the magnetic anisotropy in the material.

A piece of iron, while ferromagnetic, does not necessarily have a net magnetization. This is due to the material being isotropic, meaning that the material contains ferromagnetic domains, but the net magnetization is zero because they negate each other. Magnetic anisotropy is the directional dependence of a material's magnetic properties, such as in a U-shaped magnet. The magnet flux is directed from one pole to another (one end of the U to the other) by an anisotropy induced in the magnet via various processing techniques, such as heat treatments in the presence of a strong magnetic field. Without any type of heat treatment, crystalline magnetic materials tend to have an anisotropy based on the position of the atoms in the lattice, known as magnetocrystalline anisotropy. This directional dependence of the easy axes of magnetization is due largely to the spin-orbit coupling in the material (Spaldin 2003).

For thin films of magnetic materials where the surface area to volume ratio is several order of magnitudes larger than that in a bulk material, a different type of anisotropy occurs, known as shape anisotropy. Shape anisotropy describes the formation of magnetic domains whose dimensions are affected by the thickness and geometry of the film. The origin of this phenomena lies in the demagnetization field, which is generated from the stray fields that form when a material is magnetized. The direction with the lowest demagnetization field indicates the easy axis of the material. As the film thickness is decreased, magnetic domains are more likely to lie in-plane. This leads to magnetic domains that are ellipsoidal rather than spherical. The long

axis of the ellipsoidal domain has a lower demagnetization energy compared to the short axis (Cullity 2009). A study of this effect was assessed for epitaxial Fe (001) with various thicknesses and geometries (Hanson 2002). It was found that for thin films below 10 nm, the magnetic domains formed exclusively in plane. Above 50 nm, the films formed several domains to minimize the demagnetization field.

1.3.5 Magnetoelastic Behavior

A property of all ferromagnetic materials, the direct magnetostrictive effect, describes the change in shape/dimension during magnetization. A common example of the magnetostrictive effect is seen in current transformers, which use a generated magnetic field to step down the current in a power line. The buzzing sound a transformer makes is a result of the magnetostrictive effect, which is traditionally thought of as a loss mechanism in a ferromagnetic material. This change is due to the reorientation of magnetic domains in the material to align with the field, as shown in Figure 1-8. As a magnetic field is applied, the magnetic domains in the film reorient themselves. This reorientation impacts the structure of the film in some magnetic materials and result in an expansion along the applied field for positive magnetostrictive materials and a contraction for negative magnetostrictive materials. The saturation magnetostriction value, λ_s , is the amount of strain in a material from a saturating magnetic field. This value is known for many magnetic materials due to the relative ease of the measurement for bulk samples. The piezomagnetic coefficient is a field-dependent value for strain, which is useful for dynamic applications, but is much more difficult to measure.

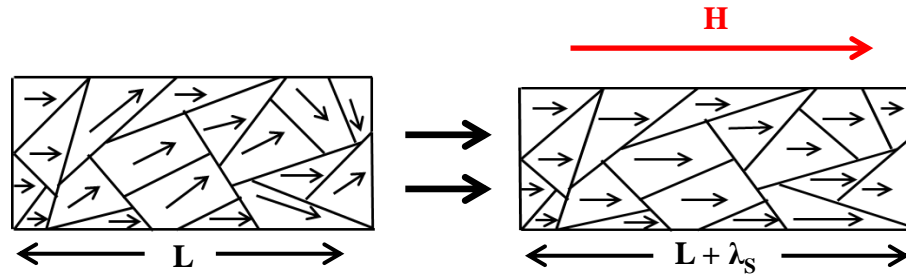


Figure 1-8. Shape change of a ferromagnetic material having positive magnetostriction with applied field, H .

The origin of magnetostriction results from the size of the domains in a magnetic material, as well as its crystal structure. Terbium-iron has the largest magnetostriction of any material; however, its large saturation field (~ 5 Tesla) limits its applications in multiferroic composites. The addition of dysprosium, which has magnetocrystalline anisotropy opposite to that of terbium, was found to reduce the hardness of the material at specific compositions, specifically those which lie on the morphotropic phase boundary, between the tetragonal and cubic phases (Engdahl 2000).

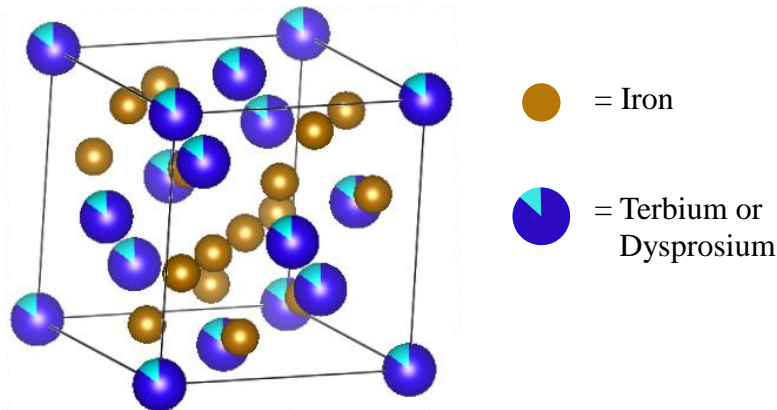


Figure 1-9. Crystal structure for Terfenol-D ($Tb_{0.3}Dy_{0.7}Fe_{1.92}$), where the Tb and Dy atoms can occupy the same lattice position.

In iron-gallium, a rare-earth-free magnetostrictive material, the origin of this effect is less obvious, due to the gallium being diamagnetic. Neutron scattering experiments on $Fe_{1-x}Ga_x$ ($0.14 < x < 0.20$) showed that the addition of Ga caused some of the cubic cells to become

slightly rectangular and therefore, strained. These rectangular domains readily align with an applied magnetic field (Cao 2009). The coexistence of cubic and slightly tetragonal cells result in a saturation magnetostriction an order of magnitude higher than that of iron.

A metric for assessing the magnetoelastic behavior is the magnetomechanical coupling. This parameter, k^2 , has a value between 0 and unity and represents the amount of magnetic energy a material can convert to mechanical energy. It is a function of the dynamic strain coupling, d_{33} , the relative permeability, μ_r , and the mechanical modulus of the material, E (Hudson 1998).

$$k^2 = \frac{d_{33}^2 E}{\mu_r} \quad (1.15)$$

Magnetostriction in amorphous materials is a more complex phenomenon because the effect magnetocrystalline anisotropy is weaker. Amorphous ferromagnetic metals are most commonly doped with a metalloid, such as carbon or boron, to disrupt the crystal structure that contributes to magnetic hardness. Depending on the level of doping, the material can either be a spin glass (doping > 20%) or an amorphous ferromagnet (doping < 20%). A spin glass is a magnetic material with a geometrically frustrated structure, meaning that spins of the atoms do not align in a regular pattern (Engdahl 2000). Because of the frustrated structure, these materials tend to have zero magnetostriction, thus are not useful for strain-coupled composite multiferroics.

Amorphous ferromagnets are a specific type of soft magnetic material, where the domain size is on the order of nanometers. Because of this, one would expect a diminished magnetostriction for the materials, but for many materials, such as FeGaB or CoFeB, this is not the case. The reason is that the materials maintain an orientational order without a regular crystal

structure. One of the most common ways of tuning the anisotropy of an amorphous ferromagnet is via heat treatment. For example, Metglas ($\text{Fe}_{0.45}\text{Ni}_{0.45}\text{Mo}_{0.07}\text{B}_{0.03}$) is an amorphous ferromagnet used for transformer cores. In order to maintain a very fine grain structure, the material is rapidly quenched on the order of 10,000 K/min. The ability to tune the anisotropy of magnetic materials allows for optimization of the loss as well as the magnetoelastic behavior.

1.3.6 Spring Exchange Magnetism

Spring exchange magnetism occurs where a hard and soft ferromagnet are interfaced with one another over very small distances on the order of the exchange length of the material. The soft ferromagnet, usually a transition metal with high saturation magnetization, is interfaced with a hard ferromagnetic material, generally a rare earth-based ferrimagnet with a high coercivity. The resulting material maintains a high magnetization and high coercivity because the rare-earth material helps the softer material maintain its anisotropy, increasing the overall coercivity. A SmCo/Fe thin film demonstrated a broader coercivity and higher magnetization that diminished as the Fe-interlayer thickness increased (Liu 2008). One of the main advantages of these composites is that they require significantly less of the rare-earth magnetic material, increasing the stability of the device and reducing the cost.

The study of magnetic heterostructures is not limited to rare-earth materials. The coupling between the hard ferromagnetic (FM) layer and the soft FM layer reduces the energy required to flip the magnetization of the composite. One study has shown that interfacing FeGa and NiFe in nanowire form can affect the static magnetic properties, specifically the coercivity and anisotropy field (Lupu 2008). In this study, layer thickness was fixed at 20 nm for the NiFe and 60 nm for the FeGa, both far larger than the exchange length of either material. Both the

number and thickness of the individual layers was found to affect the coercivity and anisotropy of wires, which is attributable to a change in shape anisotropy. The coercivity of the heterostructures was found to be similar to that for pure FeGa nanowires, however, the magnetoelastic behavior was not reported for this system.

Another study examined the impact of the number of layers and their thickness on the magnetic properties of $(\text{TbFe}_2/\text{Fe}_3\text{Ga})_n$ system grown via DC magnetron sputtering. It was found that the magnetic properties of the Tb-Fe phase is highly dependent on thickness as well as annealing temperature, though diffraction studies showed that the FeGa formed a bcc crystal structure as deposited (Ranchal 2011). After crystallization and layer optimization, a magnetostriction value of $550 \mu\epsilon$ and a coercivity of 400 Oe was achieved (Ranchal 2012). The hybrid material exhibited the complementary properties of the phases: high saturation magnetostriction of TbFe_2 and the low coercivity and high magnetization of FeGa.

NiFe has been used in combination with other magnetically hard materials as an attempt to reduce the energy required to flip the magnetization. The dynamic magnetic properties of a hard magnetic material, $(\text{Fe}_{70}\text{Co}_{30})_{0.95}\text{N}_{0.05}$, have been shown to be significantly affected by sandwiching it between thin films of NiFe. Specifically, a trilayer NiFe (5 nm)/FeCoN (100 nm)/NiFe (5 nm) structure exhibited a significantly reduced the coercivity from 5 Oe to 0.6 Oe along the hard axis (Wang 2000). Since the NiFe layers were not exchange-coupled to one another because they were separated by 100 nm, they were likely coupled through the magnetostriction of the FeCoN layer. The reduction in coercivity and enhanced permeability was attributed to a change in the magnetic anisotropy dispersion; however, only a single heterostructure was studied. Another study showed that reducing the layer thickness in a Fe/NiFe material system enhanced the magnetic softness of the multilayers (Nakatani 1988). Holding the

total thickness constant, the structure was sub-divided into more layers and this was shown to result in a reduction in the magnetic anisotropy dispersion, by limiting the possible orientations of an easy axis in the plane of the film. From these works, it is clear that heterostructures provide a means of tuning magnetic properties, and that their properties are dependent on the thickness and number of layers.

Exchange-coupled magnetic heterostructures offer tunable properties that are a function of both the constituent phases as well as the geometry of the structures. Developing magnetic materials for high-frequency, strain-coupled applications requires a compromise between magnetic softness and magnetoelastic coupling. Heterostructures provide one avenue of developing the optimal material.

1.4 Multiferroic Composites

The coupling between electricity and magnetism was first proposed by Pierre Curie in 1894, but it was not until the work of Landau and Lifschitz in 1960 that a model for the linear coupling between the two phenomena was developed, shown in the following equations:

$$P_i = \sum \alpha_{ij} H_j + \sum \beta_{ijk} H_j H_k + \dots \quad (1.16)$$

$$M_i = \sum \alpha_{ij} E_j + \sum \beta_{ijk} E_j E_k + \dots \quad (1.17)$$

P and M are the electric and magnetic polarizations; H and E are the applied magnetic and electric fields, respectively. The linear and nonlinear magnetoelectric (ME) susceptibilities are represented by α and β , respectively. In 1960 Astrov discovered the first single phase magnetoelectric material, Cr_2O_3 , and showed that an applied electric field caused the material to exhibit a magnetic moment proportional to that field (Astrov 1961).

Magnetoelectric materials are a broad category of materials, of which multiferroic materials are one type. Multiferroic materials contain at least two primary ferroic orderings. There are four primary ferroic orderings: ferromagnetism, ferroelectricity, ferroelasticity and ferrotoroidicity. As mentioned previously, ferromagnetism is property of a material that may undergo spontaneous magnetization. Ferroelectricity describes a material that may undergo a spontaneous polarization, which can be reversed by a negative electric field. A ferroelastic material may undergo a spontaneous strain, which is reversible with an applied stress. Ferrotoroidicity is the phenomena where a material can undergo a spontaneous phase transition to a long-range order of microscopic magnetic toroidal moments. The interactions between these ferroic orderings can be seen in Figure 1-10. The promise of multiferroic material systems is that they could potentially allow for electric field control of magnetism, instead of current control, and as such, there is a growing interest in the field.

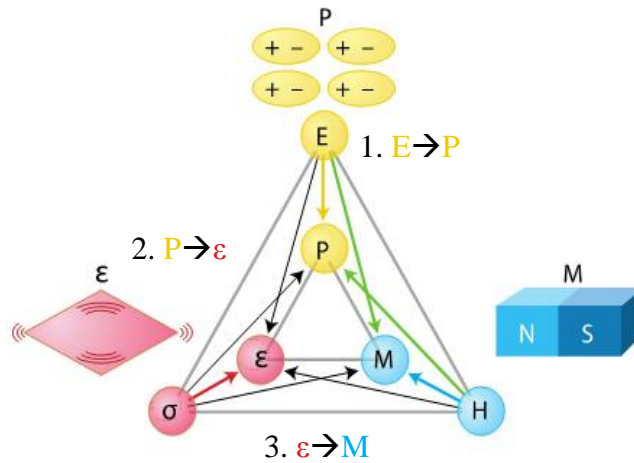


Figure 1-10. Interactions between ferroelectricity, ferromagnetism and ferroelasticity, and the route to control of magnetization through strain polarization. Electric field polarizes a ferroelectric phase (1), which generates a strain in the ferroelectric via the piezoelectric effect (2), which then strains a ferromagnetic phase (3), resulting in a net magnetization (Spaldin 2005).

Multiferroic systems are largely divided into two categories, intrinsic and composite. Intrinsic multiferroics are those which naturally contain the two ferroic orderings in a single phase. The most widely studied intrinsic multiferroic is BiFeO_3 (BFO) because it is a multiferroic at room temperature. However, it is not a true multiferroic because it is a ferroelectric and antiferromagnetic, meaning that an applied field does not induce a net magnetization in the material. There are other intrinsic multiferroic materials, but for most, their Curie temperature lies far below room temperature.

Composite multiferroic systems are an engineered approach to couple electricity and magnetism at the nanoscale via interfacing different ferroic materials, particularly those that are ferroelectric and ferromagnetic. There are several different ways in which these materials can couple, but this discussion shall be limited to the two most common: charge-mediated coupling and strain-mediated coupling.

Charge-mediated coupling in multiferroic systems originates from the influence of interfacial effects on a ferromagnetic film; specifically they are sensitive to electric fields, making them magnetoelectric. One of the most common examples of this coupling is in the CoFeB/MgO system, where the MgO acts as a spin-dependent charge filter (Amiri 2012). This can have an effect on the occupancy of d orbitals at the interface of the ferromagnetic layer. This phenomenon can be tailored for their incorporation into memory devices based on a voltage-controlled magnetic anisotropy effect, which describes the effect of electric field on the magnetic precession in a ferromagnetic film, as shown in Figure 1-11.

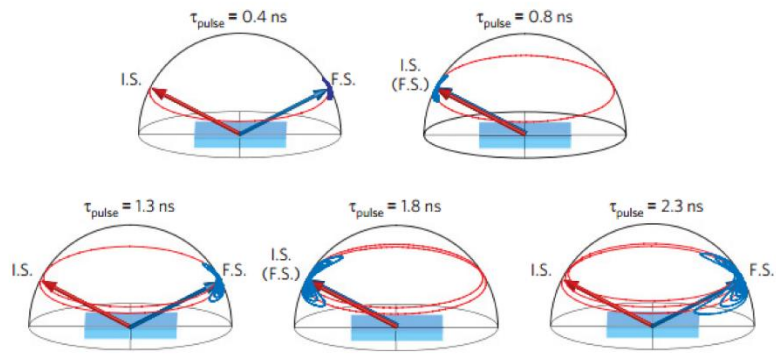


Figure 1-11. Electric-field-induced precessional switching of magnetization in a magnetic tunnel junction (MTJ) (Amiri 2012).

The magnetic spins, which are precessing in the ferromagnetic layer, are forced to flip by the applied voltage, and the probability of flipping is dictated by the length and timing of the voltage pulse. The spin-flipping affects the tunneling magnetoresistivity of the film.

Strain-coupled multiferroic systems are another type of composite multiferroic, where the ferromagnetic and ferroelectric ordering parameters are controlled by magnetostriction and piezoelectricity (Wang 2010). An applied magnetic field, H , induces a strain in a ferromagnetic material. The strain is then transferred to a piezoelectric phase, induce a polarization. This is called the direct magnetoelectric effect, and it can be seen in the upper diagram in Figure 1-12. The converse ME effect is the opposite: strain from the electric polarization causes magnetic domain realignment, resulting in a net magnetization, as shown in the lower diagram in Figure 1-12. Multiferroic composites are of great interest because they allow for the energy efficient control of magnetism at the nanoscale, due to the use of electric field instead of current.

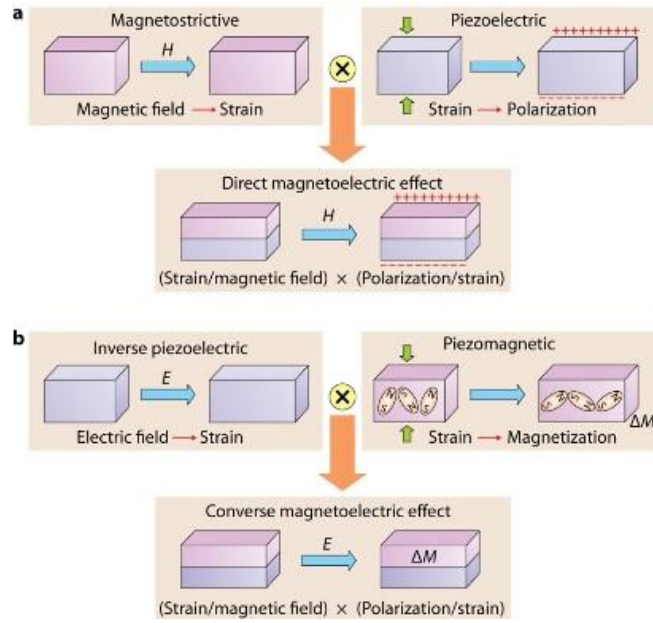


Figure 1-12. Structure of strain-mediated coupled in composite multiferroic systems (Wang 2010)

The converse magnetoelectric effect has a variety of potential applications including non-volatile computer memory as well as microelectromechanical systems (MEMS). The direct effect can be utilized to make magnetometers as well as antennas, but these systems are more complicated because of the effect of varying frequency.

1.5 RF multiferroic systems

Arguably the first example of a strain-based generation of an electromagnetic wave was proposed in 1957 with the magnetic material YIG (Geller 1957). The material's magnetic anisotropy was shown to be dependent on the strain, and so it was suggested that a material with a low FMR linewidth could be mechanically strained at a certain frequency and an electromagnetic wave could be generated.

Early RF multiferroic composites were fabricated using a ferrite (an insulating ferrimagnet) so that the energy from the EM wave would not contribute to the formation of eddy

current losses in the thin films. YIG was the material of choice for this early work, and thick films (1-110 μm) were epitaxially grown on gadolinium-gallium-garnet (GGG), which has excellent lattice matching with YIG. These films were then bonded to single crystal PMN-PT (piezoelectric material) via epoxy, and voltages were applied to the PMN-PT to induce a strain (Shastry 2004). From this work, two critical conclusions were made. First, it showed that strain-coupling these materials at microwave frequencies was possible, even though YIG has a low magnetostriction value and the two materials were bonded via epoxy. Second, it showed that there is a strong dependence of the magnetoelectric coupling on the thickness of the ferromagnetic layer. There is a trade-off, however, as for YIG films, the quality of the films as well as the magnetostriction values tend to increase with increasing film thickness.

Composite multiferroics continued to be an area of rapid development, but in order to enhance the coupling, thinner films of materials that have a higher magnetostriction value were needed. However, these materials tend to be conductive (metals), and so the losses are high due to the formation of eddy currents. Additionally, the materials tend to be magnetically hard.

Doping of ferromagnetic materials has been shown to greatly affect the physical and magnetic properties. For instance, cobalt-iron films doped with around 20% boron have been demonstrated to allow for the flipping of magnetization from out-of-plane to in-plane via electric field control, when the film is thin enough (1.1 nm) to demonstrate perpendicular magnetic anisotropy (Amiri 2012). Metalloid dopants, such as boron or carbon, have been shown to decrease the crystallinity of certain ferromagnetic metals, which reduces the magnetocrystalline anisotropy of the film. In turn, this allows the magnetic domains to rotate more easily, as they are smaller when doped, leading to an enhanced magnetic softness. An excellent example of this effect is in the iron-gallium-boron (FeGaB) material system.

Iron-gallium is a ferromagnetic material that is of great interest for industrial applications because it has the highest magnetostriction value of any intermetallic that does not contain a rare-earth element, around 400 $\mu\epsilon$ for single crystal bulk, and 275 $\mu\epsilon$ for single crystal thin film, however, its broad FMR linewidth and large coercivity limited its use in RF applications. It was discovered that the addition of boron, up to 18 at. %, narrowed the coercivity, reduced the FMR linewidth while maintaining a relatively high saturation magnetostriction, but more importantly, a high piezomagnetic coefficient, around 7 $\mu\epsilon/\text{Oe}$, due to the low saturation field (Lou 2007).

FeGaB has been incorporated into a variety of multiferroic heterostructures, including ferroelectric materials such as PZN-PT and PMN-PT (Lou 2008, Lou 2009). This work demonstrated a very large ME coupling coefficient of 2365 Oe-cm/kV and a tunable FMR frequency range of up to 5.82 GHz. One of the most promising applications is the integration into room temperature magnetometers, with sensitivity down to picotesla, achieved with a FeGaB/ Al_2O_3 heterostructure to reduce eddy current losses, and aluminum nitride as the piezoelectric material (Nan 2013).

Another avenue for achieving a low loss magnetostrictive material is through the use of exchange-coupled magnetic heterostructures. Multilayers have a few distinct advantages compared to doped systems. First, doped systems have an upper limit for the doping concentration, where the material may transition to a glass-like structure, which has little to no magnetostriction. Additionally, ensuring uniform distribution of the dopant can be difficult depending on the synthesis method used. The properties of magnetic multilayers are tunable via layer thickness, an easily controllable parameter in most semiconductor deposition processes. Table 1-1 lists several materials and their properties discussed previously that need to be optimized for this application.

Table 1-1. Pertinent functional properties of various ferromagnetic material candidates are summarized for comparison and material selection for integration into a multiferroic antenna.

Material	FMR LW (Oe)	Hc (Oe)	μ	$d\lambda/dH$ (Oe ⁻¹)	E (GPa)	k^2	Tc (°C)
Nickel	250	35	1000	0.17	200	0.1	360
Terfenol-D	1000	1500	40	2.8	40	0.8	380
FeGaB	20	1	500	7.0	65	0.4	400
Y ₃ FeO ₁₂	1	1	30	0.05	170	0.01	290
FeGa	450	80	100	2.0	75	0.6	700
NiFe	20	1	30	0.01	110	0.01	280

FMR LW = Ferromagnetic Resonance Linewidth; Unit: Oe
Hc =Coercivity; Unit: Oe
 μ =Relative Permeability; Unitless
 $d\lambda/dH$ =Piezomagnetic Coefficient; Unit: Oe⁻¹
E =Young's Modulus; Unit: GPa
 k^2 =Magnetomechanical Coupling Coefficient; Unitless
Tc =Curie Temperature; Unit: °C

These properties can be separated into two categories: magnetic loss/softness and the magnetomechanical coupling. Magnetic loss is measured by the FMR linewidth, a measure of the range of magnetic fields or frequencies in which the material absorbs the energy. For this application, a linewidth below 40 Oe desired. The metric for magnetic softness is the coercivity, which indicates the amount of energy needed to flip the magnetization of the material. For a receiving antenna, the energy of the incident signal would be very low, and so a coercivity below 10 Oe is desired. Magnetomechanical coupling, k^2 , describes the ability of a ferromagnetic to convert strain to magnetization or vice-versa. It is a function of the permeability, piezomagnetic coefficient, $d\lambda/dH$, and the modulus of the material, E.

$$k^2 = \frac{d_{33}^2 E}{\mu_r} \quad (1.18)$$

If a material candidate was selected on the softness/loss properties alone, Y₂Fe₅O₁₂ (YIG) is the obvious choice, with FMR linewidth and coercivity of 1 Oe. YIG is also an insulator,

which would reduce the eddy current loss. However, this material has poor magnetoelastic coupling, indicating by the low piezomagnetic coefficient. Additionally, its properties are structure dependent, requiring the use of specialized substrates to attain the optimal crystallographic orientation. Another material with low loss and sufficient softness is NiFe, and fabrication in thin film form on a variety of substrates has been demonstrated (Kay 1964, Ueno 1995, Xu 2015). NiFe has poor magnetoelastic behavior as well, and so by itself not a candidate for a strain-coupled multiferroic antenna.

If a material candidate was selected based on magnetomechanical coupling alone, Terfenol-D ($\text{Tb}_{0.3}\text{Dy}_{0.7}\text{Fe}_2$) is the obvious choice, with the highest k^2 of any magnetic material at room temperature. However, it has a broad FMR linewidth and is magnetically hard. Similar to YIG, the growth of thin films is difficult, as the properties are highly dependent on the ratio of Tb/Fe as well as orientation of the film. Another material with large k^2 is FeGa, which has the highest room temperature coupling of any material not containing a rare earth element and can be grown in thin film form (Battogtokh 2009, Zhang 2013, Zhang 2015). Its loss and softness properties are better than Terfenol-D, but still above the targeted values, so by itself it is not a candidate for this application.

Iron-gallium-boron (FeGaB) is a relatively new magnetostrictive material that has magnetic properties that are tunable via composition as well as functionality in multiferroic composites (Lou 2007, Lou 2009, Nan 2013). Doping with 12% boron results in a material with almost no coercivity, a high degree of magnetization as well as a large piezomagnetic coefficient, and so this material system was explored initially for integration into a multiferroic antenna.

Though FeGaB is a promising candidate for this application, FeGa/NiFe multilayers were pursued as an alternative and potentially better material because of the tunability that multilayers

offer compared to doped magnetic systems, where too large of a doping concentration results in little to no magnetostriction. Studies of FeGaB thin films showed that the magnetic softness and loss were higher than reported literature values. FeGa/NiFe multilayers demonstrated favorable loss and softness while maintaining a large magnetostriction, and so these were integrated into antenna devices.

1.6 Scope and Organization

Finding the optimal magnetic material for this application requires balancing the magnetic loss and softness of the material and the magnetomechanical coupling. This work was divided into the development of two material systems: iron-gallium-boron (FeGaB) as a single-phase RF magnetic material and iron-gallium/nickel-iron (FeGa/NiFe) heterostructures. FeGaB thin films were grown via sputter deposition and a thickness dependence of the coercivity and FMR linewidth was observed. FeGa/NiFe heterostructures were synthesized to take advantage of their complementary magnetic properties. The rotation of the magnetization with applied electric and magnetic fields in the individual layers was studied via polarized neutron reflectometry. Finally, the heterostructures were incorporated into a surface acoustic wave (SAW) and a bulk acoustic wave (BAW) antenna device to characterize the multiferroic coupling in the GHz regime.

Chapter 2 : Experimental Setup

Several material systems were synthesized via sputter deposition in this work: iron-gallium, iron-gallium-boron, and nickel-iron. Composition of the thin films was confirmed via x-ray photoelectron spectroscopy (XPS) and their crystal structures were analyzed via x-ray diffraction. Surface morphology was characterized by atomic force microscopy (AFM). Magnetic hysteresis measurements were performed via superconducting quantum interference device (SQUID) magnetometry, magneto-optic Kerr effect (MOKE) spectroscopy, and vibrating sample magnetometry (VSM). Magnetic domain formation and propagation was observed with magneto-optic imaging film. Electron spin resonance (ESR) spectroscopy was used to analyze the FMR linewidth at X band (9.7 GHz), and a stripline measurement was used for broadband FMR measurements, from which the real and imaginary components of permeability were extracted. The magnetostriction of the materials was measured via SQUID magnetometry with *in situ* electrical poling. Coupling between the layers and rotation of the magnetization with applied electric field was observed via polarized neutron reflectometry (PNR) studies.

2.1 Synthesis

2.1.1 Sputter Deposition

Sputtering is a specific type of physical vapor deposition (PVD) where atoms are ejected from a source, or target, by means of bombardment with high energy particles, which can be supplied by plasma, an ion source, or an accelerator. In the case of plasma sputtering, the plasma is generated by ionizing a gas in a low pressure environment. A negative bias is applied to the source, so that ions accelerate toward the target, and in turn they bombard the surface with high

energy, ejecting particles from source. The ejected particles are directed at a substrate by the incident angle of the high energy particles and form a thin film. A schematic of this process can be seen in Figure 2-1.

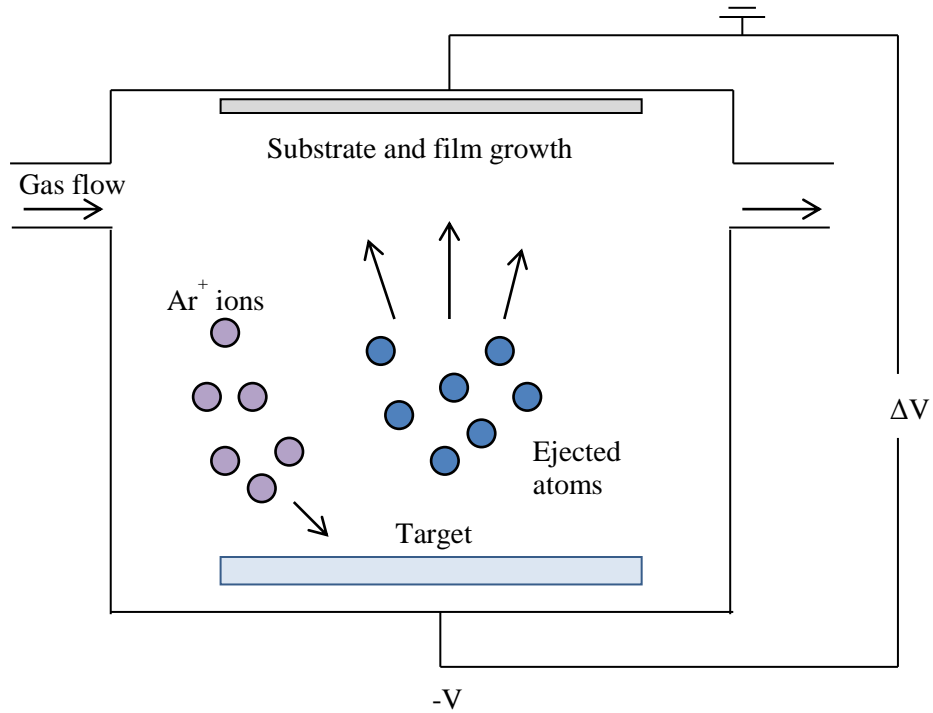


Figure 2-1. Schematic of the sputtering phenomena where the bias between the substrate and the target combined results in the ionization of argon atoms.

The target has a high purity ($> 99.9\%$) and can be made from a variety of materials, such as metals, oxides or nitrides. Argon, nitrogen and oxygen are common choices for generating the plasma. The target is held in a cathode, made of a material with very low resistance that attract the positively charged argon ions once biased. Oxygen or nitrogen is used more frequently in reactive sputtering, where the atoms ejected from the target react with the plasma to form a thin film. For instance, thin films of aluminum nitride are often grown via reactive sputtering, where a pure Al target is sputtered with a mixture of Ar and N_2 plasma. Argon is used for sputtering

metals, as well as single targets of oxides or nitrides. Co-sputtering of different materials is a method for tuning the film composition, and therefore, the properties.

Depending on the properties of the material, either a direct current (DC) or radio frequency (RF) bias is needed. A DC bias is sufficient for sputtering conductive materials, or materials where there is no charge build up. The sputtering power is the number of incident argon ions (a flow of electrons, or a current) multiplied by the bias applied to the cathode. An RF bias is used in materials, such as oxides or nitrides, where charge build-up would cause the positively charged sputtering ions to be repelled from the target. RF sputtering requires an impedance-matching network (Hayakawa 1992).

The main parameters, aside from the purity/composition of the target, that are controlled during sputtering are as follows: sputtering power, gas flow rate, and operating pressure of the system. In both RF and DC systems, an increase of sputtering power results in a higher sputtering yield, and therefore a higher growth rate. Gas flow rate and sputtering pressure are inherently linked by the pumping capabilities of the system, but does not have a direct effect on the quality of the film produced. The sputtering pressure controls the amount of argon in the chamber, and thereby controls the amount of argon that can be ionized and bombard the target. There is an optimal sputtering pressure to achieve a maximum growth rate: if the pressure is too high, the argon ions are scattered by the unionized argon. High sputtering pressure can also decrease the quality of films grown, as the measured pressure includes the sputtering gas as well as any gaseous impurities (Thornton 1977).

Low pressure sputtering is desirable for producing high quality films with little contamination, but it is difficult to maintain plasma at such pressures. Magnetron sputtering is used to increase the ionization of argon by trapping electrons near the surface of the target,

usually accomplished with a permanent magnet placed behind the cathode. The electrons draw in the positive argon ions, and allow for a higher sputtering rate. This technique can be applied for RF or DC sputtering systems.

For this work, two sputtering chambers were used. A Denton™ Discovery sputtering system was used for the growth of FeGaB. It is cryo-pumped and has a base pressure of $< 10^{-7}$ torr. The system has four 3" cathodes and two power supplies, 1 RF and 1 RF/DC. It utilizes confocal sputtering as well as substrate rotation to achieve conformal planar coatings. This tool does not have a load-lock, and so the targets were exposed to air after each deposition, leading to the need for extended burn-in times. Pressure control is achieved via a VAT™ system, comprised of a butterfly gate valve before the cryo-pump, which can be adjusted to maintain a specified pressure. The dimensions and purity specifications for the FeGa and boron targets used in this system can be found in Table 2-1.

The second sputtering tool used, an Ulvac™ JSP-8000 tool, has four 4" cathodes, 2 RF and 2 DC with dedicated power supplies, and a base pressure of $\sim 10^{-7}$ torr via turbo pump. The cathodes are arranged horizontally with respect to the substrate holder, reducing the risk of a small flake falling onto the samples. Additionally, the tool has a load-lock, which allows for a reduction in target burn in and pump-down time. Aside from the load-lock, the main difference between the tools is how the pressure is maintained. Pressure is controlled in the second tool by adjusting the argon flow rate. The target specifications for the FeGa and NiFe targets used in this system are listed in Table 2-1.

Iron-gallium-boron (FeGaB) was synthesized via co-sputtering of Fe₈₀Ga₂₀ (at. %, 99.9% purity) and boron (99% purity). FeGa was held at a constant power of 60 W DC and all

depositions took place at room temperature. Boron power was varied from 30-50 W RF to tune the boron content.

Fe₈₅Ga₁₅/Ni₈₁Fe₁₉ multilayers were grown via DC magnetron sputtering with pressures varying for 0.3 – 3.0 mTorr and powers ranging from 100 – 300 W to minimize the residual stresses in the films. All samples had a base layer of Fe₈₅Ga₁₅ with Fe₈₅Ga₁₅/Ni₈₁Fe₁₉ bilayers grown subsequently.

Table 2-1. Relevant technical specifications of sputter targets used in this work

Target	Purity (%)	Diameter (in.)	Thickness (in.)	Power (W)
FeGa (80/20 at. %)	99.95	3.00	0.08	60 (DC)
Boron	99.9	3.00	0.125	30-50 (RF)
FeGa (85/15 at. %)	99.95	4.00	0.1	100-250 (DC)
NiFe (81/19 wt. %)	99.9	4.00	0.25	100-250 (DC)

Purity = Purity of the target; Unit: %
Diameter = Diameter of the cylindrical target; Unit: in.
Thickness = Thickness of the cylindrical target; Unit: in.
Power = Power range used for a specific target; Unit: W

Thickness and composition control via sputtering time was confirmed via profilometry and scanning electron microscopy (SEM) for thinner samples and is discussed for the specific materials in Chapters 3 and 4.

2.1.2 Residual Stress Mitigation in Sputtering

There are a variety of deposition conditions that impact the residual stresses in a sputtered film. Tensile stresses tend to form when deposition conditions favor low adatom mobility (Thornton 1977). These stresses can be induced in several ways, including low substrate temperature, low energy particle bombardment and the physisorption of gas into the film. The low energy of the particles is most commonly attributed to a higher sputtering pressure, where

the particle experiences many more collisions with other particles before interacting with the target, reducing its energy. The most popular theory for the origin of these stresses describes the competing interatomic forces between individual grains as well as the substrate. Sputter growth initiates with the formation of isolated atomic clusters. As the grains grow larger, their interatomic interactions cause an elastic deformation of the grain walls, which are fixed due to the much stronger forces bonding the substrate to the grain.

The formation of compressive stresses is attributed to two mechanisms: incorporated impurities and atomic peening, or roughening, of the film via high energy particles. For the scope of this work, oxygen and argon incorporation are considered. Oxygen can incorporate into grain boundaries, reducing the grain coalescence, mitigating the tensile forces. It was originally thought that argon entrapment in the film lead to the compressive stresses; however, it was found that the stresses were induced by the surface bombardment with high energy particles, i.e., atomic peening (Windischmann 1992). The energy of the bombarding particles has a significant impact on the residual stress, and it can be tuned via sputtering pressure and power.

The reason for minimizing residual stress is twofold. First, strong compressive forces can have a negative impact on the positive magnetostriction of a magnetic material, such as FeGa. Additionally, these compressive forces can cause issues with fabrication, especially in microelectronmechanical systems (MEMS), which often require free standing structures. Since reducing the stresses to zero can be difficult, especially for a process involving more than one material, slightly tensile residual stresses are acceptable. Stresses were tuned by adjusting the sputtering pressure to find a minimum, then adjusting the power.

2.1.3 Sample Configurations

This dissertation can be discussed in two parts: doped material system, FeGaB, and multilayer material systems, with FeGa/NiFe as the constituent phases. FeGaB was synthesized in single-phase thin film form via co-sputtering. FeGa/NiFe multilayer heterostructures were deposited in a variety of geometries and configurations and so a nomenclature was established for these samples. A 1 Bilayer (1 BL) sample refers to a single FeGa/NiFe bilayer on top of a base FeGa layer. Table 2-2 lists the bilayer samples used to optimized bilayer configurations and explore the origin of the tunability.

Table 2-2. Description of bilayer configurations of the FeGa/NiFe samples characterized to optimize the structures. All samples were grown on Si and PMN-PT.

Sample	Bilayer Structure	FeGa:NiFe (vol. rat.)	Experiments
1 BL	(25 nm FeGa/50 nm NiFe) ₁ /25 nm FeGa	1:1	Optimization, PNR, MOIF
2 BL	(17 nm FeGa/25 nm NiFe) ₂ /17 nm FeGa	1:1	Optimization
3 BL	(13 nm FeGa/17 nm NiFe) ₃ /13 nm FeGa	1:1	Optimization
4 BL	(10 nm FeGa/13 nm NiFe) ₄ /10 nm FeGa	1:1	Optimization
5 BL	(8.5 nm FeGa/10 nm NiFe) ₅ /8.5 nm FeGa	1:1	Optimization, SAW
6 BL	(7.2 nm FeGa/8.5 nm NiFe) ₆ /7.2 nm FeGa	1:1	Optimization
7 BL	(6.3 nm FeGa/7.2 nm NiFe) ₇ /6.3 nm FeGa	1:1	Optimization
8 BL	(5.5 nm FeGa/6.3 nm NiFe) ₈ /5.5 nm FeGa	1:1	Optimization, PNR, MOIF

The first aspect of this work focused on the optimization of the bilayer structures and the explanation for the tunability of the properties with decreasing layer thickness, as shown in Figure 2-2. Tunability was explored for 1 – 7 BL configurations and the in-plane domain size

and coherent rotation of magnetization was determined for 1 BL and 8 BL samples, which correspond to very thick and very thin layers, respectively.

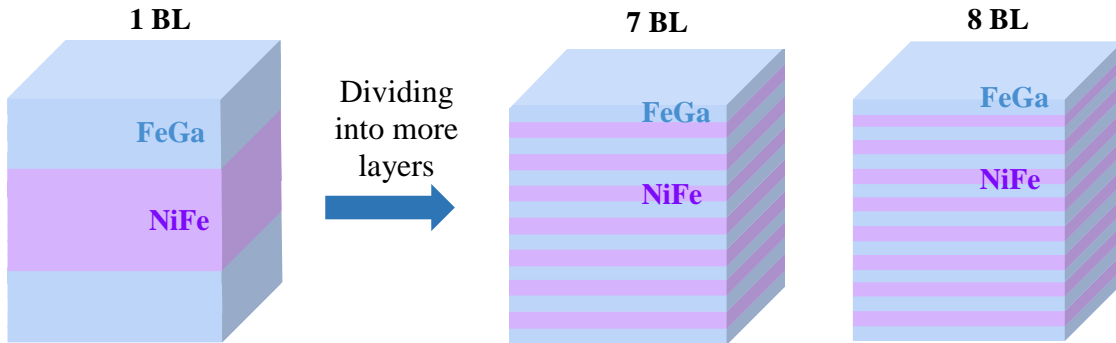


Figure 2-2. Schematics of the bilayer structures used to 1) determine the optimal bilayer structure and 2) determine the origin of the thickness-dependent tunability of these structures.

For a strain-coupled multiferroic system, coherent rotation of magnetization with applied strain is critical for device integration. To this end, single bilayer samples were grown on PMN-PT (011) substrates with a fixed thickness of the magnetostrictive FeGa and a variable thickness of NiFe, which are shown on the left in Figure 2-3 and described in Table 2-3. A superlattice structure, similar to what would be incorporated into an antenna structure, is shown on the right. Polarized neutron reflectometry was used to determine the depth-dependent magnetization of these films with electric field induced strain.

Table 2-3. Description of the bilayer samples measured via PNR with applied strain. All samples were grown on Si/PMN-PT.

Sample	Bilayer Structure	FeGa:NiFe (vol. rat.)	Experiments
1 BL _(3:1PNR)	7 nm NiFe/20 nm FeGa	3:1	PNR w/strain
1 BL _(1:1PNR)	20 nm NiFe/20 nm FeGa	1:1	PNR w/strain
1 BL _(1:2PNR)	40 nm NiFe/20 nm FeGa	1:2	PNR w/strain
3 BL _(PNR)	(20 nm FeGa/7 nm NiFe) ₃ /20 nm FeGa	4:1	PNR w/strain

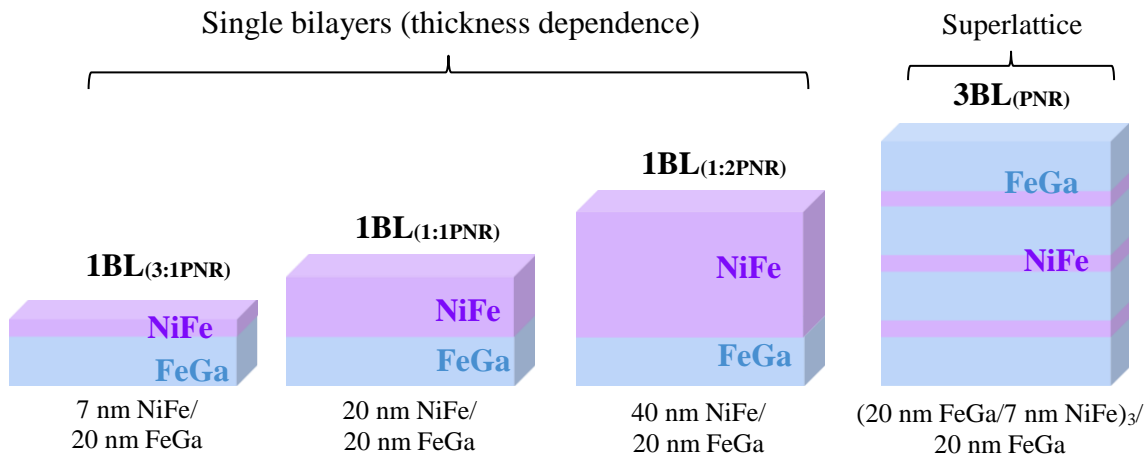


Figure 2-3. Schematics of the four samples grown to study the depth-dependent magnetization rotation with applied strain. The three samples on the left were used to analyze the thickness-dependence of the strain effect and the sample on the right is a super lattice, like what would be incorporated into a device.

Once the layer thickness and configuration were optimized and coherent rotation of all layers was verified, the samples were integrated into two antenna structures: a surface acoustic wave (SAW) and bulk acoustic wave (BAW) structure. The SAW structure was designed to measure the absorption of an acoustic wave traveling through a piezoelectric substrate via the magnetoelastic material. From this, the frequency-dependent magnetoelastic behavior of the film was assessed. The BAW antenna is designed to measure how well the material can convert an

electromagnetic wave into an acoustic wave. The samples grown for this are described in Table 2-4 and shown in Figure 2-4 and the measurement techniques are discussed in Section 2.4.2 and the results are discussed in Chapter 5.

Table 2-4. Description of the bilayer samples integrated into the BAW and SAW antenna structures. Samples were grown on Si/PMN-PT as well as the respective antenna structure.

Sample	Bilayer Structure	FeGa/NiFe (vol. rat.)	Experiments
12 BL _(BAW)	(25 nm FeGa/5 nm NiFe) ₁₂ /25 nm FeGa	5:1	BAW
5 BL _(SAW1)	(4.2 nm FeGa/5 nm NiFe) ₅ /4.2 nm FeGa	1:1	AD-FMR
5 BL _(SAW2)	(8.5 nm FeGa/10 nm NiFe) ₅ /8.5 nm FeGa	1:1	AD-FMR

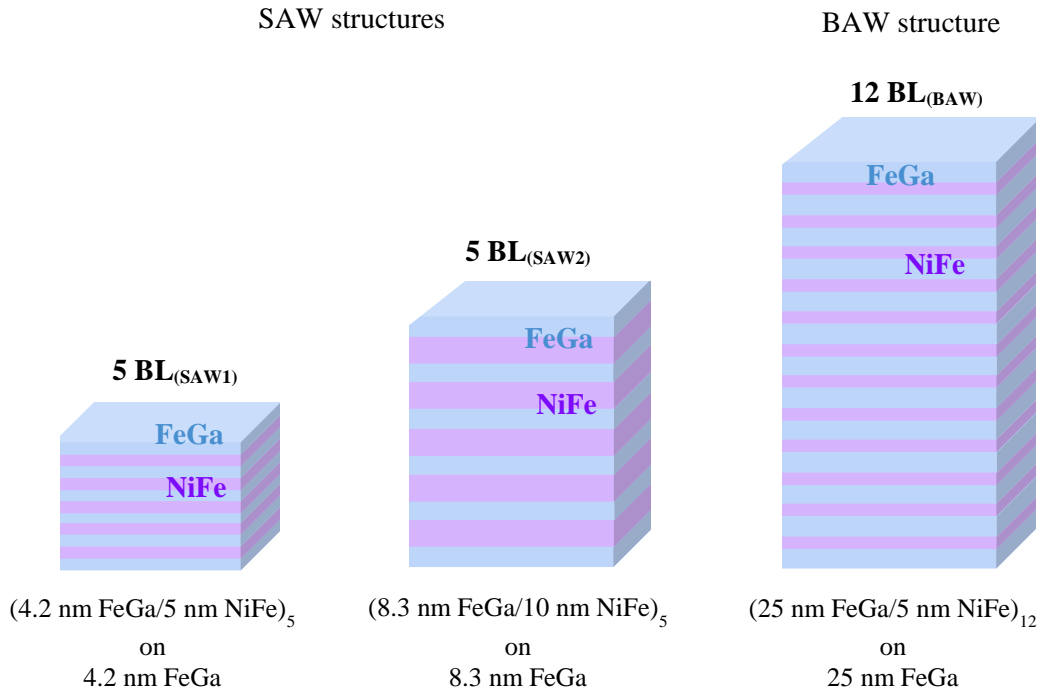


Figure 2-4. Bilayer samples measured in (left) surface acoustic wave (SAW) measurements and (right) bulk acoustic wave (BAW) measurements.

2.2 Material Characterization

2.2.1 X-ray Photoelectron Spectroscopy

X-ray photoelectron spectroscopy (XPS) is a technique used for characterizing the surface composition and chemical bonding states of very thin films. The material is irradiated with tuned x-rays while the number of core photoelectrons emitted from the surface is counted by a spectrometer. A diagram of this can be seen in Figure 2-5. XPS is useful for analyzing the surface of thin films, as electrons that are excited further away from the surface may be subject to scattering.

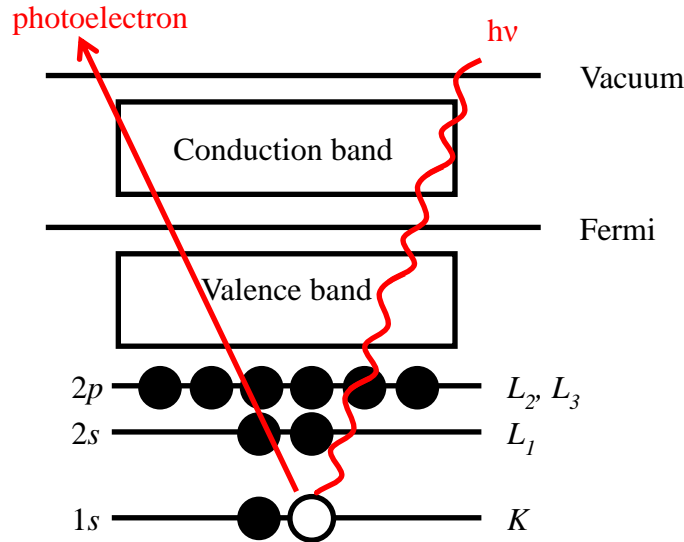


Figure 2-5. A schematic illustration of emission of a photoelectron by the x-ray with an incident kinetic energy of $h\nu$, from the 1s orbital.

This technique can be simply described by an energy balance, where the kinetic energy of the emitted photoelectron is equal to the difference of the energy of the x-rays ($h\nu$), the binding energy ($E_{binding}$) and the work function of the spectrometer (ϕ).

$$KE = h\nu - E_{Binding} - \phi \quad (2.1)$$

The binding energy is different for every core photoelectron and so depending on the resolution of the spectrometer, every element aside from hydrogen and helium can be uniquely identified.

Additionally, because the binding energy is specific to the energy shell, chemical bonding information about the sample can be inferred (Wolstenholme 2003). During a scan, the spectrometer counts the number of photoelectrons emitted when incident x-rays of certain energy strike the sample. The experiment needs to be performed in a high vacuum system so the energy of the emitted photoelectrons is not affected by gas phase collisions. An example of a survey scan of iron-gallium-boron can be seen in Figure 2-6.

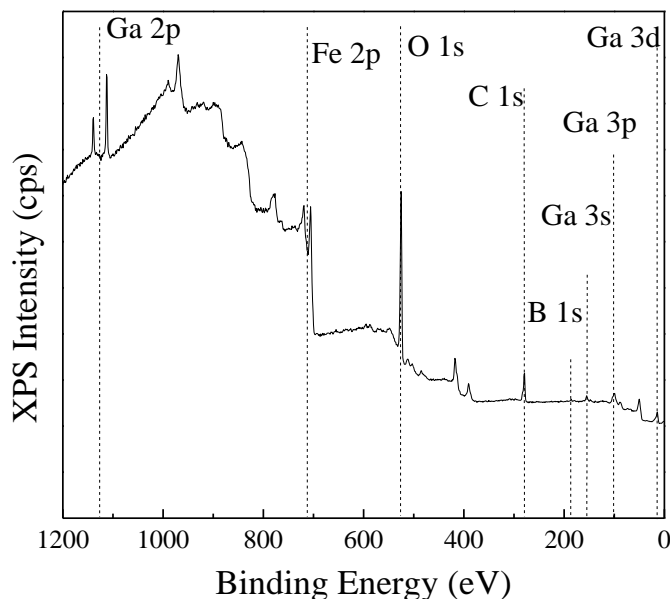


Figure 2-6. XPS survey scan from 1200 – 0 eV of a 100 nm $\text{Fe}_{76}\text{Ga}_{22}\text{B}_{12}/\text{Si}$ film with major elemental peaks identified.

In this study, the elemental composition of all material systems were measured via *ex situ* XPS, specifically a Kratos™ Axis Ultra XPS with monochromated Al x-ray source. The excitation energy for this tool was 1486.6 eV and the electron takeoff angle was 90° with respect to the sample surface. Survey spectra were taken with a pass energy of 160 eV with a step size of 1 eV. High resolution detail scans were taken with a pass energy of 20 eV with a step size of 0.1 eV. The survey scan is first calibrated with the known value of the C-C 1s peak (284.6 eV). The composition can then be quantified by first determining the background of the scan, and then

integrating the area under each peak. The area for each peak corresponding to a core photoelectron is normalized with its respective relative sensitivity factor (R.S.F.). After the peak areas are normalized by their atomic sensitivity factors, they can be directly compared, giving a relative composition of the thin film. For Fe₆₆Ga₂₂B₁₂, the following peaks show the greatest intensity within the limits of the XPS system: Fe 2p, Ga 2p, and B 1s. Scans for C 1s and O 1s are generally performed as well to account for the peak shifting. Table 1 lists the ASF values and binding energies for these peaks.

Table 2-5. Binding energies and R.S.F factors for Fe 2p, Ga 2p, B 1s, C 1s and O 1s

Element	Binding Energy (eV)	R.S.F.
Fe 2p	706.7	2.957
Ga 2p	1115.5	5.581
B 1s	190.3	0.159
C 1s	284.6	1
O 1s	531.6	2.93

Binding Energy = Energy required to remove a core shell electron; Unit: eV
R.S.F = Relative Sensitivity Factor; Unitless

The depth-dependent composition of a 3 BL sample with the structure (20 nm FeGa/15 nm NiFe)₃/20 nm FeGa/Si was measured via XPS with argon sputtering to determine both the composition and amount of intermixing in metallic multilayers. An example of the attenuation of the Ga 2p_{1/2} and 2p_{3/2} oxide peaks as a function of etch time can be seen in Figure 2-7.

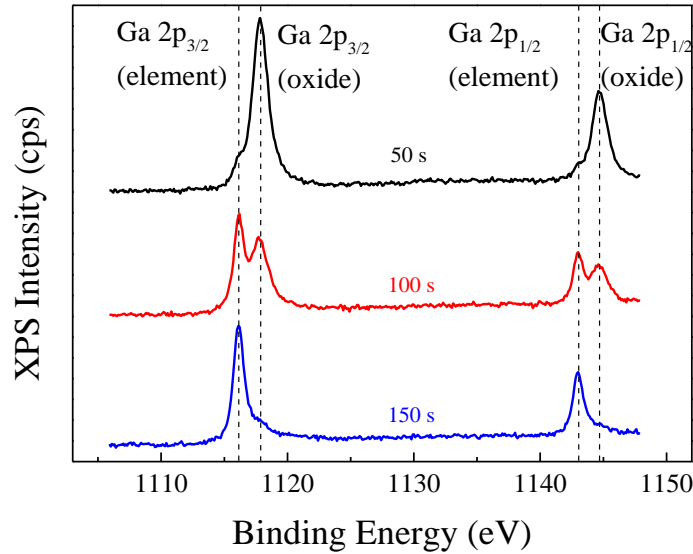


Figure 2-7. XPS detail spectra of Ga 2p peak with increased sputtering time, resulting in the removal of native Ga_2O_3 oxide for a FeGa/NiFe multilayer sample with the structure (20 nm FeGa/15 nm NiFe)₃/20 nm FeGa/Si

A +4 keV bias was applied to the bilayer sample in 50 second increments to remove the native oxide layer of FeO_x (likely some mix of Fe_2O_3 and FeO) and Ga_2O_3 that formed on the sample when exposed to atmospheric conditions after deposition. At 150 s of etch time, the native oxide is completely removed and so the composition of the film can be determined by fitting and comparing the areas of the elemental peaks.

2.2.2 X-ray Diffraction

X-ray diffraction is a technique used to analyze the structure of a crystal. The crystalline atoms cause an incident x-ray to scatter into many different directions depending on the orientation of the crystal. A detector can measure the intensities of the scattered x-rays as a function of angle, which correspond to specific crystallographic information of the material.

Crystals are periodic arrangements of atoms, and when an incident EM wave (x-ray) strikes the electrons of those periodic atoms, it produces regular spherical waves in a process

known as elastic scattering. The resulting spherical waves cancel each other out in most directions via destructive interference, but a few add constructively in specific directions, which can be represented via Bragg's law.

$$2d \sin \theta = n \lambda \quad (2.2)$$

Where d is the spacing between the diffracting planes, θ is the angle at which constructive interference was observed (higher intensity), n is any integer and λ is the wavelength of the incident x-ray, usually on the order of 1-100 Å. A diagram of scattering via Bragg's law can be seen in Figure 2-8. The incident x-ray is scattered by the electrons of the atoms in the material. If the x-rays are scattered in the same way (caused by the periodic nature of the lattice) then they add constructively, producing a reflection in the diffraction pattern (Jensen 1989). The angle at which the reflections occur is catalogued by the Joint Committee on Powder Diffraction Standards (JCPDS), which maintains a database containing powder diffraction information for over 500,000 materials. The right pane of Figure 2-8 shows the XRD spectra of Fe₆₀Ga₂₅B₁₅, the main peak being the Fe [110], corresponding to a Fe (bcc) structure, where Ga replaces Fe atoms substitutionally. Scherrer's equation can be used to determine the mean crystalline grain size, τ , in the film using the full width at half of the maximum, β , of a corresponding peak.

$$\tau = \frac{K \lambda}{\beta \cos \theta} \quad (2.3)$$

K is a dimensionless shape-factor, which is selected based on the geometry of the material. For polycrystalline thin films, K equals 0.89, which corresponds to spherical grains. The x-ray wavelength, λ , used in all of these studies is 1.54 Å and θ is half of the angle where the peak emerged. A 100 nm Fe₆₀Ga₂₅B₁₅ thin film has a strain of 3.3% and a grain size of 2.5 nm.

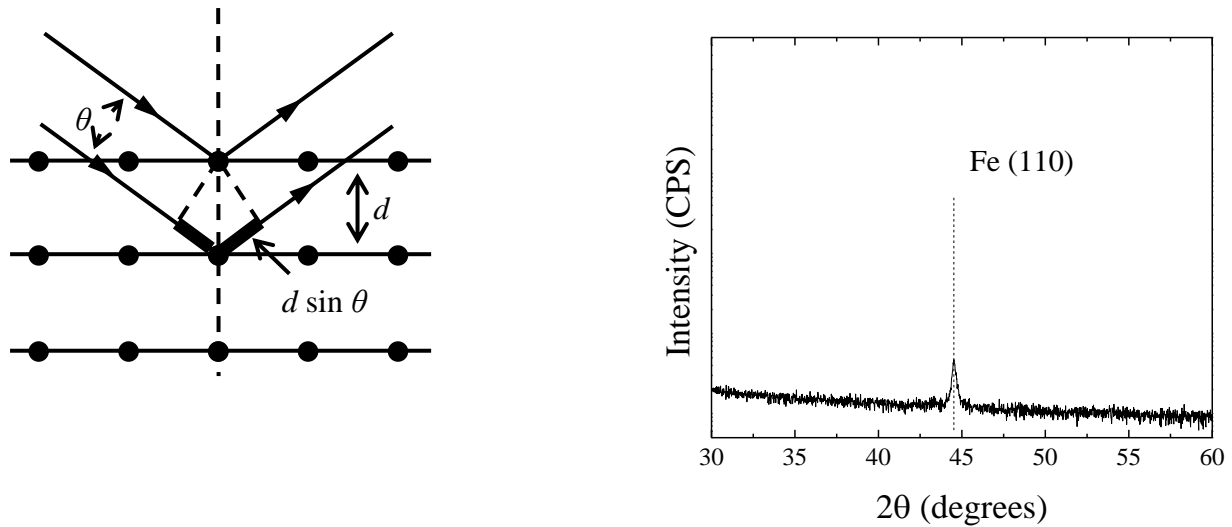


Figure 2-8. (Left) Schematic of Bragg diffraction in a single crystal and (right) XRD scan of a 100 nm $\text{Fe}_{60}\text{Ga}_{25}\text{B}_{15}$ with the Fe [110] peak indicated.

2.2.3 Profilometry

Profilometry is a technique for directly measuring the thickness of thin films. The principle of operation is very simple: a diamond-tipped stylus moves along the surface of the film for a specified distance and contact force and changes in position depending on the surface features. This change in position generates an analog signal that is converted to a digital signal, giving the height and depth of the film features. A schematic of this process can be seen in Figure 2-9.

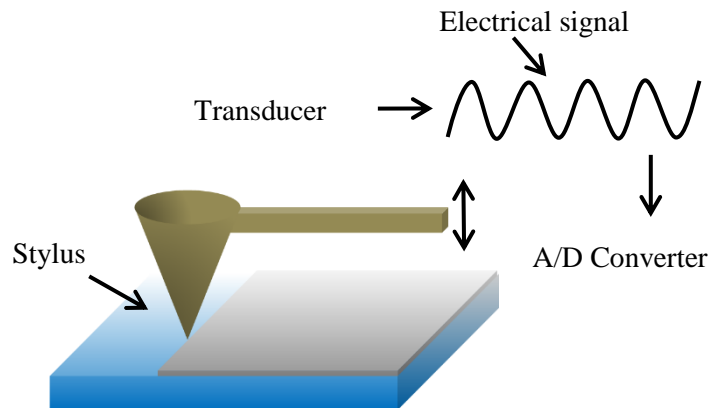


Figure 2-9. Schematic of contact profilometry of a thin film.

A profilometer can measure features ranging from 5 nanometers – 1 millimeter and the resolution of is determined by the speed of the stylus, the diameter and the force. The diameter of the stylus determines the minimum measurable width and the force it uses during a scan must be adjusted depending on the material being measured. A Veeco™ Dektak Surface Profilometer was used for the thickness measurements in this work. The stylus diameter was 12.5 μm and the force applied during the measurements was 10 mg. A sample measurement for a 50 nm FeGa film grown on Si can be seen in Figure 2-10. To secure the samples during depositon, Kapton™ tape was used, which also formed an edge of the film that could be used to measure the thickness. All films were cleaned with isopropyl alcohol (IPA) to ensure the adhesive was removed before the measurement.

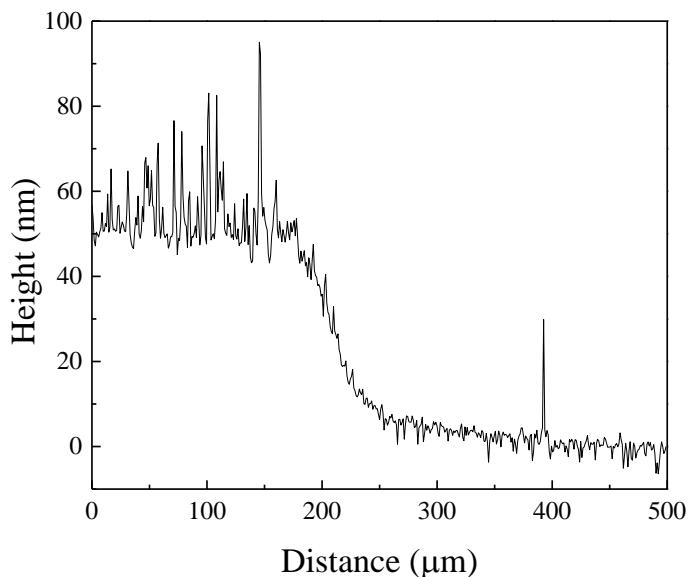


Figure 2-10. Normalized thickness data taken using profilometer for $\text{Fe}_{75}\text{Ga}_{25}/\text{Si}$ corresponding to a thickness of 50 nm.

The raw data for this technique tends to have large outlier values that increase the signal noise due to sample imperfections or even particulate matter, but in cases such as this, the average height is clear amongst the noise.

2.2.4 Atomic Force Microscopy

Atomic force microscopy (AFM) is a high-resolution technique used to probe the surfaces of different materials with sub-nanometer resolution. The method of operation is relatively simple: an atomically sharp tip is dragged along a surface, and as the surface morphology changes, the position of a laser beam focused on the top of the tip also changes, which is measured by a photodiode. The tip itself is often made from a very hard material, such as SiC, so that it is not deformed by the sample itself. A simple diagram of its operation can be seen in Figure 2-11.

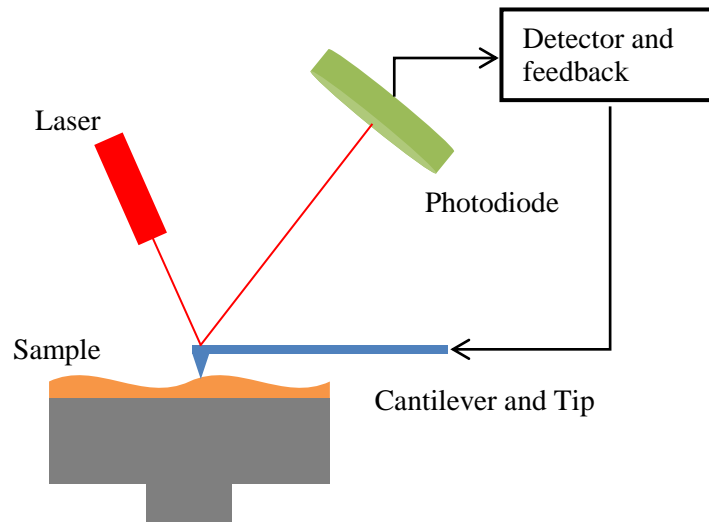


Figure 2-11. Illustration of atomic force microscopy, where the small deflections in the position of the cantilever are captured by the change in position of a laser.

This measurement technique is versatile because it can be used on a variety of different materials, as it is most commonly used in ambient conditions. There are several different modes in which the AFM can operate, but the two most common are contact mode and tapping mode.

When operating in contact mode, the tip is dragged across the surface, and in tapping mode, the tip is driven to oscillate up and down by a piezoelectric element (Rugar 1990).

For this work, a Bruker™ Dimension Icon Scanning Probe Microscope was used, with SiN probes with a tip diameter of 600 nm. The measurements were performed over areas ranging from 1 μm^2 to 100 μm^2 . The raw data for the image includes a background, which must be removed before quantifying the surface roughness. An example of a scan with the background removed can be seen in Figure 2-12.

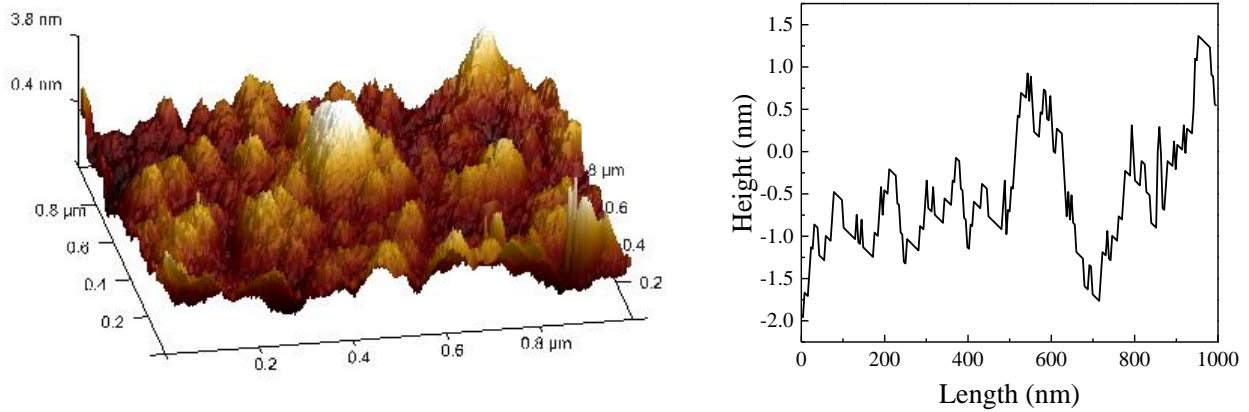


Figure 2-12. (Left) Normalized AFM image of a 50 nm FeGaB film deposited on Si over a 1 μm^2 area and (right) an extracted line scan.

Based on this scan, the surface roughness of the 1 μm^2 sample was determined to be 0.5 nm. The surface roughness was calculated using the following equation, where Z_i is the height of an individual spot, and Z_{ave} is the average height.

$$RMS = \sqrt{\frac{\sum (Z_i - Z_{ave})^2}{N}} \quad (2.4)$$

2.3 Magnetic Characterization

2.3.1 Magneto-optic Kerr Effect Spectroscopy

Magneto-optical Kerr Effect (MOKE) microscopy is an extremely sensitive technique for analyzing the surface magnetization of very thin films. The magneto-optic Kerr effect describes the change in the polarization of incident light based on the magnetization of the material. The reflectivity of a material is determined by the forced motion of electrons due to the electrical field generated by the incident light. If the material is magnetized, the force on the electrons is augmented by a Lorentz force.

$$\bar{\mathbf{F}} = q(\bar{\mathbf{E}} + \bar{\mathbf{v}} \times \bar{\mathbf{B}}) \quad (2.5)$$

Linearly polarized light experiences a rotation of the polarization plane (Kerr rotation, ϕ_k) as well as a phase difference between the electric field components both parallel and perpendicular to the plane of incident light, (Kerr ellipticity, ε_k), which forms the complex Kerr angle.

$$\phi_K = \theta_K + i\varepsilon_K \quad (2.6)$$

The interaction of the electromagnetic field and the magnetic material can be represented by the dielectric tensor, ε , and its diagonal and off-diagonal elements, ε_{xx} and ε_{xy} , respectively.

$$\phi_K = \theta_K + i\varepsilon_K = \frac{i\tilde{\varepsilon}_{xy}}{\sqrt{\tilde{\varepsilon}_{xx}(1-\tilde{\varepsilon}_{xx})}} \quad (2.7)$$

The off-diagonal elements of the tensor are linearly dependent on the magnetization of the material and describe the magneto-optic contributions to the tensor, caused by both spin orbit coupling and spin polarization. Thus, the change in the rotation in polarized light, or Kerr

rotation, reflects the changing magnetization of the material, though the saturation magnetization cannot be quantified from this technique (Qiu 2000).

A MOKE microscopy setup consists of a large electromagnet, polarized light source and a detector. A magnetometer is often employed for calibrating the current applied to the magnet to an induced field. The sample is placed in the electromagnet, and the light source is incident on the sample. A magnetic field is swept while the polarization of the reflected light is measured. The Kerr rotation changes linearly with the magnetization of the sample, and thus a magnetic hysteresis loop is generated. The MOKE setup used for this work utilizes an electromagnet capable of fields up to 0.7 T and a 525 nm laser. A schematic of this setup can be seen in Figure 2-13.

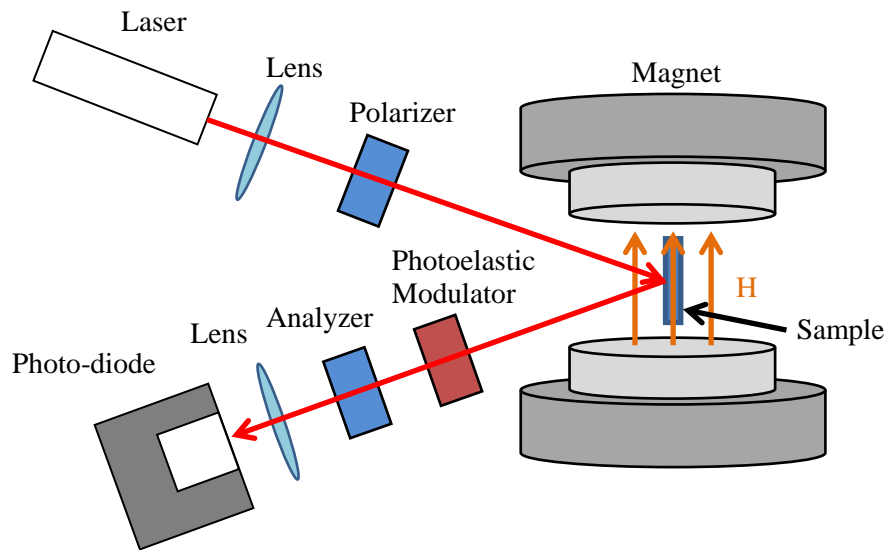


Figure 2-13. Schematic of a room temperature MOKE spectroscopy system set up for measuring in-plane magnetization.

It is important to note that the magnetization of the film cannot be quantified using MOKE spectroscopy, as the change in the polarization of the light is being measured, represented by the Kerr rotation. However, the saturation field, coercivity, and anisotropy field can be obtained using this method.

During a MOKE measurement, up to 20 scans are taken in order to minimize the signal-to-noise ratio. Additionally, at high fields, there is drift in the Kerr rotation, and so this can be accounted for during the data processing. Figure 2-14 shows an example of a normalized, in-plane, MOKE spectra for 200 nm $\text{Fe}_{60}\text{Ga}_{22}\text{B}_{18}/\text{Si}$, with a coercivity of around 80 Oe, and a saturation field of 600 Oe. Though data has had some corrections, there is still some crossover visible at the saturation value.

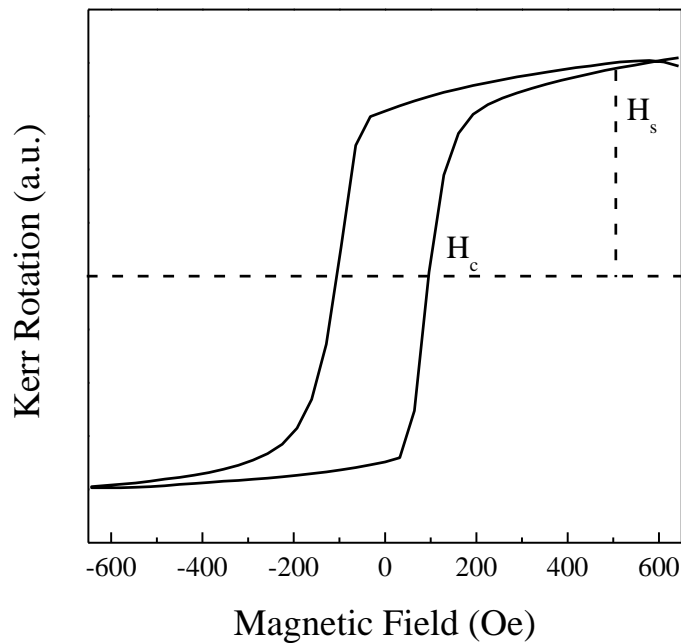


Figure 2-14. Normalized magnetic hysteresis for 200 nm $\text{Fe}_{60}\text{Ga}_{22}\text{B}_{18}/\text{Si}$, with the coercivity H_c and saturation field H_s indicated on the plot.

Another technique that relies on the magneto-optic effect utilizes magneto-optic indicator film, most commonly bismuth-doped yttrium iron garnet (Bi:YIG). This film has a strong in-plane easy axis, which allows it to interact with the fringe fields of the edges of the domains in the material. Due to the magneto-optic Faraday effect (described in the previous section) in the indicator film, these edges can be observed with polarized light microscopy. This technique offers the ability to image domain formation and propagation, which can reveal subtleties

regarding the film's anisotropy. An image of the magnetic domains for a sample with the structure (5.5 nm FeGa/6.3 nm NiFe)₈/5.5 nm FeGa/Si is shown in Figure 2-15.

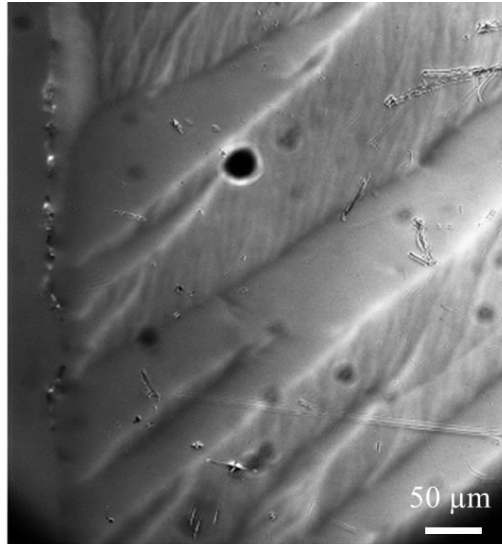


Figure 2-15. Image of the magnetic domains in a (5.5 nm FeGa/6.3 nm NiFe)₈/5.5 nm FeGa/Si sample indicating domain size of 100 μm or larger.

By performing time-resolved measurements, the reversibility of the domain formation can be observed, which is critical for device integration. Within the scope of this work, this technique was used to compare the size of in-plane domains for samples with varying layer thickness.

2.3.2 Superconducting Quantum Interference Device Magnetometry

Superconducting Quantum Interference Device (SQUID) magnetometry is a powerful technique that can be used to measure very small magnetic fields. The technique is based on the Josephson Effect, via superconducting loops, combined with the known quantization of magnetic flux in a fixed area.

The Josephson Effect occurs where two superconductors are separated by a thin non-superconducting layer and electrons are able to tunnel through it without losing energy. When a

metal is at a temperature above the superconductor transition temperature, electrons have a net repulsive effect. When the metal is cooled below the superconductor transition temperature, electrons become slightly attracted, due to the interactions with the ionic lattice of the material. The slight attraction allows electrons to transition to a lower energy state, and they can move through the ionic lattice without being scattered, which is the origin of electrical resistance. Thus, Cooper pairs of electrons can tunnel through a non-superconducting layer without any energy loss. If this current exceeds some critical value, a time-dependent AC voltage develops across the junction. An important note is that superconducting materials expel all magnetic fields.

A DC SQUID consists of a loop with two Josephson junctions (superconductor/non-superconductor/superconductor) in parallel disrupting the loop, as shown in Figure 2-16.

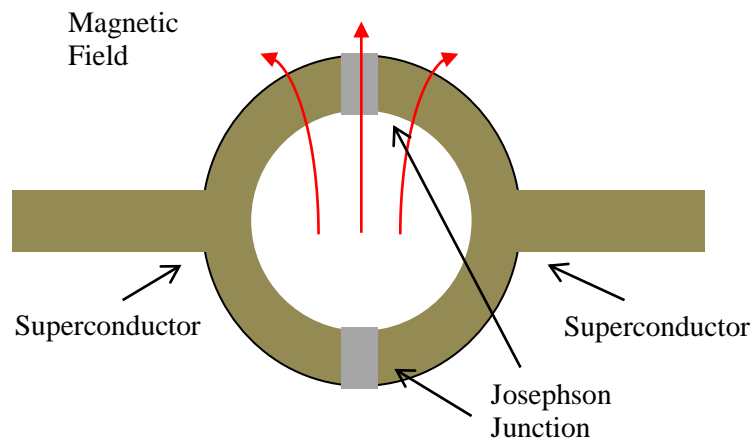


Figure 2-16. SQUID loop made of a superconductor with two Josephson junctions separated by thin insulators.

An RF loop may be constructed from one Josephson junction, but it is less sensitive than DC. For DC, a current, I , is applied to one side of the loop, which is split between the two branches of the loop equally. If a small magnetic field is applied, a screening current is generated

to cancel this, as the superconducting material expels any magnetic field. This current adds to the current in one branch, and subtract from the current in the other.

$$\begin{aligned} I_1 &= I/2 - I_s \\ I_2 &= I/2 + I_s \end{aligned} \quad (2.8)$$

As the magnitude of the applied field increases, eventually the critical current is reached, after which, an AC voltage appears across the Josephson junction. If the applied magnetic field exceeds $\phi_0/2$, which is half magnetic flux quantum, it is energetically favorable to increase the magnetic flux, so the screening current reverses. The magnetic flux quantum is represented by the following equation, where \hbar is Planck's constant and e is the charge of an electron.

$$\phi_0 = \frac{2\pi\hbar}{2e} = 2.0678 \times 10^{-15} \text{ tesla} \cdot \text{m}^2 \quad (2.9)$$

Thus, the screening current oscillates as a function of magnetic flux. If a constant bias current is maintained in the SQUID magnetometer, the voltage oscillates at the two junctions. These oscillations are counted and are correlated to a magnetic flux that is applied to the sample. The change in voltage, ΔV , is a function of the shunt resistance, R , the inductance of the loop or coil, L , and the change in magnetic flux quantum (Lueken 2012).

$$\Delta V = \left(\frac{R}{L} \right) \Delta\phi \quad (2.10)$$

In the SQUID setup, the sample is placed between two electromagnets, and moved up and down to increase the applied field. Two pickup coils surround the sample and measure the voltage caused by the applied flux from the sample. SQUID magnetometry can be used to determine the magnetic coercivity, saturation field and saturation magnetization of thin magnetic films.

An MPMS® (Magnetic Property Measurement System) XL tool made by Quantum Design was used for this work. It is capable of fields +/- 5 Tesla and can resolve down to 6×10^{-7} emu at room temperature. There are three modes for how the electromagnet sets the field: no overshoot, oscillate, and hysteresis. No overshoot mode is important for initial magnetization measurements, as it first reaches 70% of the setpoint, then 70% of the remainder until it reaches the desired field. Oscillate mode approaches the field in a sinusoidal fashion, decreasing the amplitude until it reaches the desired field, which is useful for minimizing the magnetic flux settling in the superconducting electromagnet. Hysteresis mode operates in a persistent-current mode, where the current is swept as the field is measured, and so it is rapid, but only useful for samples with moments greater than 10^{-5} emu and the field value may vary by up to 1% from the setpoint. In this work, no overshoot and hysteresis modes were primarily employed.

The tool measures the total magnetization of the sample, and so to obtain a value for the saturation magnetization, the volume of the sample must be measured. Additionally, since the majority of the samples in this work were grown in silicon substrates, there is a large diamagnetic (negative linear slope) or paramagnetic component (positive linear slope) in the raw data. This can be removed by fitting the linear diamagnetic component and subtracting it from the magnetization. Figure 2-17 shows an example of a normalized magnetic hysteresis obtained for FeGa.

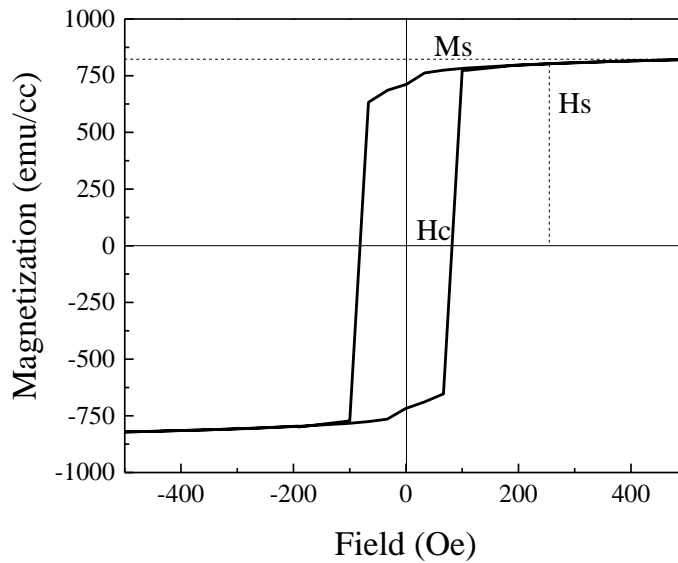


Figure 2-17. Normalized in-plane magnetic hysteresis for a 100 nm $\text{Fe}_{65}\text{Ga}_{20}\text{B}_{15}/\text{Si}$ with H_c , H_s and M_s indicated.

Adjusting the samples position relative to the magnetic field allows for out of plane scans to be acquired. The magnetization value is determined by normalizing the measured moment by the sample volume, which is based on its length, width, and the thickness as measured by profilometry.

2.3.3 Vibrating Sample Magnetometry (VSM)

VSM is a technique where the bulk magnetization of the sample is measured by detecting a moving electric field inducing by the vibrating of a magnetized sample. A magnetic material is vibrating sinusoidally in a uniform magnetic field and a voltage is induced in sensing coils near the sample. This voltage is proportional to the magnetic moment of the material being measured. A schematic of this technique can be seen in Figure 2-18.

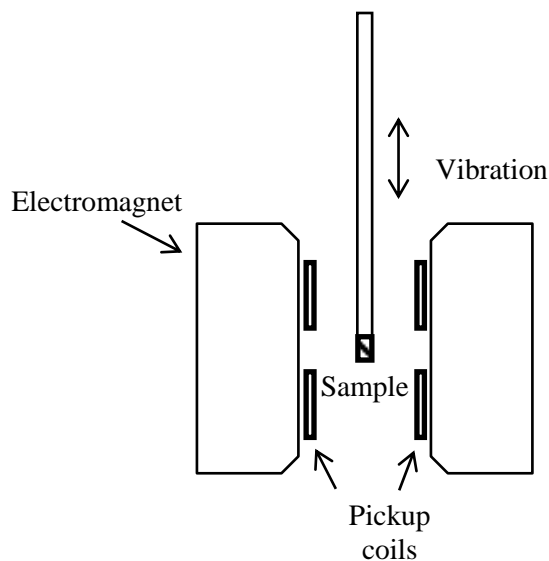


Figure 2-18. Schematic of vibrating sample magnetometry with sample centered between pickup coils placed on the faces of the poles of the magnet.

The induced electromotive force (*emf*) is amplified with a lock-in amplifier, which is sensitive to signals at the vibration frequency, usually 100 Hz or less. A piezoelectric material is commonly used as a voltage reference at the frequency of vibration. By simultaneously measuring the field produced by the electromagnet, the magnetic hysteresis can be measured (Cullity 2009). Several measurement factors can be varied in the measurement that have an impact on the final hysteresis. The time constant indicated the length of time that each point is measured, therefore, a higher constant has a higher sensitivity, but the experiment takes a much longer time. Another important factor for these types of measurements is the centering procedure. The centering procedure in VSM is fundamentally similar to that of SQUID magnetometry: the position of the sample is adjusted to maximize the induced voltage. However, for VSM measurements, the centering is commonly done with positioning screws, which introduces the possibility of human error. Poor centering in either measurement can lead to non-physical hysteresis loops (Jin 2007).

In this work, a Lakeshore™ 7400 series VSM was used for more detailed analysis of in-plane and out of plane magnetic measurements. With a time constant of 10 s/pt, the tool is sensitive to 10^{-7} emu, similar to that of SQUID magnetometry. The tool features a goniometer integrated into the linear actuator that provides the vibration, allowing for angle-resolved magnetic hysteresis measurements. Data processing is similar to that of SQUID magnetometry, where the diamagnetic or paramagnetic linear component is removed by determining the slope of the linear portion of hysteresis after saturation.

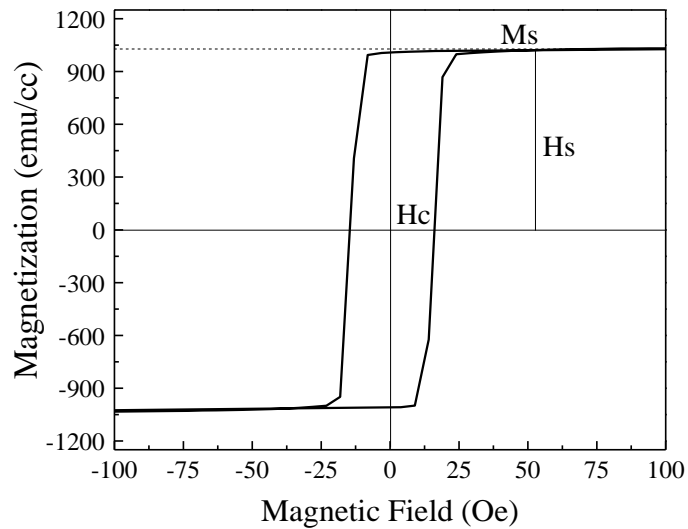


Figure 2-19. Normalized in-plane hysteresis measurement of a 25 nm FeGa/50 nm NiFe/25 nm FeGa/Si sample measured by VSM with coercivity, saturation magnetization and field indicated.

2.3.4 Electron Spin Resonance (ESR) Spectroscopy

ESR is a technique used to probe unpaired electrons. The Zeeman effect describes how a spectral line splits in the presence of a magnetic field, based on the spin states of the electrons. The sample to be probed is placed into a resonant cavity, and it is excited with a fixed frequency (typically X band, 9.7 GHz), while a large magnetic field is swept over the sample. When the

magnetic field induces a frequency equal to that of the applied microwave, there is an increase in absorption, indicating the resonant field.

The energy of an electron, E , is a function of the spin state, m_s , which has a value of $+1/2$ for parallel or $-1/2$ for antiparallel state, the g-factor, g_e , the Bohr magneton, μ_B , and the strength of the applied magnetic field, B_0 .

$$E = m_s g_e \mu_B B_0 \quad (2.11)$$

The g-factor is a dimensionless quantity that allows for the relation of the magnetic moment to the appropriate angular momentum quantum number. This is known to be approximately 2 for a free electron, but as the number of shells increase (i.e., Z increases) the value changes due to spin-orbit interactions. This is especially true for ferromagnetic elements, as the origin of magnetism lies in spin-orbit coupling.

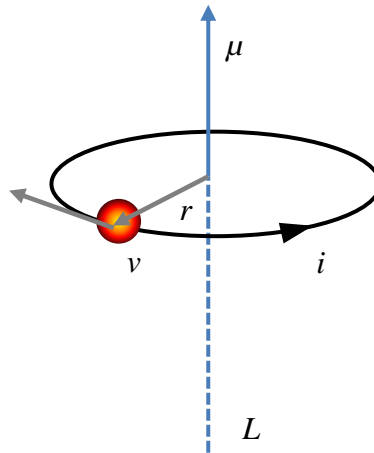


Figure 2-20 Precessional motion of an electron under an applied magnetic field.

Since electrons either occupy a parallel ($+1/2$) or antiparallel state ($-1/2$), and they have the same Bohr magneton, g-factor, and applied magnetic field.

$$\Delta E = E_{+1/2} - E_{-1/2} = g_e \mu_B B_0 \quad (2.12)$$

The electrons in the film follow a Maxwell-Boltzmann distribution, meaning that most lie in a lower energy level. When the microwave excites the electrons in the sample, it causes a

large increase in absorbed energy as read by the detector. This excitation occurs at the magnetic field that induces a resonant frequency equal to that of the microwave, as energy is quantized.

$$\Delta E = h\nu = g_e \mu_B B_0 \quad (2.13)$$

This technique can be used to estimate the ferromagnetic resonant (FMR) linewidth of magnetic materials, as the origin of magnetism lies in the spin-orbit coupling of electrons of different energy levels. When a ferromagnetic material is magnetized, the domains within the material begin to precess. Precessional motion describes the change in orientation of the rotational axis in a rotating body, and the Larmor precession is the point at which magnetic domains in a material precess at the same frequency under an applied magnetic field. When this frequency matches that of the microwave, the material absorbs the energy. Thus, the resonant field linewidth can be estimated from this technique using the gyromagnetic ratio (2.8 MHz/Oe).

A Bruker™ EMX system was used for these experiments, which has a field range of up to 1.2 T. The cavity is sized to allow for a standing wave at X band (9.7 GHz). In order to allow for the standing wave, the experimental parameters must be tuned according to the procedure indicated in Appendix A.4. The measurements are performed at ambient pressure and room temperature, though low temperature measurements are possible with liquid nitrogen.

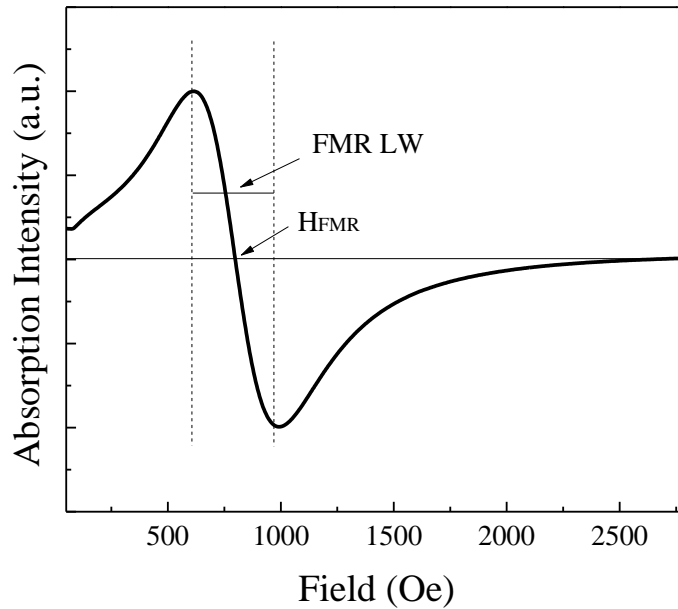


Figure 2-21. ESR spectra for $\text{Fe}_{65}\text{Ga}_{20}\text{B}_{15}$ (100nm)/Si, where the resonance field is around 600 Oe and linewidth is 350 Oe.

Once the measurement is taken, the absorbance of the plot should be normalized, so that spectra of varying samples can be easily compared. By depositing the substrate on a piezoelectric material, such as PMN-PT (011), and applying a strain-inducing voltage, the resonant field can be tuned. The results of this are discussed in Section 4.2 and the procedure is discussed in Appendix A.4.

2.3.5 Stripline Measurement for Permeability

Magnetic permeability of thin films can be measured by a stripline method, which works by applying an EM wave to a ferromagnetic film on a resistive substrate. The scattering parameters, or S-parameters, are used to calculate the transmission constants, and then these values can be used.

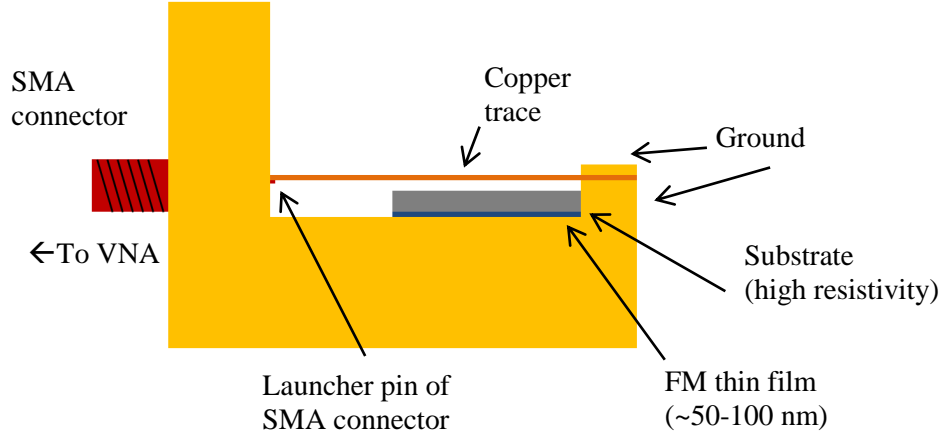


Figure 2-22. Schematic of stripline measurement system for frequency-dependent permeability measurements.

This technique works by creating a short circuit on the stripline setup, where the EM wave short to ground. The general technique for this measurement involves conformal mapping –an effective permeability for the entire cavity must be determined (Wu 2010). First, the vector network analyzer (VNA) must be calibrated with an empty cavity to assess the background S-parameter of the cavity. This is then repeated for the bare substrate (Si with $\Omega > 10,000$ ohm-cm) and then the substrate with the film. The transmission constants, γ_1 and γ_2 , can then be used to determine the effective permeability.

$$\gamma_1 = \gamma_0 - \frac{1}{2l} \ln \left(\frac{S_{11}^{sub}}{S_{11}^{empty}} \right) \quad (2.14)$$

$$\gamma_2 = \gamma_1 - \frac{1}{2l} \ln \left(\frac{S_{11}^{film}}{S_{11}^{sub}} \right)$$

The transmission coefficients represent the enhancement of the permeability with the addition of the substrate first, and then the magnetic film. The effective permeability is calculated with the following equation.

$$\mu_{eff} = \left(\frac{\gamma_2}{\gamma_1} \right)^2 \quad (2.15)$$

Once this value is determined, the technique of conformal mapping can be employed to extract the permeability for the thin film. The effective permeability can be expressed as a function of the permeability and permittivity of the entire cavity, as shown in Figure 2-23.

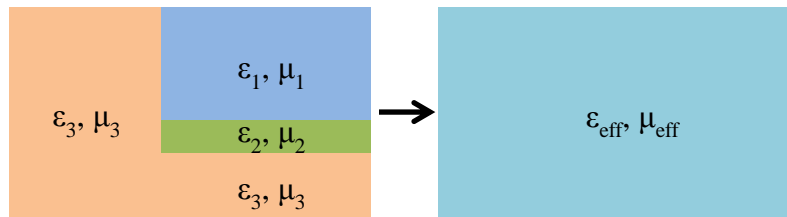


Figure 2-23. Individual permeabilities of the cavity/substrate/film in terms of an effective permeability.

Based on the effective dimension and permittivity of the rest of the cavity, the permittivity and permeability of the thin film can be calculated. These measurements can be performed with an electromagnetic to observe the dependence of the FMR on applied field.

2.3.6 Neutron Reflectometry

Electromagnetic radiation of varying wavelengths (from 10^{-6} to 10^{-10} m) is utilized in the majority of the techniques described thus far, but has limitations due to the penetration depth of these techniques. One method that allows for the characterization of the atomic structure of thicker samples is few neutron reflectometry, where a neutron beam is reflected on the surface of a sample and the intensity of the reflection is measured as a function of angle, or Q . By spin-polarizing the neutron beam, this technique has been able to reveal the subtleties of depth-dependent magnetization in thin films.

Polarized neutron reflectometry (PNR) relies on the interactions between the spin of an incident polarized neutron and the magnetization in the sample. A simple schematic of this technique can be seen in Figure 2-24.

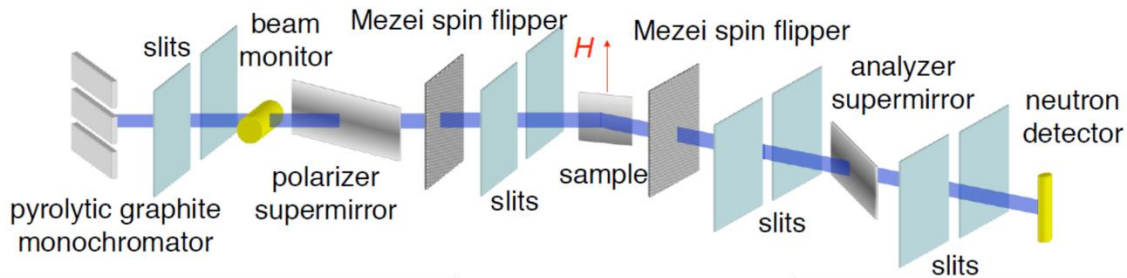


Figure 2-24. Schematic of polarized beam reflectometry setup at the National Institute for Standards and Technology’s Center for Neutron Research (NCNR) *image courtesy of NCNR.*

A collimated beam of neutrons is polarized via a supermirror, where non-magnetic/magnetic bilayers of various thicknesses reflect only spin-up neutrons. These neutrons are then directed at a low Q ($Q = 4\pi \sin \theta / \lambda$) to the sample, which is under some magnetic field. After interacting with the sample, the neutrons are then polarized again to filter out spin-down states via supermirror and the remaining spin-up neutrons are detected. The spins of the neutrons can be controlled via spin flippers placed on either side of the sample. By activating one or the other flipper, the “spin-flip” scattering of the sample can be assessed, a measure of how the neutrons’ spins are flipped by interacting with the sample itself. A schematic of this can be seen in Figure 2-25. Non-spin flip (NSF) scattering measurements are sensitive to the moments in the film that are parallel to those of the neutrons, which have not been flipped by interacting with the magnetization of the sample. NSF measurements are performed under a saturating magnetic field with both of the spin flippers on or off. Spin-flip (SF) measurements are sensitive to moment’s perpendicular to those of the incident neutrons, which have been flipped by interacting with the

sample. SF measurements are taken at a small remnant magnetic field with only one of the spin flippers activated.

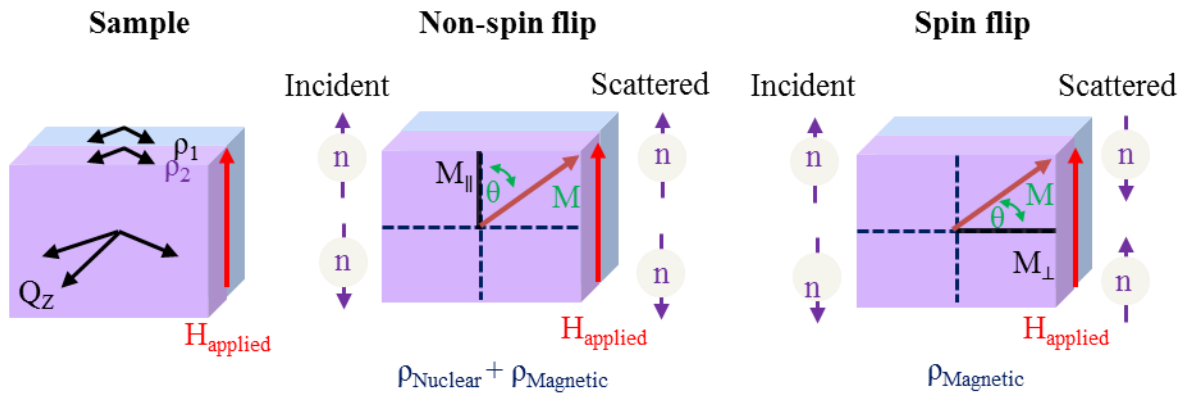


Figure 2-25. Schematic sample position (left) non-spin flip (center) and spin-flip scattering (right) occurring in PNR experiments. Each layer has a nuclear and magnetic scattering length density (ρ or SLD) and the angle of magnetization ($\theta_{\text{magnetization}}$) is determined by fitting the model.

These measurements can be taken sequentially for a given magnetic field and fixed Q so that the range of interactions between the neutrons and the material can be assessed. Similar to other reflectivity measurements, the data taken for these measurements show oscillations, caused by the interface of areas of different scattering length density, as shown below, which are fitted to reveal information about the magnetization of each layer.

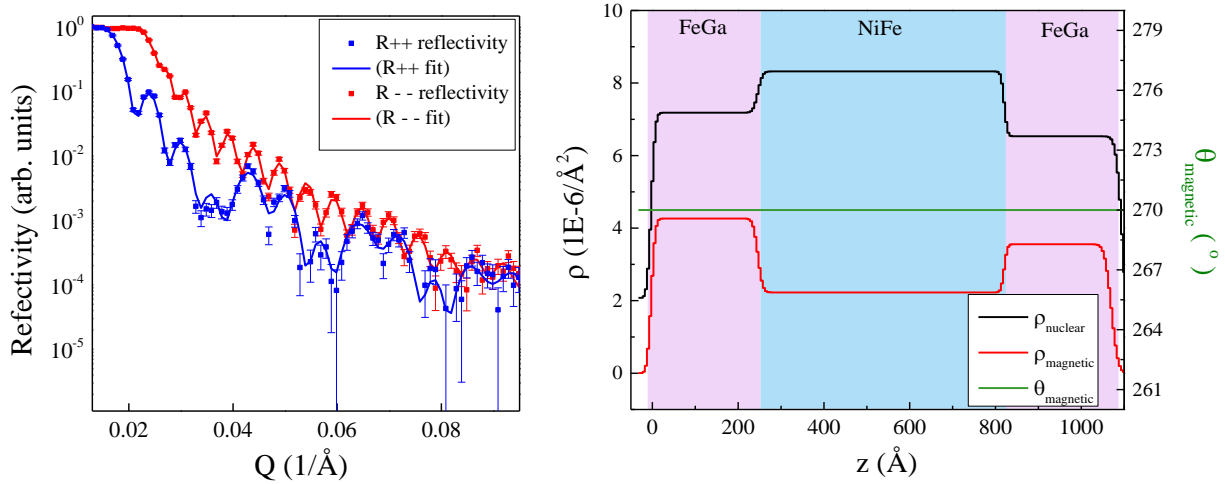


Figure 2-26. (Left) Fitted reflectivity for a 25 nm FeGa/50 nm NiFe/25 nm FeGa sample and (right) the corresponding scattering length density profile generated from the fit.

The data processing for this technique relies on a physical model to which the data can be fitted. The parameters that are used for the fit include the following: nuclear scattering length density, magnetic scattering length density, magnetization direction, layer thickness, and interfacial roughness. Each element has a unique nuclear scattering density length (ρ or SLD), which describes the scattering power of a material. This parameter decreases with increasing physical density. The magnetic scattering length density increases with increasing magnetization, but can vary more dramatically than the nuclear SLD depending on the proximity to other layers. Using an iterative fitting process, the magnetic structure of complex films can be determined. A more detailed discussion of the fitting process is discussed in Appendix B.

2.4 Multiferroic Device Characterization

2.4.1 Magnetostriction

This technique can be used to measure the magnetostriction of thin ferromagnetic films. The film to be measured can be deposited on a single-crystal piezoelectric substrate, such as

oriented PMN-PT, and a voltage can be applied through the substrate, inducing a known strain in the film. A diagram of the substrate and poling apparatus can be seen below in the left panel and an example of a strained and unstrained hysteresis loop can be seen in the right panel.

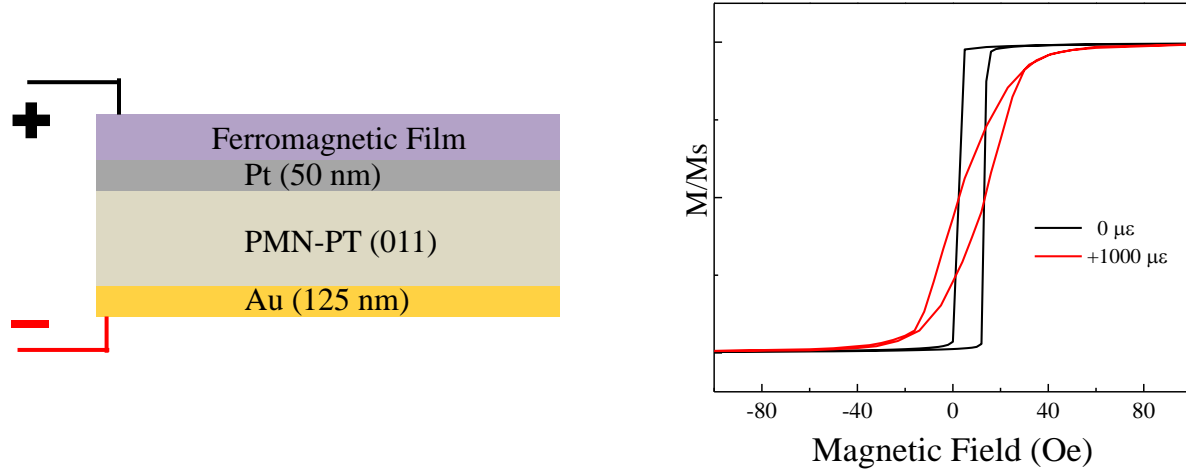


Figure 2-27. (Left) Schematic of ferromagnetic thin film deposited on PMN-PT (011) substrate and (right) normalized strained and unstrained hysteresis loops for a 25 nm FeGa/50 nm NiFe/25 nm FeGa sample.

Changes in coercivity can be correlated to the magnetostriction with knowledge of the strain induced by the piezoelectric material and its modulus, as well as the saturation magnetization of the material. The value for magnetostriction can be calculated with the following equation.

$$\mu_0 M_s H_c = \frac{3}{2} \lambda_s E (\varepsilon_y - \varepsilon_x) \quad (2.16)$$

M_s , H_c , and λ_s represent the saturation magnetization, coercivity and saturation magnetostriction respectively and have been discussed in Section 1.3. E represents the Young's Modulus for PMN-PT and ε_x and ε_y represent the x and y components of piezostrain. Another approach for determining the saturation magnetostriction, Matlab™ was used to extract the magnetoelastic energy from the difference in the strained and unstrained magnetic hysteresis

loops. The same principle can be applied to a 4-point bend test, where a deflection in a piece of Si (100) oriented wafer can be correlated to a strain via strain gauge, as the Young's modulus of the film is negligible compared to the substrate (Hill 2013).

2.4.2 Surface Acoustic Wave Device Characterization

In order to effectively integrate a magnetic material into a multiferroic antenna, the frequency-dependence of the magnetoelastic behavior must be determined. Acoustically-driven ferromagnetic resonance (ADFMR) is a new technique that allows for the absorption of a strain wave via a magnetostrictive material to be measured. A strain wave is launched via IDTs in a piezoelectric substrate, which is absorbed by a ferromagnetic thin film. Any energy that isn't absorbed is measured by a second set of IDTs, and so the dynamic absorption of the material can be quantified. A schematic of this experimental setup can be seen in the left panel of Figure 2-28. When combined with the ability to rotate the applied magnetic field, absorption can be quantified as a function of angle. For a material that has in-plane magnetic anisotropy, 4-lobed absorption is expected with the maxima roughly at 45° , as seen in the right panel below.

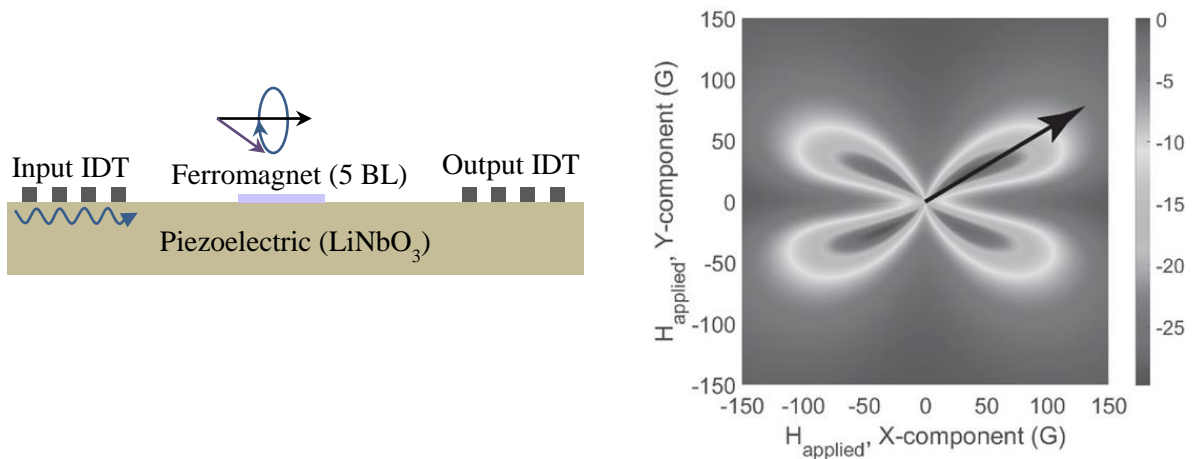


Figure 2-28. (Left) Schematic of ADFMR in a ferromagnetic material grown on LiNbO₃ and (right) a plot of the absorption of that acoustic wave as a function of applied magnetic field in the X and Y directions (Labanowski 2016).

The ability to extract the frequency-dependent magnetoelastic coefficient from these measurements is reliant on the film having in-plane magnetic anisotropy as well as the directional propagation of the strain wave in the Y-cut of LiNbO₃.

$$b = \frac{3}{k} \sqrt{\frac{(1 - |S_{21}|^2) MW}{2M_s \gamma \text{Im} \left\{ \frac{\omega_1}{\omega_1 \omega_2 - \omega^2} \right\}}} = \frac{-3\lambda\mu}{M_s} \quad (2.17)$$

The magnetoelastic coefficient (b) is a function of the transmission coefficient S_{21} as well as the saturation magnetization (M_s) and permeability (μ). In the scope of this work, the ADFMR was measured for a 5 BL sample, as it was shown to have the high permeability via stripline measurements as well as a large magnetostriction. A thin sample with the structure (4.2 nm FeGa/5 nm NiFe)₅/4.2 nm FeGa and a thick sample with the structure (8.3 nm FeGa/10 nm NiFe)₅/8.3 nm FeGa were measured using this technique.

2.4.3 Bulk Acoustic Wave Antenna Characterization

The bulk acoustic wave (BAW) antenna operates on the phenomena that is more critical to the functionality of a strain-coupled antenna: the conversion of an electromagnetic wave moving at the speed of light to an acoustic wave moving at the speed of sound. This is a substantially more difficult undertaking because it requires the absorption of an electromagnetic wave from free space via strain-energy from a substrate as is the case for SAW devices. Figure 2-29 shows a schematic of a cross-section of a BAW stack, where the ferromagnetic material is sandwiched between piezoelectric AlN and Al₂O₃. The right panel shows a colorized SEM top-down image of the actual BAW resonator, where the stack is suspended over an air cavity. Because of this design, the device is sensitive to the fabrication process, specifically, the residual stresses that occur in the films. BAW devices were fabricated on high-resistivity Si wafers, on

which a 700 nm thick AlN layer was deposited via reactive sputtering by an outside manufacturer. FeGa/NiFe multilayers were incorporated after initial patterning of the AlN, followed by a 700 nm Al₂O₃ deposition. The final fabrication step was the release of the resonators via isotropic etching of Si by XeF₂ gas at 2500 mTorr at 25°C with 8 etch pulses of 60 seconds. The devices were characterized initially with a stripline measurement system, specifically on S₁₁ (reflection) and S₂₁ (transmission) if the devices were still attached to the anchor points after release.

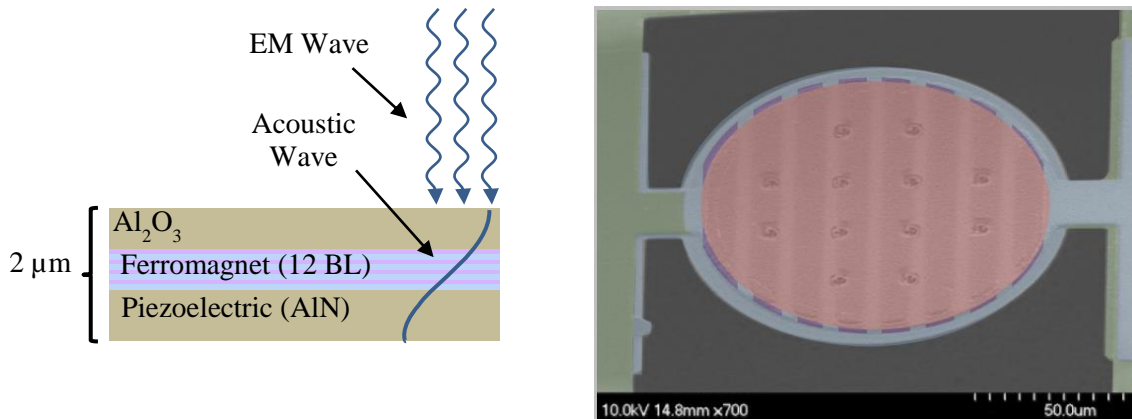


Figure 2-29. (Left) Schematic of cross-section of BAW stack in an antenna and (right) a top down SEM image of the BAW resonator device.

Characterization of the SAW device allows for the extraction of the frequency-dependent magnetoelastic coefficient, which is critical to the development of material candidates for this application. The BAW characterizations are the true measure of a material’s ability to operate in an antenna, that is, to convert an electromagnetic wave into an acoustic wave.

Chapter 3 : Growth and Characterization of Iron-Gallium-Boron

Doping was explored as a method for enhancing the soft magnetic properties, while maintaining the high magnetostriction of iron-gallium ($\text{Fe}_{75}\text{Ga}_{25}$). The addition of boron (up to 19%) to $\text{Fe}_{75}\text{Ga}_{25}$ reduced the magnetocrystalline anisotropy, enhancing the high frequency properties. The coercivity reduced by 80% with the addition of boron while maintaining 90% of the magnetization of $\text{Fe}_{75}\text{Ga}_{25}$. Electron spin resonance spectroscopy at X band (9.6 GHz) showed that the addition of boron reduced the FMR linewidth by up to 70% to a value of 210 Oe, and an increased thickness lead to a broader linewidth. Electrically poled hysteresis measurements showed that the $\text{Fe}_{65}\text{Ga}_{20}\text{B}_{15}$ film has a saturation magnetostriction of 50 $\mu\epsilon$, comparable in magnitude to literature reported value for a similar iron-gallium-boron composition of $\text{Fe}_{70}\text{Ga}_{18}\text{B}_{12}$.

3.1 FeGa

3.1.1 Growth and composition

Iron-gallium ($\text{Fe}_{75}\text{Ga}_{25}$) was synthesized via sputtering of a single target of $\text{Fe}_{80}\text{Ga}_{20}$ (at. %) at a power of 60 W and a pressure of 5 mTorr using argon as the working gas. Films with thickness ranging from 5 – 500 nm were grown with a growth rate of 6 nm/min, as determined by profilometry. Composition of the thin films of $\text{Fe}_{75}\text{Ga}_{25}$ were verified via x-ray photoelectron spectroscopy (XPS). A typical survey scans of $\text{Fe}_{75}\text{Ga}_{25}$ is shown in Figure 3-1. The relative ratios of the elements were determined by fitting the Fe 2p and Ga 2p peaks. The composition was determined to have a ratio of 3:1 for Fe:Ga.

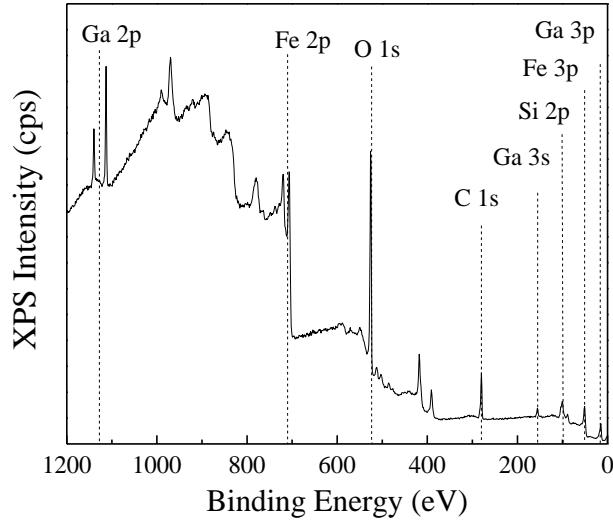


Figure 3-1. XPS survey scan of a 100 nm $\text{Fe}_{75}\text{Ga}_{25}/\text{Si}$ sample with elemental peaks indicated.

3.1.2 Magnetic Properties of FeGa

Superconducting quantum interface device (SQUID) magnetometry was used to measure the magnetic hysteresis of the $\text{Fe}_{75}\text{Ga}_{25}$. In-plane and out-of-plane hysteresis measurements were performed on 200 nm $\text{Fe}_{75}\text{Ga}_{25}$ films deposited on Si. For $\text{Fe}_{75}\text{Ga}_{25}$, in-plane measurements were taken from -5000 to 5000 Oe for in-plane measurements to gauge the coercive field, but did not reach magnetic saturation. The out-of-plane measurements were taken from -30 kOe to 30 kOe, well past saturation. Figure 3-2 shows that the $\text{Fe}_{75}\text{Ga}_{25}$ has a strong in-plane anisotropy. This is shown by a large difference in the saturation fields for the in-plane and out-of-plane measurements, which are approximately 5 kOe and 11 kOe, respectively. The in-plane and out-of-plane coercivities for $\text{Fe}_{75}\text{Ga}_{25}$ was found to be 140 Oe and 350 Oe, respectively. Saturation magnetization extracted from hysteresis measurements was found to be 873 emu/cc or 11 kG.

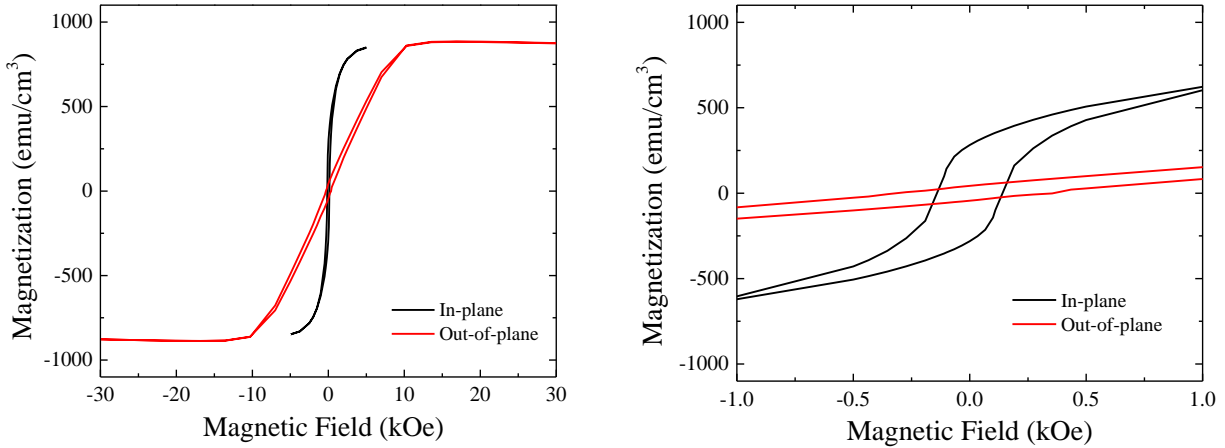


Figure 3-2. In-plane and out-of-plane magnetic hysteresis of a 200 nm $\text{Fe}_{75}\text{Ga}_{25}/\text{Si}$ (right is magnified to show coercivity).

Ferromagnetic resonance (FMR) linewidth was measured at X band (9.7 GHz) for magnetic fields sweeping from 100 – 6000 Oe. The FMR frequency is the point at which the precessional frequency of the magnetic domains in the material is equal to the frequency of the incident microwave. This causes the material to absorb the energy from the microwave. FMR linewidth was measured using electron spin resonance spectroscopy (ESR), which measures the FMR linewidth at X band (9.6 GHz). A 200 nm thick $\text{Fe}_{75}\text{Ga}_{25}$ film grown on a Si (100) substrate was measured and its linewidth was found to be 750 Oe with a resonant field of 666 Oe as shown in Figure 3-3. Other studies reported FMR linewidth values for 100 nm polycrystalline $\text{Fe}_{80}\text{Ga}_{20}$ films of 260 Oe, while some have reported as low as 77 Oe for 22 nm single-crystal $\text{Fe}_{81}\text{Ga}_{19}$ films (Lou 2009) (Parkes 2013). The 200 nm $\text{Fe}_{75}\text{Ga}_{25}$ film measured in this work had a large linewidth for two reasons: the polycrystallinity of the film, resulting from room temperature depositions and the fact that the films were thicker compared to those mentioned previously.

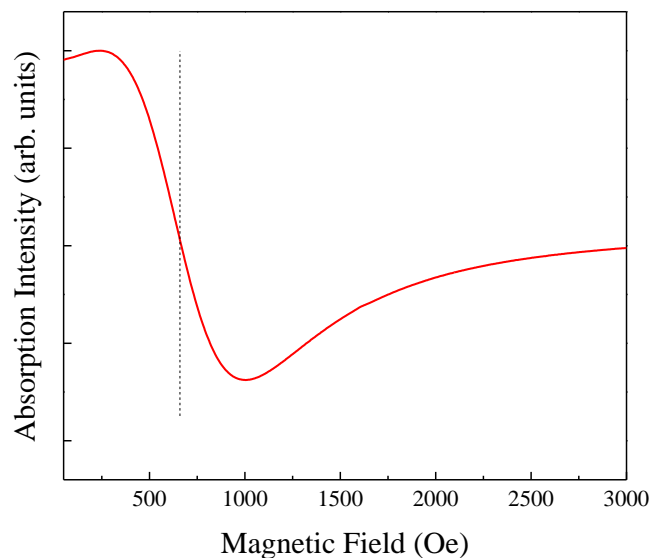


Figure 3-3. ESR spectra of a 200 nm Fe₇₅Ga₂₅/Si film with a FMR linewidth of 750 Oe.

The effect of sputtering pressure on the linewidth of 35 nm Fe₇₅Ga₂₅ films was carried out by varying the pressure from 0.4 – 3.0 mTorr. It was found that the pressure has a large effect on the FMR linewidth of the films as shown in Figure 3-4. The curve has a shape similar to a sombrero function, though lower sputtering pressures could not be explored because of plasma instability. At pressures of 1.2 and 3.0 mTorr, a large increased in FMR linewidth was observed, which may be due to the residual stress (Chapter 4) that has a direct impact on the FMR linewidth. At the lowest pressure, 0.4 mTorr, the FMR linewidth was found to be 175 Oe, lower than the literature value of 260 Oe for a 90 nm epitaxial Fe₈₁Ga₁₉ film (Butera 2005).

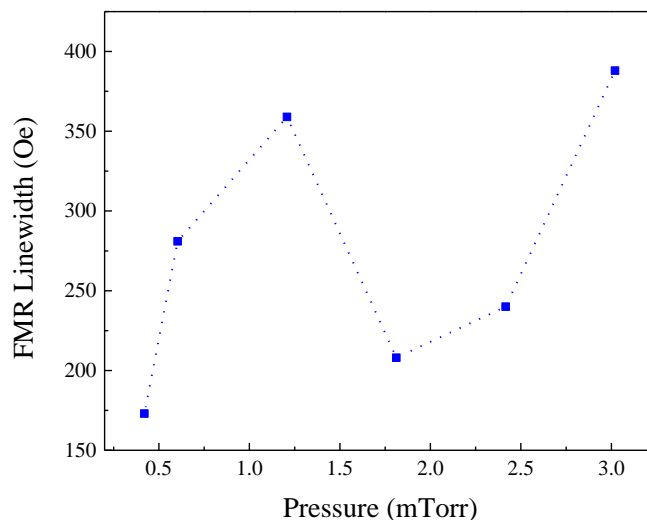


Figure 3-4. FMR linewidth as a function of sputtering pressure of argon for 35 nm Fe₇₅Ga₂₅/Si films.

The magnetoelastic behavior of FeGa was determined via longitudinal magneto-optic Kerr effect (MOKE) measurements. Using a voltage-controlled MOKE setup described in Chapter 2, magnetic hysteresis of Fe₇₅Ga₂₅ (70 nm)/Ta(20 nm)/PMN-PT [001]/Ni (20 nm) structure was measured. Magnetic field was swept from -600 to 600 Oe, while poling the PMN-PT sample to strain the Fe₇₅Ga₂₅ film, and the results can be seen in Figure 3-5.

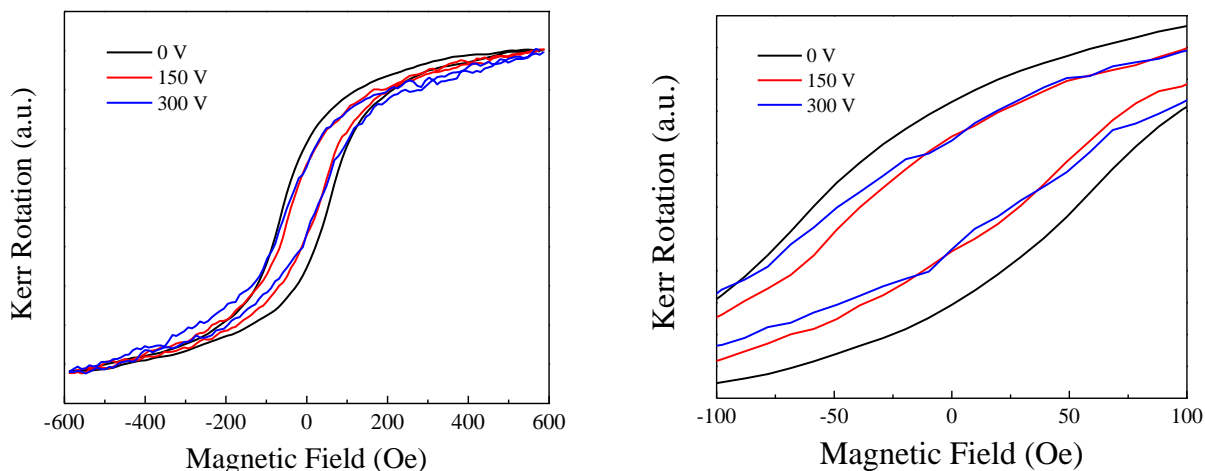


Figure 3-5 Magnetic hysteresis measured by MOKE of Fe₇₅Ga₂₅ (70 nm)/Ta (10 nm)/PMN-PT [001]/ Ni (20 nm) with applied voltages.

At 300 V applied through the PMN-PT substrate, a strain of approximately $-1000 \mu\epsilon$ was induced in the $\text{Fe}_{75}\text{Ga}_{25}$ film. This corresponded to a reduction in coercivity from 58 Oe with no strain to 37 Oe with $1100 \mu\epsilon$. Using the values for coercivity and saturation magnetization, a value for saturation magnetostriction was extracted, which was $20 \mu\epsilon$ for this 70nm $\text{Fe}_{75}\text{Ga}_{25}$ film, which is low for single-phase $\text{Fe}_{75}\text{Ga}_{25}$, normally closer to $100 \mu\epsilon$. Extracting magnetostriction from the change in coercivity does not take into consideration the change in anisotropy, and so this method underestimated the values for thin film FeGa.

To assess the effect of the Fe and Ga ratio on the magnetostriction and saturation magnetization, a slightly different composition of 85/15 was examined, as it was reported to have a high magnetostriction of up to $600 \mu\epsilon$. For $\text{Fe}_{85}\text{Ga}_{15}$ films, the volume normalized saturation magnetization was increased to 1150 emu/cc compared to 873 emu/cc of $\text{Fe}_{75}\text{Ga}_{25}$ films. The magnetostrictive properties of sputtered films are highly dependent on the residual stresses that form during deposition, and so optimization was required.

300 nm $\text{Fe}_{85}\text{Ga}_{15}$ films were grown on Pt (50 nm)/Ti (5 nm)/PMN-PT (011)/Ti (10 nm)/Au (125 nm) and hysteresis loops were measured with and without applied voltage/strain, as shown in Figure 3-6. The left plot shows the change in hysteresis with applied strain, which corresponds to a magnetostriction of $60 \mu\epsilon$, close to values reported for thicker $1.5 \mu\text{m}$ $\text{Fe}_{85}\text{Ga}_{15}$ films (Zhao 2009). The plot on the right shows the strained and unstrained hysteresis of a 300 nm $\text{Fe}_{85}\text{Ga}_{15}$ film with residual stresses 20 times higher than the left plot. Not only is the coercivity significantly higher (57 Oe compared to 30 Oe), the change in the magnetic anisotropy is significantly diminished, indicating the residual stresses have significant impact on the magnetoelastic properties.

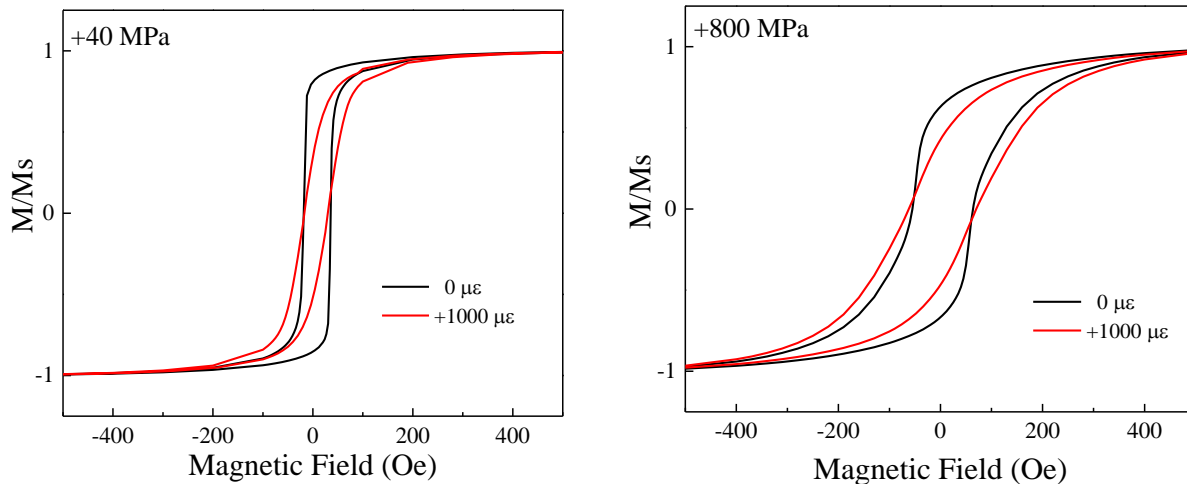


Figure 3-6. Strained and unstrained hysteresis of a 300 nm $\text{Fe}_{85}\text{Ga}_{15}$ sample with (left) a residual stress of +40 MPa and (right) a residual stress of +800 MPa.

3.2 FeGaB

3.2.1 Growth and Composition

Iron-gallium-boron (FeGaB) was synthesized via co-sputtering of a $\text{Fe}_{80}\text{Ga}_{20}$ and boron targets. While the $\text{Fe}_{80}\text{Ga}_{20}$ target was held at a constant power of 60 W, it was found that with increasing power to the boron target, the boron content increased, as expected. It was also found that as the boron content of the films increased, the ratio of Fe to Ga decreased, as shown in Table 3-1. This effect was also reported by other groups, but the cause is not known at this time (Lou 2007).

Table 3-1. Changing Fe:Ga ratio with increasing boron content

Boron Power (W)	Boron Content (at. %)	Fe:Ga Ratio
0	0	75:25
30	11	68:21
40	15	65:20
50	19	60:21

3.2.2 Magnetic Properties of FeGaB

200 nm $\text{Fe}_{65}\text{Ga}_{20}\text{B}_{15}$ films were synthesized on Si (100) substrates. Similar to $\text{Fe}_{75}\text{Ga}_{25}$, $\text{Fe}_{65}\text{Ga}_{20}\text{B}_{15}$ showed strong in-plane anisotropy and the saturation fields for in-plane and out-of-plane magnetization are 3 kOe and 15 kOe as seen in Figure 3-7. The addition of boron caused the out-of-plane saturation field to increase and the in-plane saturation field to decrease. In-plane and out-of-plane coercivities were found to be 55 Oe and 300 Oe respectively, which is expected, as boron is known to soften the properties of magnetic materials. Saturation magnetization was found to be 987 emu/cc or 12.4 kG, an increase from $\text{Fe}_{75}\text{Ga}_{25}$, contradicting prior work on this material system (Lou 2007). One possible explanation for this lies with the stresses in the $\text{Fe}_{75}\text{Ga}_{25}$ films. Boron could allow for the reduction of the residual stresses in the structure, allowing for a higher magnetization at the low fields measured.

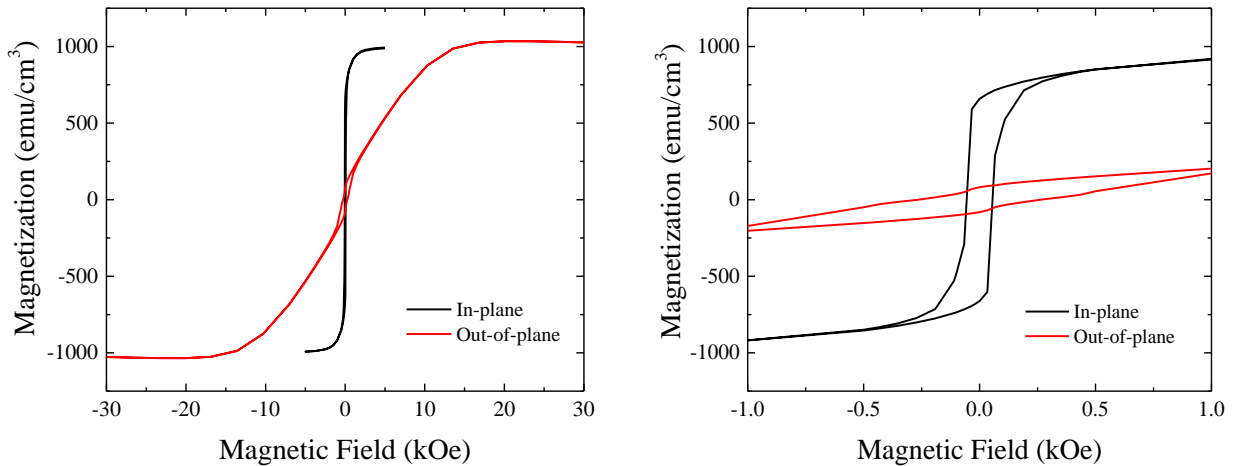


Figure 3-7. In-plane and out-of-plane magnetic hysteresis of 200 nm $\text{Fe}_{68}\text{Ga}_{26}\text{B}_{14}/\text{Si}$ (the right plot is magnified to show coercivity).

The effect of boron content and film thickness on the saturation field, coercivity and saturation magnetization of FeGaB films was assessed via SQUID magnetometry. Films with 11%, 15% and 19% boron content and thicknesses of 30, 50 and 100 nm were deposited on Si

(100) substrates, shown in Figure 3-8. For the purposes of tuning the properties via boron content, only in-plane scans were performed, as the properties need to be optimized in-plane for this specific application. Magnetic hysteresis was measured from -500 Oe to 500 Oe, as this was determined to be sufficient to saturate the FeGaB films in-plane. As boron content increases, in-plane anisotropy increases, decreasing the saturation field from 200 Oe at 11% boron to around 80 Oe at 19% – as the material becomes magnetically softer, it takes less energy to saturate it. However, the film with boron content of 15% had a larger saturation field than that of the 11% sample. Additionally, the coercivity decreased from 80 Oe at 11% boron to 16 Oe at 19% boron, which follows the trend for the saturation field.

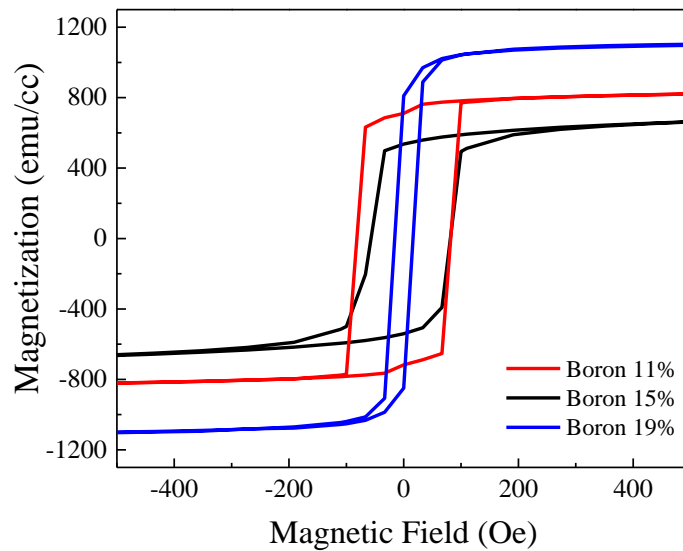


Figure 3-8. Magnetic hysteresis of 100 nm thick FeGaB films at 11%, 15%, and 19% boron content.

The effect of film thickness for $\text{Fe}_{65}\text{Ga}_{20}\text{B}_{15}$ films is shown in Figure 3-9. As film thickness decreased, coercivity was found to decrease. At 15% boron, a 100 nm film had a coercivity of 58 Oe, while a 30 nm film had a coercivity of less than 20 Oe. As the film thickness decreases, the magnetic domains in the film tend to have an in-plane orientation, so a reduction

in coercivity is expected. One important note is that at 19% boron content, 30, 50 and 100 nm films all had similar coercivities, approximately 18 Oe.

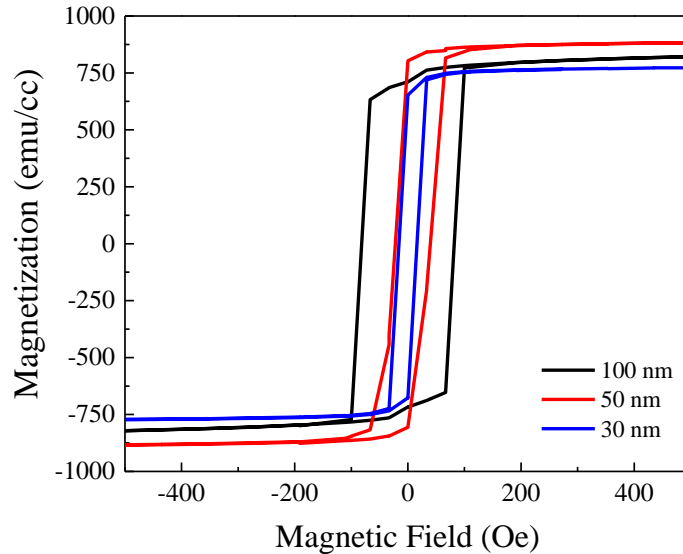


Figure 3-9. Magnetic hysteresis of $\text{Fe}_{65}\text{Ga}_{20}\text{B}_{15}$ at 30, 50, and 100 nm thicknesses.

A summary of the composition and thickness effects on magnetic hysteresis for FeGaB films is shown in Figure 3-10. The saturation magnetization was found to increase with increasing boron content and decreasing film thickness, from 640 emu/cc (8 kG) at 100 nm and 11% boron to 1460 emu/cc (18.3 kG) at 30 nm and 19% boron. In the iron-gallium system, the boron is purported to be an interstitial atom, disrupting the lattice of FeGa, reducing the size of the crystallites and therefore, the magnetic domains. Because of this, the magnetic softness of the material is enhanced, meaning that the coercivity and FMR linewidth should decrease. FeGaB films with boron concentration of 19% and 30 nm thickness have the lowest coercivity and highest magnetization of all films characterized. However, this enhancement is at the cost of the magnetocrystalline anisotropy, and therefore magnetostriction, indicating that there is an optimal value for the boron concentration (11-15% in this work).

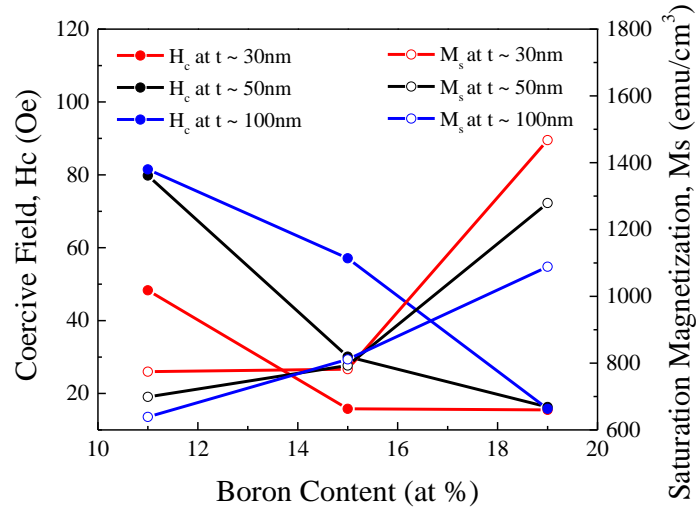


Figure 3-10. Summarized composition and thickness dependent magnetic hysteresis properties for FeGaB (B=11-19%) thin films (30-100nm).

The effect of boron content on the linewidth was assessed at 100 nm thickness, for 11%, 15% and 19% boron content as shown in Figure 3-11. As expected, the linewidth narrowed as a boron content increased, i.e., the material became magnetically softer. At 11% boron, the linewidth was determined to be 600 G, and at 19% boron content, the linewidth was determined to be 210 Oe. This value is higher than the reported value for Fe₇₀Ga₁₈B₁₂, about 20 Oe at 100 nm, though this was achieved with *in situ* magnetic field during the deposition (Lou 2007). As expected, the linewidth narrowed as a boron content increased, i.e., the material became magnetically softer. The interstitial boron disrupts the lattice of FeGa, reduces the grain size of the films, leading to reduced magnetocrystalline anisotropy, softer magnetic properties and lower loss.

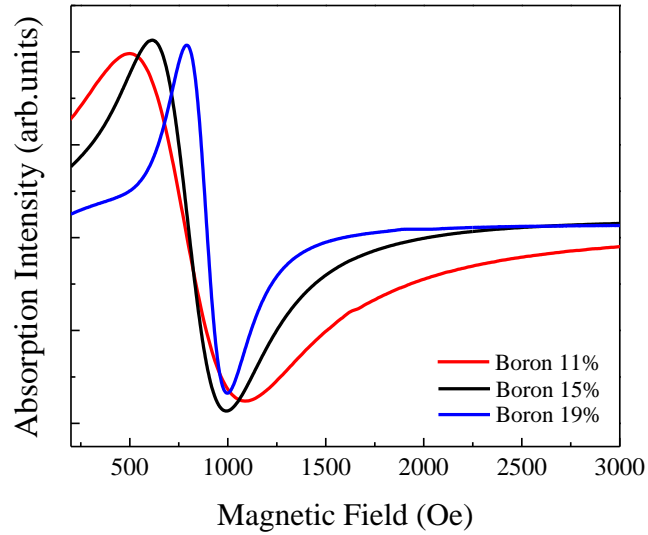


Figure 3-11. ESR spectra of 100 nm FeGaB/Si with 11%, 15% and 19% boron concentration.

The effect of film thickness on linewidth was assessed at film thickness of 30 nm, 50 nm, and 100 nm at 11%, 15% and 19% boron as shown in Figure 3-12. At 11% boron, the thickest 100 nm film had the largest linewidth of 600 Oe, and the thinnest 30 nm film had the smallest linewidth of 210 Oe. This trend of narrower linewidth with decreasing thickness applied to all boron concentrations measured. Boron doping enhances the magnetic softness as well as reduces the loss, so a large linewidth at low doping concentration is expected. For a given boron concentration, the thickest film did not have the largest linewidth as expected. For the 15% boron film, the 50 nm film had the highest FMR linewidth. With 11% and 19% boron, the thickest film had the largest FMR linewidth, justifying the usage of thinner films for the intended application.

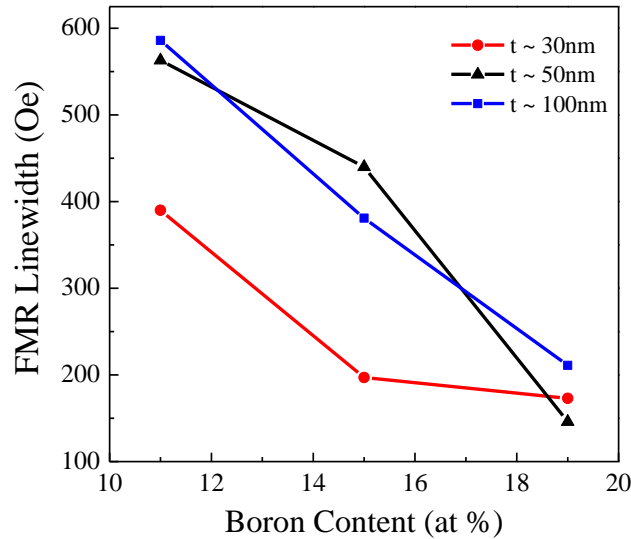


Figure 3-12. Summary of FMR linewidth data for FeGaB samples with boron doping at 11%, 15% and 19% at film thicknesses of 30, 50 and 100 nm.

The magnetoelastic behavior of a 100 nm $\text{Fe}_{65}\text{Ga}_{20}\text{B}_{15}$ sample with 15% boron content was assessed using SQUID magnetometry with *in situ* electrical poling. The sample was grown on Pt (50 nm)/Ti (5 nm)/PMN-PT (011)/Ti (10 nm)/Au (125 nm) and the magnetic hysteresis was measured with 0 V and +400 V applied. The magnetostriction was extracted by taking the difference in the area of the strained (voltage) and unstrained (no voltage) hysteresis loops. With a modulus of 70 GPa, a 100nm $\text{Fe}_{70}\text{Ga}_{18}\text{B}_{12}$ film was reported with a saturation magnetostriction of 70 $\mu\epsilon$ (Lou 2007). Assuming the same modulus, the saturation magnetostriction in this work for a 100 nm $\text{Fe}_{65}\text{Ga}_{20}\text{B}_{15}$ sample was determined to be 50 $\mu\epsilon$, comparable in magnitude to the literature result.

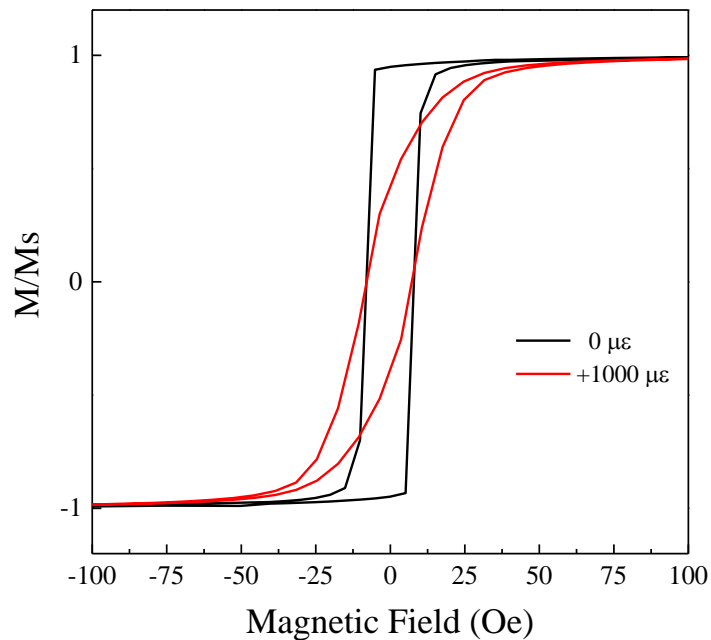


Figure 3-13. Strained and unstrained hysteresis of a 100 nm $\text{Fe}_{65}\text{Ga}_{20}\text{B}_{15}$ corresponding to a saturation magnetostriction of $50 \mu\epsilon$.

Boron doping is a useful technique for tuning the magnetic properties of FeGa, but it is difficult to ensure uniform distribution of the dopant throughout the entire film. Additionally, doping often reduces the stiffness of the material, negatively impacting its ability to propagate strain. Because the application considered requires films with thickness on the order of nanometers, the exchange interactions of magnetic materials can be exploited via sequential growth of materials with complementary magnetic properties. Whereas doping has a level of uncertainty regarding the uniformity of dopant throughout the film, layer thickness and uniformity can be easily controlled for magnetic multilayers.

Chapter 4 : Growth and Characterization of FeGa/NiFe Multilayers

In this work, the frequency-dependent magnetic properties of sputtered Fe₈₅Ga₁₅/Ni₈₁Fe₁₉ (or FeGa/NiFe) magnetic multilayers were examined to tailor their magnetic softness, loss at microwave frequencies, permeability, and magnetoelasticity, leveraging the magnetic softness and low loss of NiFe, and the high saturation magnetostriction (λ_s) and magnetization (M_s) of FeGa. A systematic change was observed as the number of bilayers or interfaces increases: a seven-bilayer structure results in an 88% reduction in coercivity and a 55% reduction in FMR linewidth at X-band compared to a single phase FeGa film, while maintaining a high relative permeability of 700. The magnetostriction was slightly reduced by the addition of NiFe but still maintained at up to 70% that of single phase FeGa. The depth-dependent composition and magnetization of these heterostructures as a function of magnetic and electric fields was assessed via polarized neutron reflectometry. The tunability of these magnetic heterostructures makes them excellent candidates for RF magnetic applications requiring strong magnetoelastic coupling and low loss.

4.1 Growth and Composition

To maintain the magnetic properties of FeGa and NiFe over time, the residual stress was used as a metric for optimizing the quality of the films. Stress can be tuned via sputtering power and pressure, and as discussed in Section 2.1.2, but a slightly tensile stress is preferred for fabrication and maintaining a high saturation magnetostriction. The trends in residual stress as a function of increasing power and pressure can be seen in Figure 4-1. As the sputtering pressure decreased, both phases exhibited a reduction in the residual stresses, which is expected due to the

increased energy per sputtered species. For similar reasons, the reduction of residual stresses with increasing sputtering power was observed.

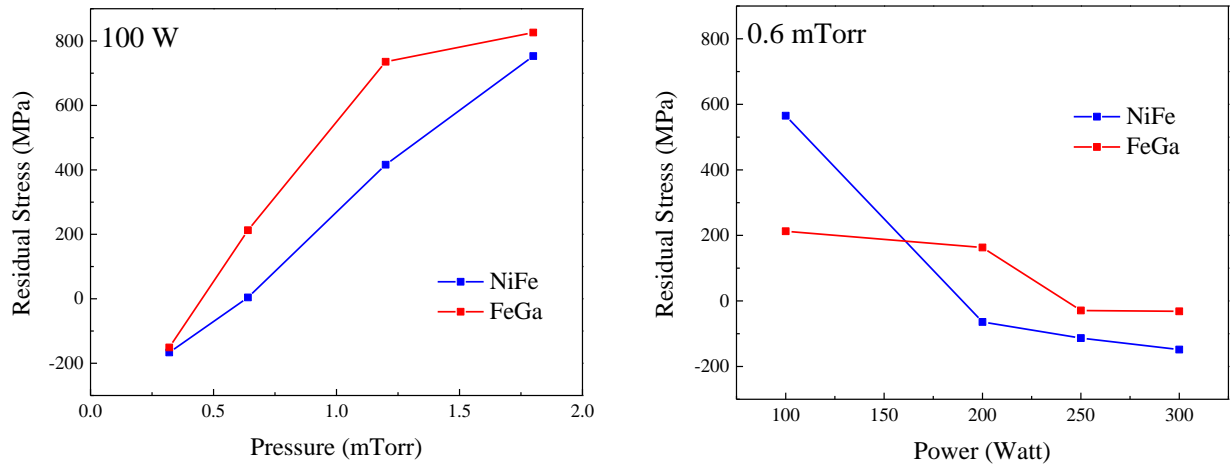


Figure 4-1. Residual stress optimization for (left) sputtering pressure and (right) power for 60 nm FeGa and NiFe films grown on Si (100).

Growth rates of FeGa and NiFe were measured via contact profilometry for all process conditions. It was found that in both cases, the growth rate was largely independent of sputtering pressures from 0.3 – 1.8 mTorr, which is often the cause for DC magnetron sputtering. Deposition rate was shown to increase at higher powers. Neither sputtering pressure nor power was shown to impact the composition of the films, which is due in part to the similar sputtering yields for the constituent elements, 1.3 for Ni and 1.5 for Fe at 600 eV. Growth rate with varying pressures and powers is summarized in Figure 4-2.

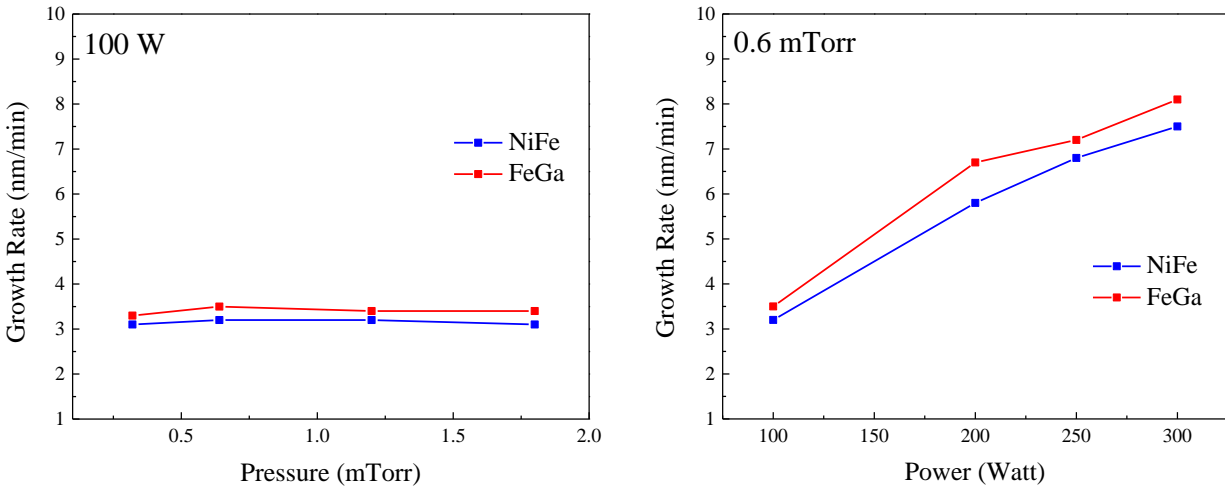


Figure 4-2. Growth rates for FeGa and NiFe as a function of (left) sputtering pressure and (right) power.

XPS depth profiling indicated that FeGa and NiFe layers have a minimal local mixing, likely due to the relatively low sputtering power and the fact that the films were deposited at room temperature. However, the Ga 2p peak can still be observed after 850 s etch time, indicating that there may be some local intermixing due to the ion sputtering process in XPS (4 KeV). A 3 BL sample with the structure (20 nm FeGa/15 nm NiFe)₃/20 nm FeGa and a total thickness of 130 nm was measured after 50 second intervals of Ar⁺ milling at 4 kV, and the resulting spectra can be seen in Figure 4-3.

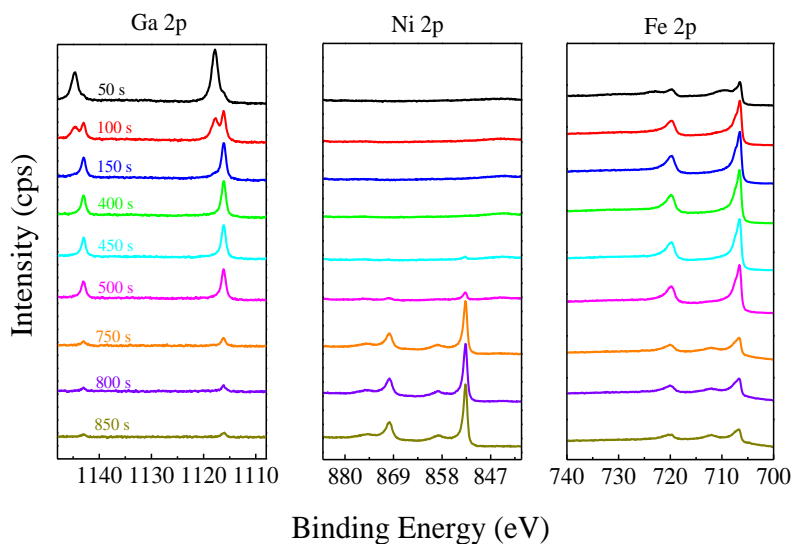


Figure 4-3. XPS spectra for 3 BL FeGa/NiFe sample with increasing etch time, showing the appearance of the Ni 2p peak and attenuation of the Ga 2p peak.

At $t=100$ s, the Ga 2p peak began to attenuate as expected with removal of the native oxide, and was completely removed by 150 s etch time. Similarly for Fe 2p, the oxide layer was removed by 100 s resulting in a nominal Fe/Ga ratio of 85/15 (at. %). The Ni 2p peak began to appear after 500 s etch time, the FeGa layer thickness was reduced to less than 10 nm, the penetration depth of XPS. The appearance of the satellite peak at 859 eV can be attributed to the creation of a 3d hole that is localized on the core hole, creating a two hole state that is approximately 6 eV lower than the Ni 2p 3/2 peak (Hufner 1975). The Fe 2p spectra shows the appearance of a small satellite peak at 750 s etch time at 712 eV. The peak spacing indicates that the peak at 720.1 eV and 713 eV are Fe 2p 3/2 and 1/2, respectively. The peak at 712.1 eV can be attributed to an Auger peak from Ni 2p, as it only appeared when the Ni 2p peak appears. Since the depositions occurred at room temperature, little intermixing between the individual layers was expected.

Film structure was characterized via x-ray diffraction for the 1-7 BL samples as shown in Figure 4-4. The prominent peak at 44° corresponds to the FeGa (110) as well as the NiFe (111)

orientations. Several oxide peaks were identified, specifically those for NiFe_2O_4 , indicating slight oxidation of the NiFe films due to ambient exposure.

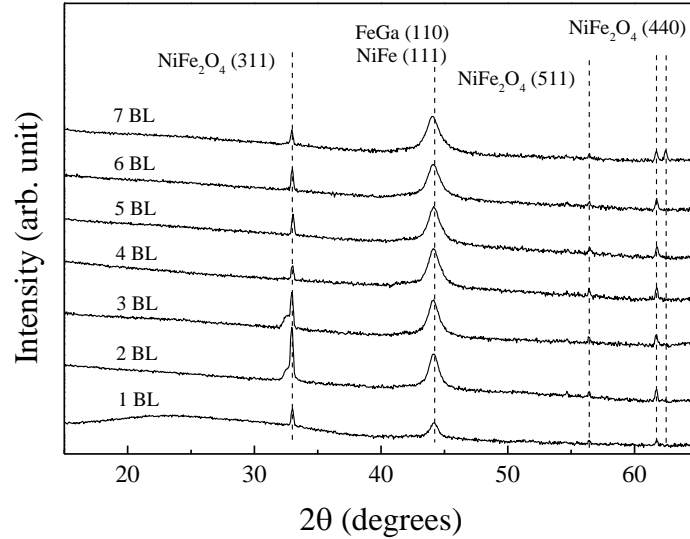


Figure 4-4. X-ray diffraction data for the 1 – 7 BL FeGa/NiFe samples with major peaks for FeGa and NiFe identified.

Grain size of the FeGa (110) and NiFe (111) phases was extracted using the FWHM of the peaks and the Scherrer equation described in Chapter 2 and the results are summarized in Figure 4-5. With the exception of the 2 BL sample, grain size decreases linearly as the thickness of the individual layers decreases. For the 7 BL sample that had the thinnest layers, the grain size was only slightly larger than the layer thickness, indicating the impact of the geometry on the structure.

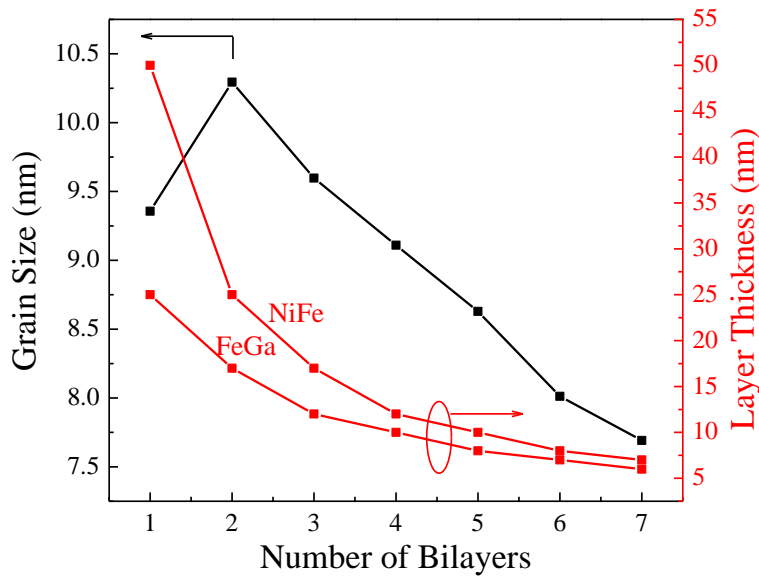


Figure 4-5. Grain size (left axis) of the major FeGa (110) and NiFe (111) peaks and layer thickness (right axis) as a function of the number of bilayers in 100 nm samples.

4.2 Magnetic Properties of FeGa and NiFe Multilayers

Static magnetic properties were assessed using both SQUID magnetometry and VSM, which were discussed in Sections 2.3.2 and 2.3.3. Figure 4-6 shows the static magnetic properties of FeGa and NiFe as well as a 5 BL structure to illustrate their complementary magnetic properties. Single-phase FeGa was shown to have a saturation magnetization of 1150 emu/cc and a coercivity of 60 Oe, and NiFe was shown to have a saturation magnetization of 780 emu/cc and a coercivity of less than 1 Oe, both of which agree well with values reported in literature for sputtered films (Ueno 1995). Additionally, the NiFe shows strong in-plane uniaxial anisotropy. For all of the bilayer samples, the saturation magnetization was found to be around 1050 emu/cc, higher than that predicted by the rule of mixtures based on the 1:1 ratio of FeGa:NiFe, indicating that the layers are exchange-coupled. This effect is similar to that seen in exchange spring systems, where the resulting composite maintains the high magnetization of the

soft phase and the high coercivity of the hard phase (Fullerton 1999). However, studies of magnetic composites where the individual phases have similar coercivity and saturation magnetization are limited.

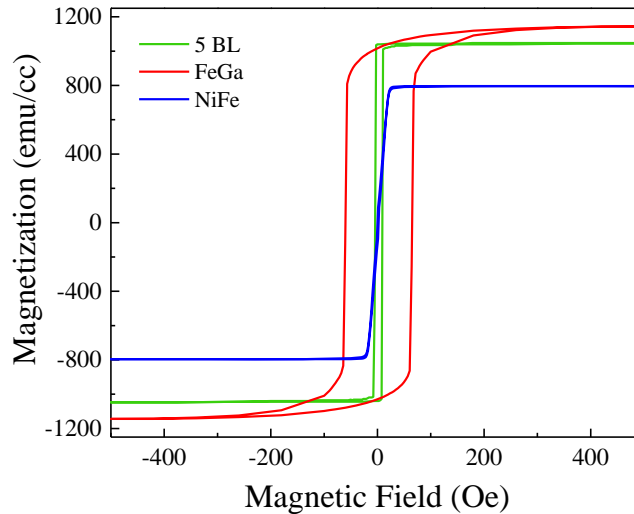


Figure 4-6. Hysteresis loops of single phase FeGa, NiFe and a 5 BL sample with the structure (8.5 nm FeGa/10 nm NiFe)₅/8.5 nm FeGa.

FMR linewidth of these samples were assessed using ESR spectroscopy, which measures the linewidth at X band (9.6 GHz). The FMR linewidth of single-phase Fe₈₅Ga₁₅ was found to be 260 Oe, while that of single-phase Ni₈₁Fe₁₉ was 30 Oe. A 100 nm 5 BL sample had an FMR linewidth was 35 Oe, which is smaller than expected given that the film contains equal thicknesses of FeGa and NiFe, indicating exchange-coupling of the low-loss NiFe layers. Figure 4-7 shows the single phase spectra with that of the 5 BL sample.

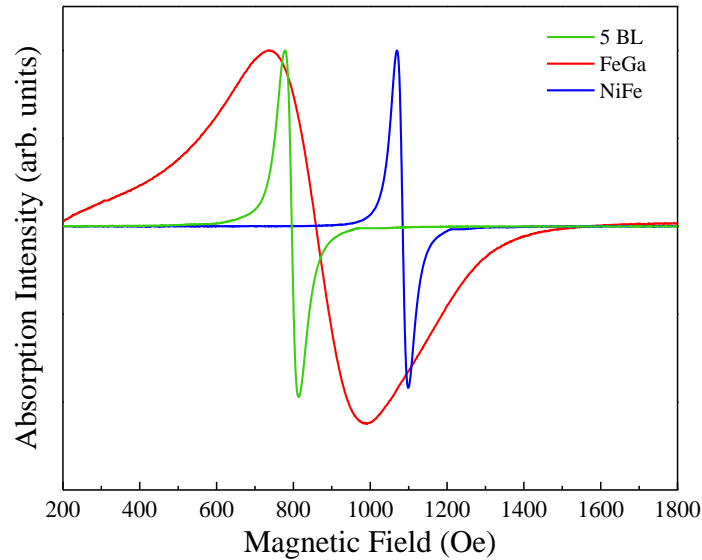


Figure 4-7. ESR spectra of single phase FeGa, NiFe and a 5 BL sample with the structure $(8.5 \text{ nm FeGa}/10 \text{ nm NiFe})_5/8.5 \text{ nm FeGa}$.

The coercivity and FMR linewidth at 9.6 GHz are shown in Figure 4-8 as a function of the number of bilayers, while maintaining a total thickness of 100 nm and a 1:1 volume ratio of FeGa:NiFe. The coercivity decreased with decreasing layer thickness, in an almost linear fashion, which can be attributed to the decrease in magnetic anisotropy dispersion. As the layers decrease in thickness, the distribution of the possible orientations of the magnetic domains narrows, with the majority lying in plane. This reduces the energy required to rotate the magnetization in plane. It also reduces the average crystallite size, which reduces the overall magnetocrystalline anisotropy, enhancing the soft magnetic properties of these films. The FMR linewidth shows similar behavior, decreasing linearly until 7 bilayer (7 BL), where the FMR linewidth increases dramatically. The broadening of the FMR linewidth in the 7 BL sample (6 nm FeGa/7 nm NiFe) can be attributed to the enhanced coupling of the FeGa layers due to layer thickness being much closer to the exchange length. The 5 BL sample shows a very narrow FMR linewidth of around 35 Oe, close to the value for single-phase NiFe, which is 30 Oe. Both

coercivity and FMR linewidth show a similar trend, indicating that the 5 BL sample is the optimal configuration in this study.

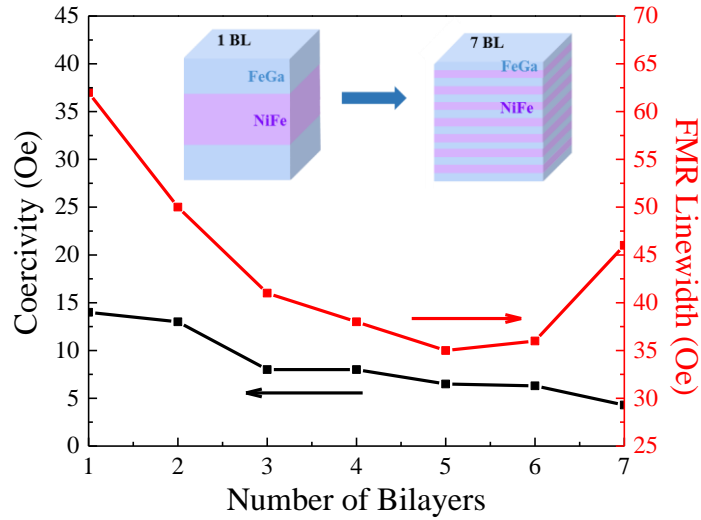


Figure 4-8. Coercivity and FMR linewidth at X band as a function increasing number of bilayers (decreasing layer thickness).

Broadband FMR measurements were performed on a 5 BL sample, and the biasing magnetic field was varied from 50–400 Oe. The real and imaginary components of the permeability were extracted via conformal mapping (Liu 2005), the results of which are shown in Figure 3. The sample shows prominent real and imaginary components of the permeability, indicating that the conductive losses of the film were not significant.

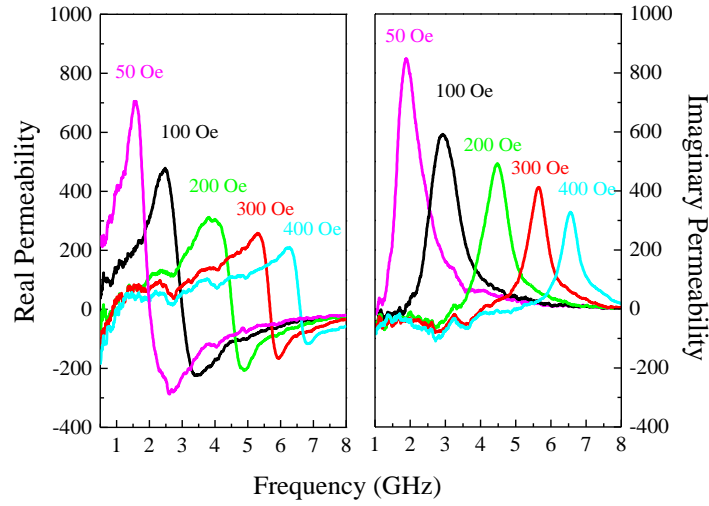


Figure 4-9. Extracted (left) real and (right) imaginary permeability for a 5 BL sample (8.5 nm FeGa/10 nm NiFe)₅/8.5 nm FeGa multilayer with increasing magnetic bias.

The 5 BL sample showed the highest permeability of 700 at a small magnetic field of 50 Oe. As the applied magnetic field increases, the curves shift to higher frequency, from a f_{FMR} of 1.9 GHz at 50 Oe bias up to 6.6 GHz at 400 Oe, which is in agreement with Kittel's equation.

$$f_{FMR} = \gamma \sqrt{(H_k + \mathbf{H}_{dc} + \Delta H_{eff})(4\pi M_s + H_k + \mathbf{H}_{dc} + \Delta H_{eff})} \quad (4.1)$$

These multilayers demonstrated strong sensitivity to magnetic fields as well low loss for a conducting film, but in order for them to be integrated into a strain-coupled multiferroic device, the magnetoelastic properties needed to be assessed. Magnetostriction was extracted from the M-H loops by integrating the area of the magnetic hysteresis loops with and without applied strain. The difference in the area represents the stored magnetoelastic energy (B_{11}), and from this the magnetostriction can be extracted (O'Handley 2000). Figure 4-10 shows the saturation magnetostriction and the saturation field as a function of the number of bilayers. The 7 BL sample, corresponding to FeGa layer thickness of 6 nm, has the highest saturation magnetostriction of all samples measured, up to 40 $\mu\epsilon$, which is 67% that of single-phase FeGa.

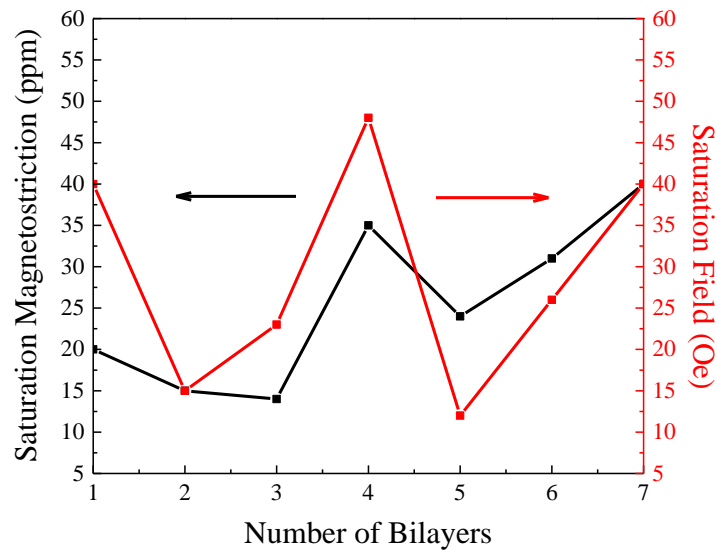


Figure 4-10. Saturation magnetostriction (left axis) and saturating field (right axis) as a function of number of FeGa/NiFe bilayers (decreasing layer thickness).

The 3 BL sample showed the smallest strain response of the samples measured, corresponding to a saturation magnetostriction of 15 $\mu\epsilon$. Values of saturation magnetostriction for 1 - 7 BL samples ranged from 15 - 40 $\mu\epsilon$. The grain size for the 4 BL sample estimated from the XRD is 9.5 nm, where the FeGa layer thickness is 10 nm. This leads to an enhanced shape anisotropy, where the grains rotate more coherently with applied in-plane strain compared to the samples with thicker layers, resulting in a larger saturation magnetostriction as well as a higher saturation field. The enhancement at 7 BL is likely caused by the thinner layers being able to couple more effectively because they are approaching the exchange length of FeGa. This would also explain the larger saturation field, as the FeGa layers with higher coercivity can couple together more effectively. While the saturation magnetostriction is an important figure of merit for strain-coupled composites, the saturation field must also be considered, especially for applications where high sensitivity of the strain response is required. The trend of the saturation field is similar to that of saturation magnetostriction, with maxima at 1, 4 and 7 BL. One possible explanation for this is that these films have a broader distribution of domain sizes compared to

others, which would be evidenced by a higher coercivity. Figure 4-8 shows that this is indeed the case for the 7 BL sample, but not the 4 BL sample, and so further studies are needed to corroborate this. The sensitivity of the strain response can be approximated by determining the ratio of saturation magnetostriction to saturation field. The ratio for the 5 BL sample is 2, the highest of all samples measured, indicating high strain sensitivity to applied magnetic fields.

The magnetoelastic properties of these multilayers was also assessed using ESR spectroscopy to determine if the coupling was strong with a high frequency excitation. Samples were deposited on Pt (50 nm)/Ti (5 nm)/PMN-PT (011)/Ti (10 nm)/Au (125 nm) substrates that were pre-poled before FeGa/NiFe thin film deposition to ensure a linear strain response. The tunability of the FMR linewidth and resonant fields were probed by applying *in situ* voltages ranging from 50 – 600 V, which can be converted to an electric field by dividing by the substrate thickness (500 μm). There was no change observed in the FMR linewidth and resonant field after 0.3 MV/m. The results for the sample with structure (11 nm FeGa/11 nm NiFe)₃/11 nm FeGa can be seen in Figure 4-11. The FMR linewidth was found to decrease with increasing strain in the direction of the magnetic field. This result was not expected due to the fact that FeGa has a positive magnetostriction, which means that it increases in size along the axis of the applied magnetic field. An applied strain should make it magnetically harder and cause the FMR linewidth to broaden, indicating that further experiments were needed.

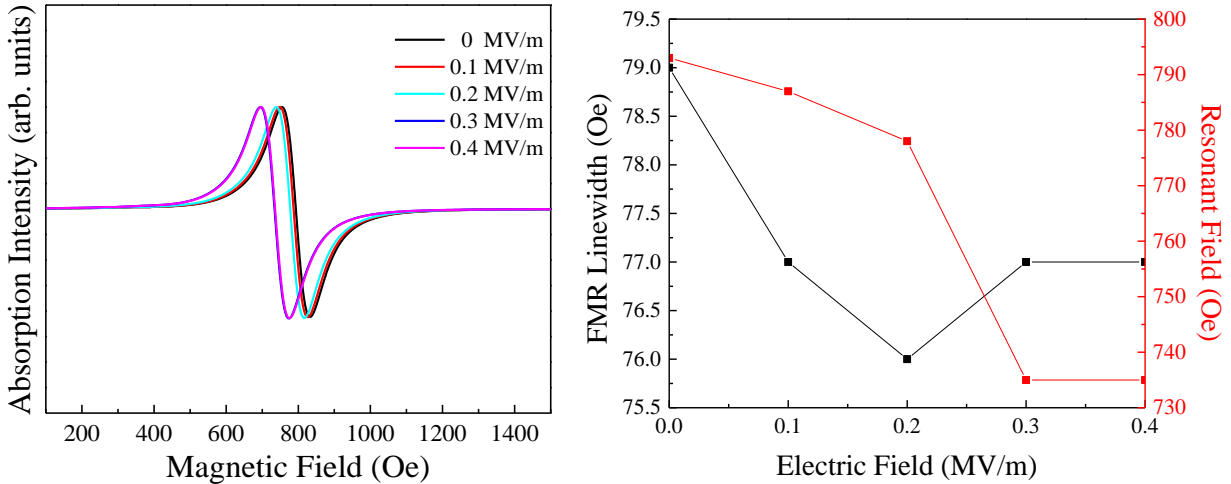


Figure 4-11. (Left) ESR spectra for a 3 BL sample and (right) FMR linewidth and resonant field as a function of electric field.

This experiment was repeated for a 2 BL sample with the structure (11 nm FeGa/11 nm NiFe)₂/11 nm FeGa, and the results can be seen in Figure 4-12. Voltages from 50-700 V were applied through the thickness of the sample, but no further shift in FMR frequency was observed after 400 V, corresponding to an electric field of 0.8 MV/m. As the electric field increased, the resonant field decreased and the FMR linewidth increased, which both indicate a hardening of the magnetic material. For the 2 BL and 3 BL samples, the layers are excited together and behave as a single magnetic material, which is promising for device integration. However, these experiments are not able to elucidate the coupling mechanism between the individual layers. Polarized neutron reflectometry was pursued to explore the depth-dependent magnetization of the FeGa/NiFe multilayers.

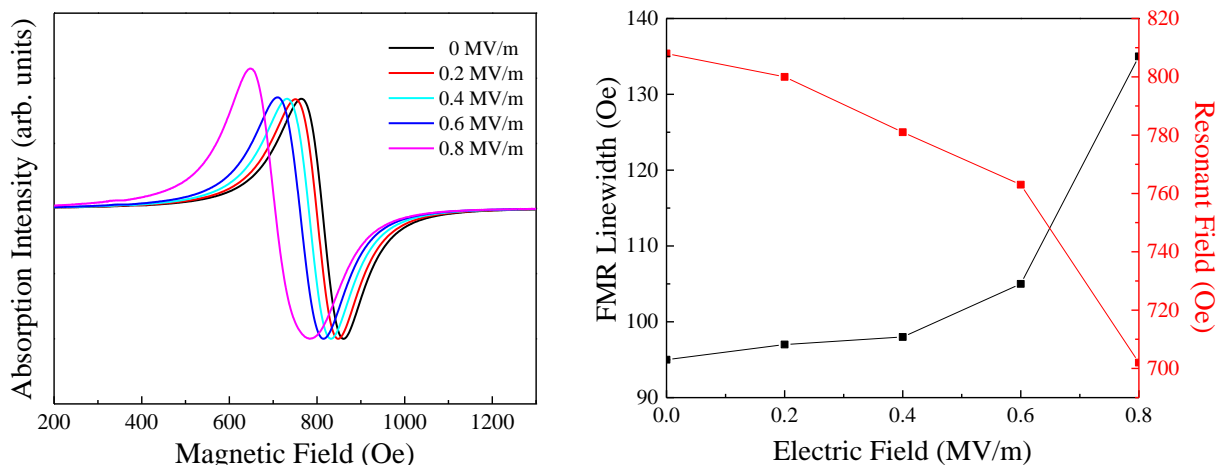


Figure 4-12. (Left) ESR spectra of 2 BL sample and (right) FMR linewidth and resonant field as a function of electric field.

4.3 Interfacial Magnetism of FeGa and NiFe Multilayers

Macroscopic magnetization techniques indicated that the magnetization of the individual FeGa/NiFe layers rotate together with applied strain and field. By varying the distance between the individual layers while holding the number of interfaces constant, the extent of the exchange coupling between each layer could be assessed by high resolution magnetometry. Three samples with different FeGa:NiFe volume ratios were selected, but all were in a 3 BL configuration (7 total layers). A sample with the structure (13 nm FeGa/17 nm NiFe)₃/13 nm FeGa/Si was measured using SQUID magnetometry and ESR spectroscopy and the results are shown in Figure 4-13. The in-plane hysteresis loops have behavior characteristic of exchange-coupled systems, where the loop can be thought of as two loops superimposed. The inset highlights this phenomena: there are two distinct saturation regions for the loop, characteristic for magnetic bilayer samples where the layers are not fully coupled (Stenning 2015). ESR spectroscopy indicated that indeed the layers were behaving as one under high frequency excitation, but the field at which the film began to absorb the incident EM energy was well past the saturation field.

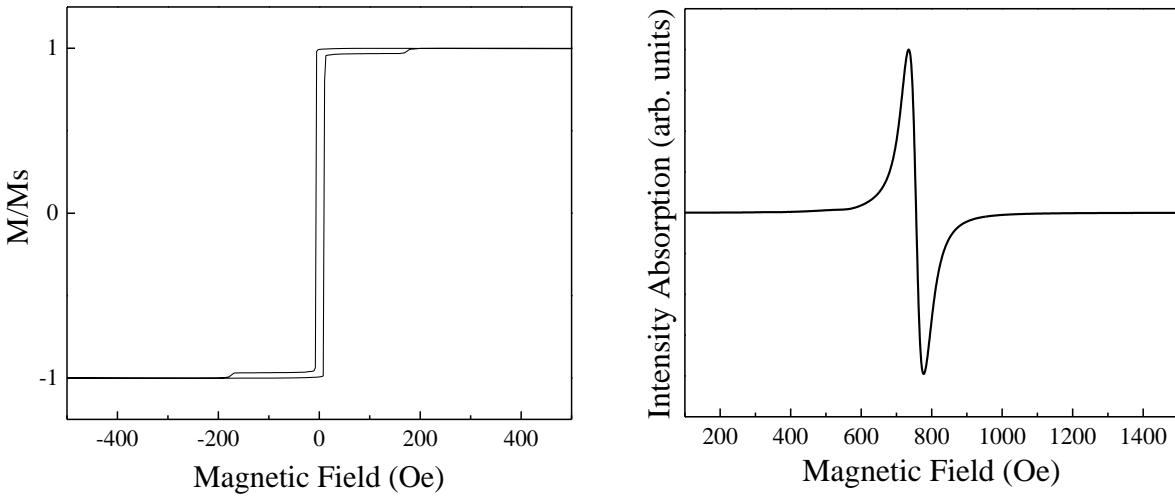


Figure 4-13. (Left) In-plane magnetization and (right) ESR spectra for a 3 BL sample with 1:1 FeGa:NiFe ratio.

A sample with the same total thickness and layer configuration, but with 4:1 FeGa:NiFe ratio with the structure (20 nm FeGa/6.7 nm NiFe)₃/20 nm FeGa/Si was grown and measured in the same way. It should be noted that thickness of the NiFe layer is close to its exchange length, around 6 nm, which could allow for more effective coupling between the FeGa layers (Abo 2013). The in-plane hysteresis loop shown in the left panel of Figure 4-14 showed similar behavior to the sample with 1:1 FeGa:NiFe volume ratio, but required almost twice the saturation field to fully rotate the magnetization. The coercivity increased from 8 Oe to 27 Oe, indicating a hardening of the in-plane easy axis as well. ESR spectroscopy confirmed that the layers exhibited a cohesive FMR linewidth, which increased from 41 Oe to 95 Oe due to the reduction in the amount of NiFe in composite.

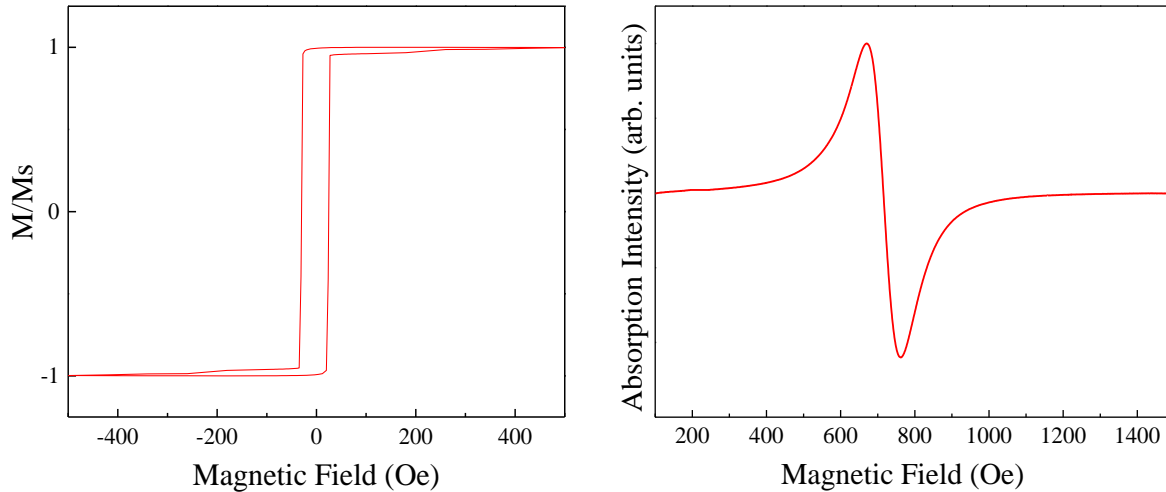


Figure 4-14. (Left) In-plane magnetization and (right) ESR spectra for a 3 BL sample with 4:1 FeGa:NiFe ratio.

A sample grown had a FeGa:NiFe ratio of 9:1 corresponding to a structure of $(22.5 \text{ FeGa} / 3.3 \text{ nm NiFe})_3 / 22.5 \text{ nm FeGa/Si}$. Magnetometry measurements shown in the left panel of Figure 4-15 indicate different behavior compared to the samples with 1:1 and 4:1 ratio, specifically, the loop closed fully and saturated at around 100 Oe, the lowest saturation field of the three samples examined. This indicates that the FeGa layers are coupled, but the very thin NiFe layers are still softening the material, as indicated by the 50% reduction in the coercivity compared to a 100 nm thick film of FeGa. However, the linewidth measured from ESR spectroscopy is almost exactly the same as single phase FeGa, indicated that the thin layers and/or volume fraction of NiFe is not enough to reduce the linewidth.

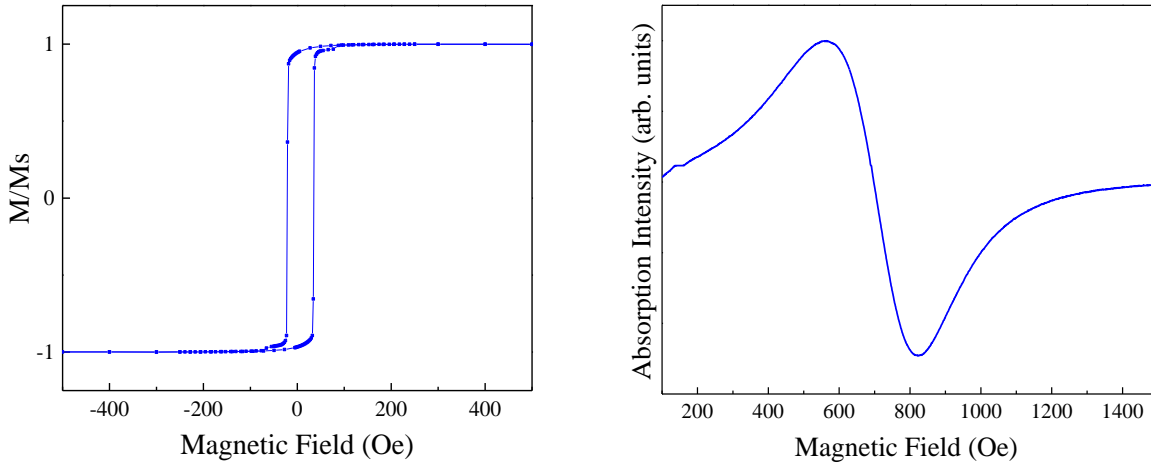


Figure 4-15. (Left) In-plane magnetization and (right) ESR spectra for a 3 BL sample with 9:1 FeGa:NiFe ratio.

From these results, there is clearly some impact of the proximity of one layer to another that affects the magnetic properties, both static and dynamic. In order to probe the exchange-coupling, polarized neutron studies were carried out to observe the depth-dependent magnetization of the films with applied magnetic field, as well as strain via a piezoelectric PMN-PT (011).

4.3.1 Magnetization Rotation of FeGa and NiFe Multilayers with Applied Magnetic Field

In order to probe the impact of layer thickness on the interlayer coupling, two samples, 1 $BL_{(PNR)}$ and 8 $BL_{(PNR)}$ were characterized by polarized neutron reflectometry. Using the PBR beamline at the NIST Center for Neutron Research, the magnetization of the samples was measured as a function of depth at both 10 Oe and 1000 Oe at 295 K. The incident and scattered neutrons were spin polarized (>97 % efficiency) to determine the parallel and perpendicular magnetization components of the multilayers. The non-spin flip components (R_{++} and R_{--}) determine the in-plane (parallel) magnetization ($\rho_{magnetic}$) and nuclear ($\rho_{nuclear}$) scattering length density (SLD) at each field. The spin flip data (R_{+-} and R_{-+}) measures the out of plane

magnetization vector. Two orientations with respect to the magnetic field were measured as seen in Figure 4-16, with one along the short axis and the other along the long axis of the rectangular sample. These two orientations are perpendicular to each other, to help assess if any anisotropy exists from the growth processes.

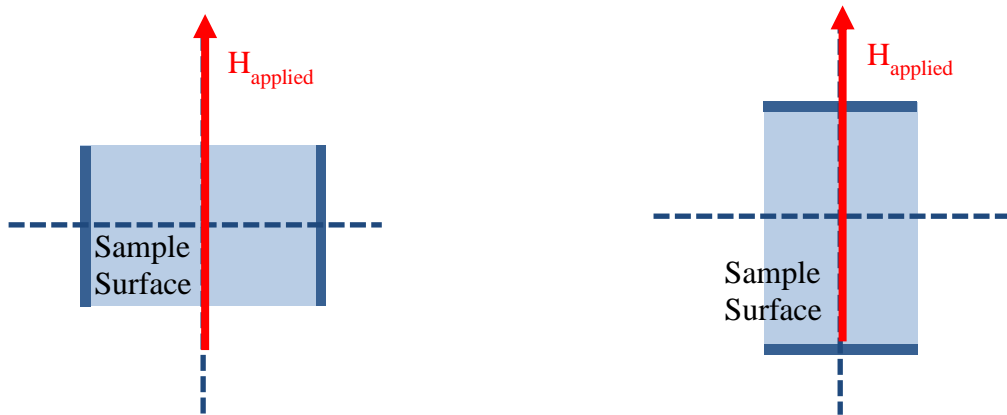


Figure 4-16. In-plane sample orientations measured for 1 $B_{(PNR)}$ and 8 $BL_{(PNR)}$.

A 1 $BL_{(PNR)}$ sample with the structure (25 nm FeGa/50 nm NiFe)₁/25 nm FeGa/Si, the thickest individual layers measured in both in plane directions with respect to the sample edge, was measured with a saturating field of 1000 Oe. The fits match the measured reflectivity well, though at higher Q values there is more uncertainty, particularly in the first sample orientation, potentially due to smaller domains and the increased likelihood of scattering.

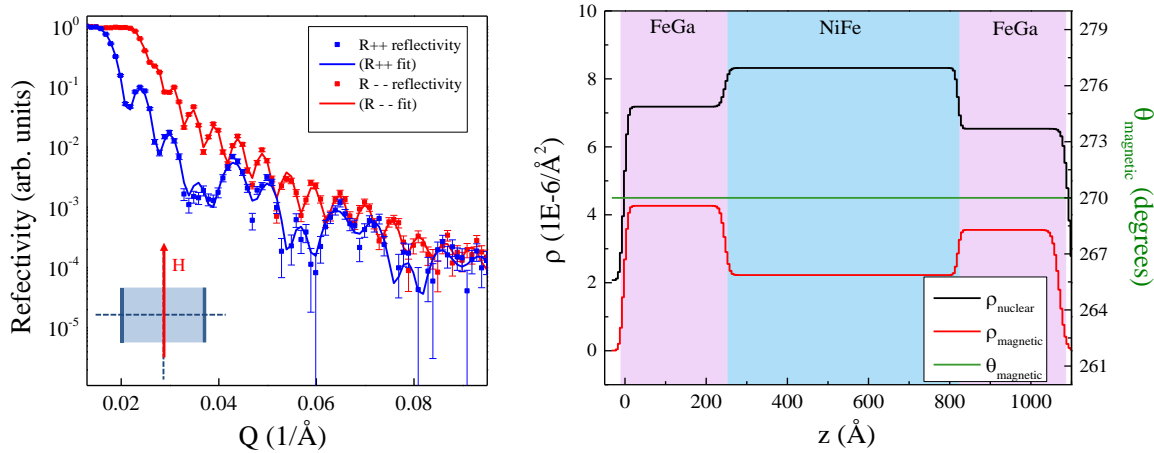


Figure 4-17. (Left) Fitted reflectivity and (right) ρ_{magnetic} and ρ_{nuclear} profiles for a 1 BL_(PNR) sample with a 1000 Oe magnetic field applied in plane.

When the 1 BL_(PNR) sample was rotated 90° so that the magnetic field is now along the long axis of the sample, the fits also match the physical model well. For both cases, there is a change in the magnetic and nuclear scattering length densities of the FeGa in the top layer of the sample. The FeGa at the interface with Si is completely clamped, and so it cannot strain significantly when a saturating field is applied compared to the top layer, which explains the decrease in ρ_{nuclear} . In poled magnetometry measurements, a slight decrease in the saturation magnetization was observed with applied strain, which would explain the decrease in ρ_{magnetic} , as they scale together.

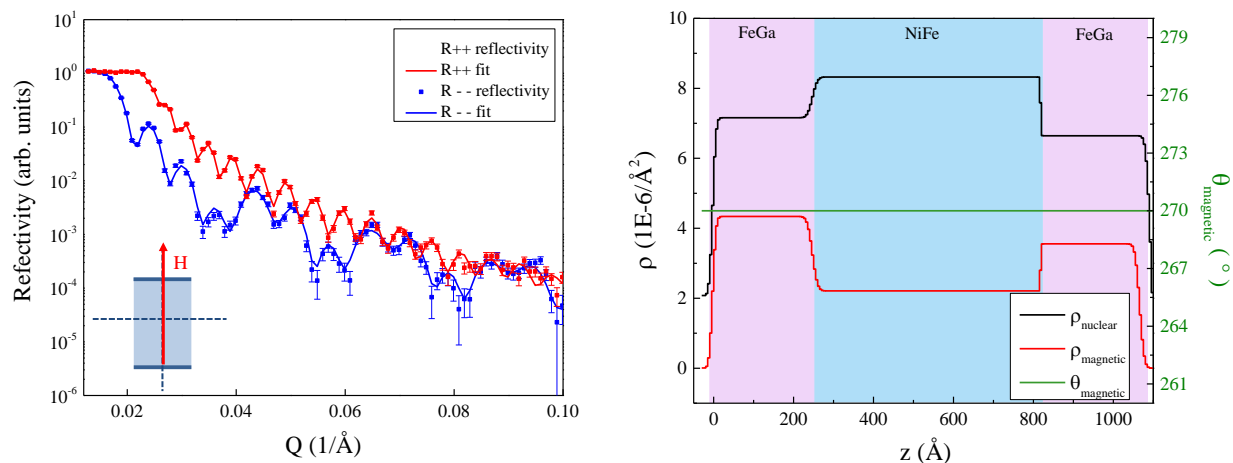


Figure 4-18. (Left) Fitted reflectivity and (right) ρ_{magnetic} and ρ_{nuclear} profiles for a 1 BL_{PNR} sample rotated 90° with respect to the applied field of 1000 Oe in plane.

Magneto-optic imaging film (MOIF) was used to determine the in-plane domain size of the 1 BL_(PNR) sample for both in-plane directions. Magnetic coercivity was determined by the field at which domains began to propagate in the film. Figure 4-19 shows the measured domain sizes, which vary between the two in-plane directions. Specifically, the original orientation showed domain sizes on the order of 10 μm while the rotated sample showed much larger domains, on the order of 100 μm . This indicates that the rotated position is an easier axis compared to the original position. One possible explanation is that the favorable axis is formed from the setup of the deposition chamber, potentially influenced by the strong permanent magnet that is behind the cathode to trap electrons near the surface of the target and promote ionization. This is unlikely, however, because the substrate is more than 6 inches from the target and constantly rotating. Another possibility lies in the anisotropy of the NiFe, in which the domains were observed to rotate 16-20° with respect to the applied field.

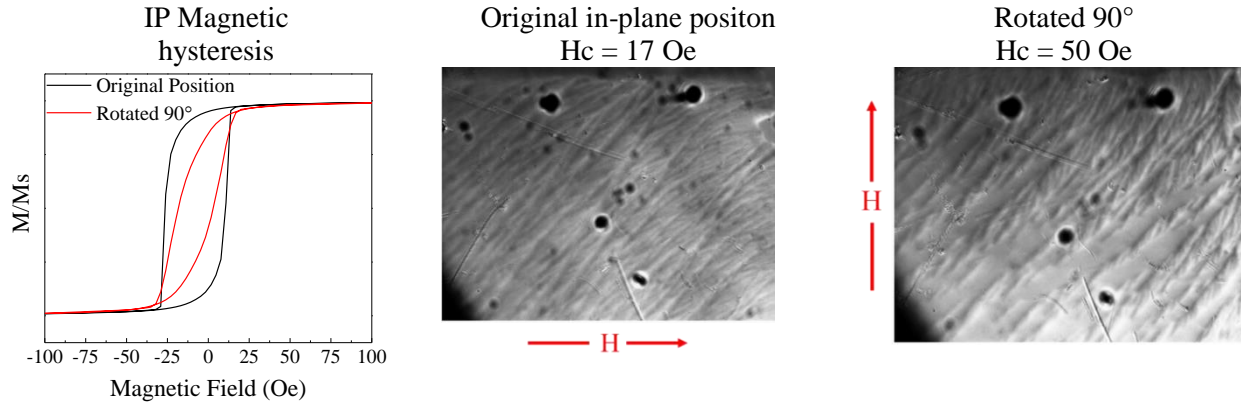


Figure 4-19. (Left) In-plane magnetic hystereses for 1 BL_(PNR) sample showing in-plane anisotropy (center) domain size in 1 BL_(PNR) sample in original orientation on the order of 10s of μm and (right) domain size of the sample rotated 90° on the order of 100s of μm , indicating in-plane anisotropy.

The 100 nm 8 BL_(PNR) sample with a structure of (6.2 nm FeGa/7.1 nm NiFe)₈/6.2 nm FeGa/Si was measured with polarized neutron reflectometry under a saturating field of 1000 Oe. Figure 4-20 shows the fitted reflectivity data for one in-plane direction as well as the scattering length density profile. At a Q value greater than 0.07, the noise increased significantly, however, the physical model captures the oscillations of the reflectivity data. The ρ_{nuclear} and ρ_{magnetic} did not vary except at the top layer of FeGa, where some oxidation is expected.

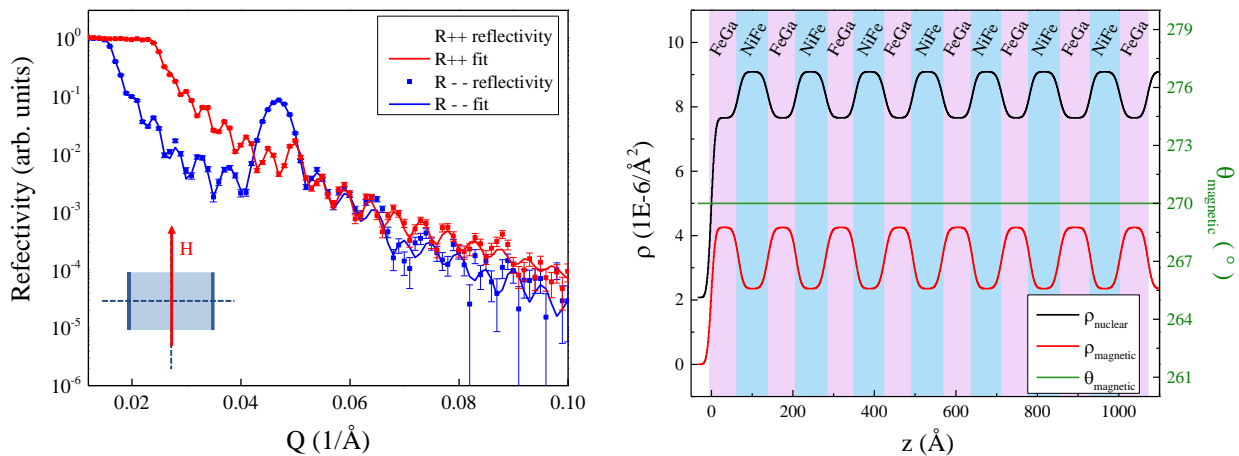


Figure 4-20. (Left) Fitted reflectivity (right) and ρ_{magnetic} and ρ_{nuclear} profiles for an 8 BL_(PNR) sample with a 1000 Oe magnetic field applied in plane.

The physical models fit well for both cases, which indicate coherent rotation of the layers. The ρ_{nuclear} and ρ_{magnetic} profiles both indicate a decrease in the nuclear SLD as well as the magnetic SLD at the FeGa/air interface, which could indicate that a large portion of the top layer has oxidized.

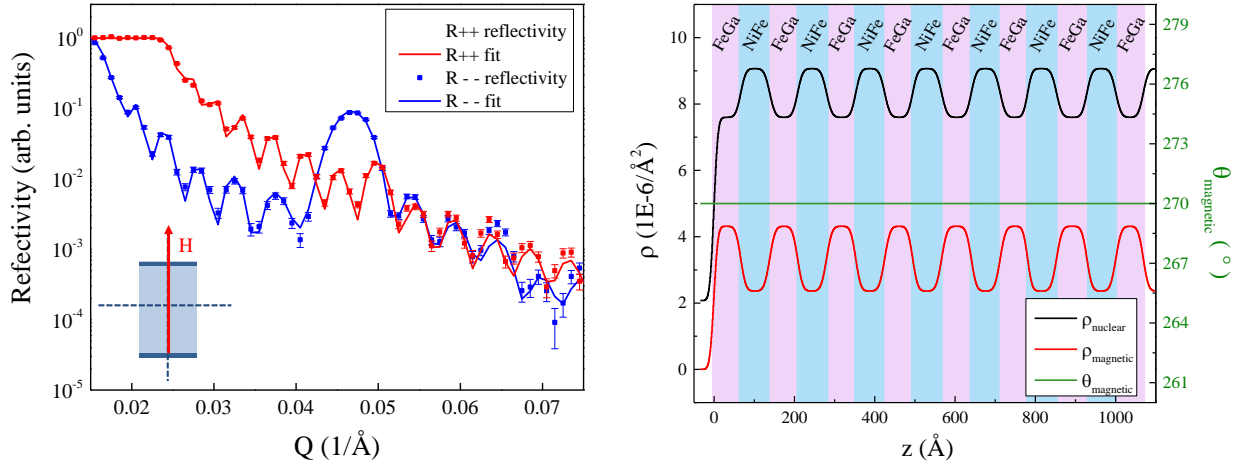


Figure 4-21. (Left) Fitted reflectivity (right) and ρ_{magnetic} and ρ_{nuclear} profiles for an 8 BL_(PNR) sample rotated 90° with respect to the applied field of 1000 Oe in plane.

MOIF was used to observe the domain formation and size in this 8 BL_(PNR) sample. Figure 4-22 shows the results for two in-plane directions, which indicate domain sizes on the order of 200 μm with similar values for magnetic coercivity. This result supports the hypothesis that the samples with the thinnest layers have larger and more uniform domain sizes, i.e., a narrow magnetic anisotropy dispersion. When the layers are thinner, it restricts the formation of domains in the out-of-plane direction and causes the two in-plane domains to be larger. No difference in coercivity between the in plane directions was observed, which indicates either that the thinner layers allow for a more uniform in plane domain size, or the anisotropy of NiFe is thickness-dependent.

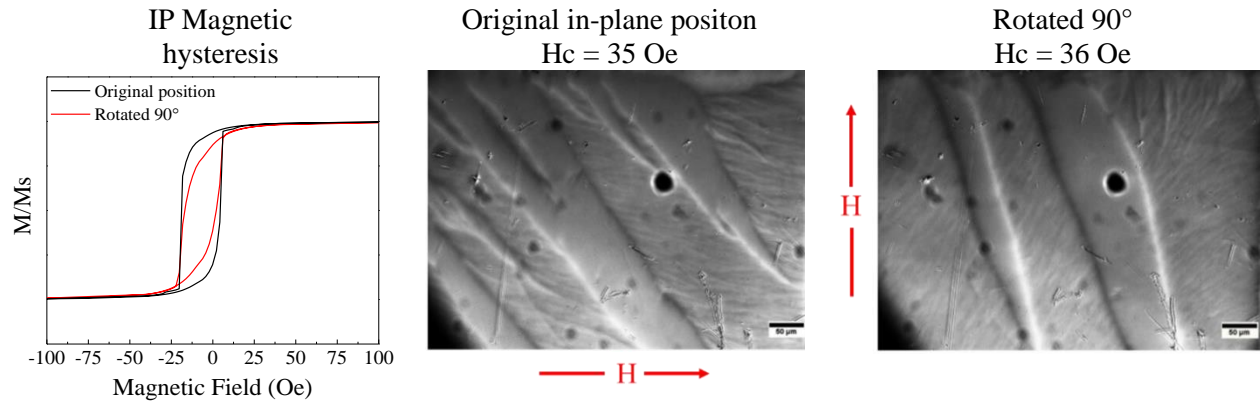


Figure 4-22. (Left) In-plane magnetic hystereses for 8 $BL_{(PNR)}$ sample showing similar coercivities, (center) domain size in 8 $BL_{(PNR)}$ sample in original orientation and (right) rotated 90° with domain sizes on the order of 100s of μm .

For 1 $BL_{(PNR)}$ and 8 $BL_{(PNR)}$, reflectivity measurements were taken at several fields below magnetic saturation to assess the subtle differences in the magnetization rotation. The 1 $BL_{(PNR)}$ sample in the left panel of Figure 4-23 shows that the two in-plane directions demonstrated a linear relationship between magnetization angle (θ_M) and applied field. The deviation in θ_M from the applied magnetic field decreases as field increases, which is expected. The 8 $BL_{(PNR)}$ sample only showed this linear relationship when the sample was rotated by 90° with respect to the applied magnetic field.

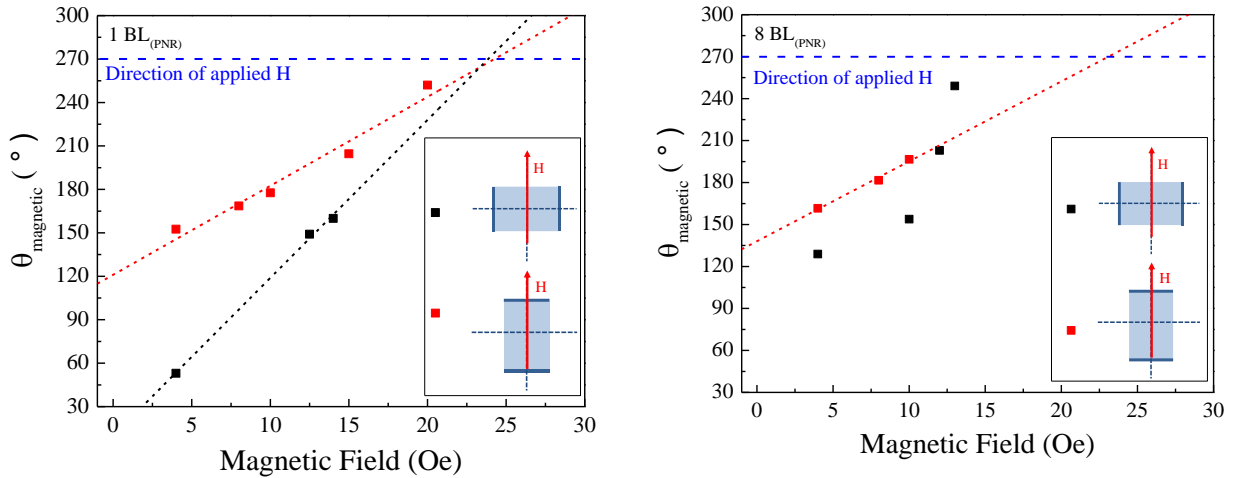


Figure 4-23. Deviation in angle of magnetization from the applied magnetic field for the (left) 1 BL_(PNR) sample and (right) 8 BL_(PNR) sample for both orientations.

These studies show that the magnetization of individual FeGa and NiFe layers did rotate coherently with applied magnetic field, however, for integration into a strain-coupled multiferroic device, it is critical to understand how the magnetization changes in the individual layers as a function of strain.

4.3.2 Magnetization Rotation of FeGa and NiFe Multilayers with Applied Strain

Due to the fact that NiFe has almost zero magnetostriction by design, it is unclear how the magnetization of those individual layers in a multilayer is affected by strain. The magnetic characterization of the 1 – 7 BL samples grown in the first part of this work show that the layers rotated coherently as shown in Chapter 4.2 and PNR was utilized to confirm this. Three samples grown on single crystal PMN-PT (011): single bilayers with a fixed FeGa thickness (20 nm) with varying thickness (7, 20 and 40 nm) NiFe grown on it. These thicknesses were chosen to be close to the exchange length of NiFe (7 nm) and well above it (20 and 40 nm). A superlattice was also grown with the structure of (20 nm FeGa/7 nm NiFe)₃/20 nm FeGa, which is a duplicate of the

thinnest bilayer, which could be more readily incorporated into a strain-coupled multiferroic device. All samples were sputter deposited at room temperature with power and pressure optimized to minimize residual stresses. Samples were grown on Si (100) for baseline characterization as well as PMN-PT (011) substrates, which provide an anisotropic strain of $+750 \mu\epsilon$ at 400 V.

Static magnetic properties were assessed at room temperature via SQUID magnetometry, while the magnetoelastic behavior was also measured. As expected, increasing the NiFe thickness reduced the coercivity of the bilayers, from 25 Oe for the 7 nm NiFe sample to 5 Oe for the 40 nm NiFe sample. A positive voltage of 400 V was applied to the samples and the hystereses measured again. All samples showed a hardening of the in-plane easy axis with positive strain, which is expected because FeGa has a positive magnetostriction.

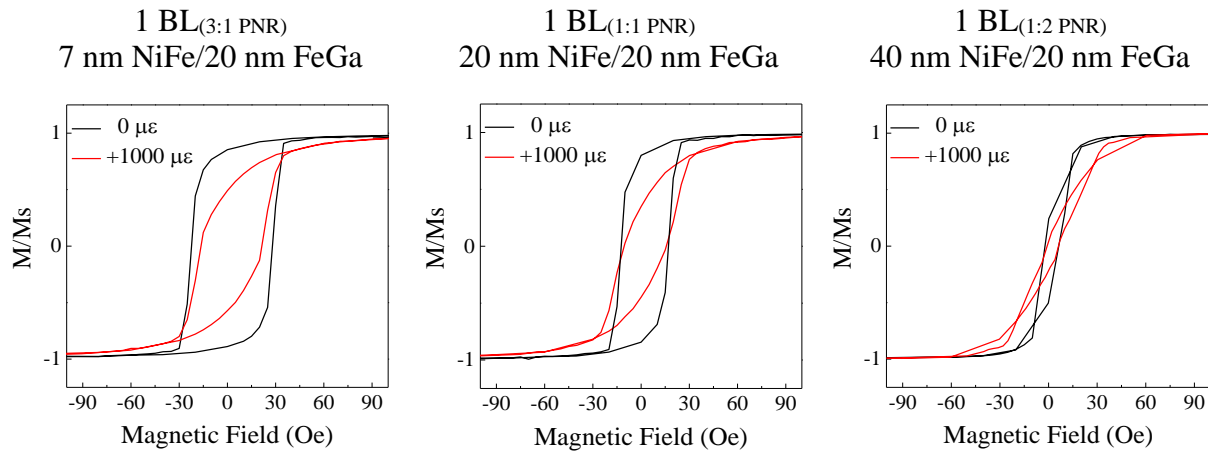


Figure 4-24. Unstrained and strained magnetic hysteresis of (left) 7 nm NiFe sample, (center) 20 nm NiFe sample, and (right) 40 nm NiFe sample with a base layer of 20 nm FeGa, all deposited on pre-poled 50 nm Pt/5 nm Ti/PMN-PT (011)/10 nm Ti/125 nm Au substrates

Out-of-plane magnetization was measured for the three bilayer samples to observe evidence of exchange-coupling between the layers and can be seen in Figure 4-25. The least noisy hysteresis loop was measured for the thinnest bilayer sample 1 BL_(3:1 PNR). As the thickness

of NiFe increased, the uniaxial anisotropy of the NiFe began to dominate the signal and any deviation in the position in the sample could contribute to this noise. All three samples show behavior that is characteristic of exchange-coupled materials, which is a hysteresis loop that does not close fully past the saturation field.

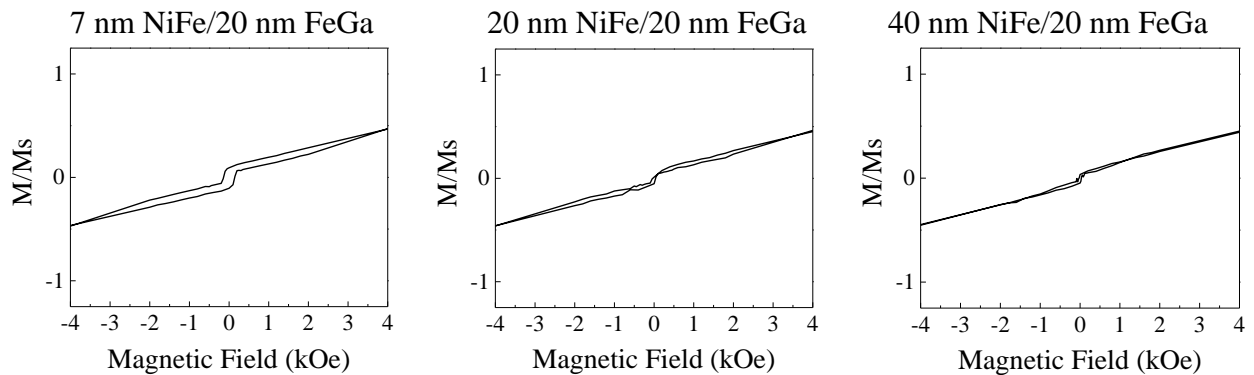


Figure 4-25. Out-of-plane magnetization measurements for the bilayer sample with (left) 7 nm NiFe, (center) 20 nm NiFe, and 40 nm NiFe (right) with a base layer of 20 nm FeGa grown on Si (100).

PNR studies were carried out on the 1 BL_(3:1 PNR), 1 BL_(1:1 PNR), and 1 BL_(1:2 PNR) samples with zero applied voltage at a saturating magnetic field of 1000 Oe, which was used to fit the nuclear and magnetic scattering length density values as shown in Figure 4-26. For all samples, there is good agreement between the data and the fits.

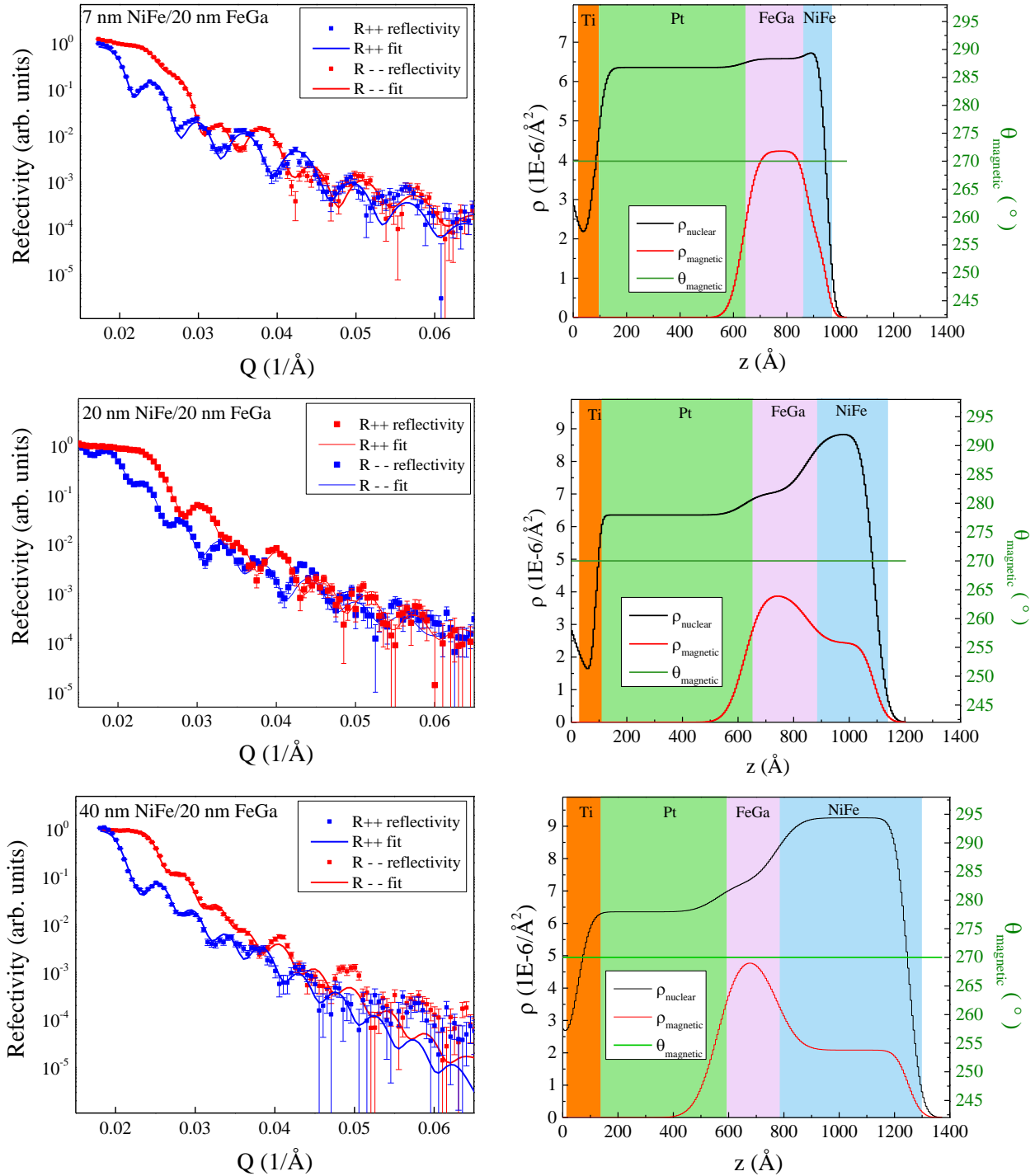


Figure 4-26. (Left) Fitted reflectivity (right) and the corresponding ρ_{magnetic} and ρ_{nuclear} profiles for 7 nm NiFe, 20 nm NiFe and 40 nm NiFe samples with a base layer of 20 nm FeGa grown on 50 nm Pt/5 nm Ti/PMN-PT (011)/10 nm Ti/125 nm Au substrates

The noise at higher values of Q is attributable to the roughness of the PMN-PT. For the 20 nm and 40 nm NiFe samples, the shift in ρ_{nuclear} and ρ_{magnetic} is very clear, but this is not the case for the 7 nm sample. The ρ_{magnetic} profile does not appear to change transitioning from FeGa to NiFe, but there is a very slight shoulder in the ρ_{magnetic} profile visible at 900 Å, indicating strong coupling between the layers. The ρ_{nuclear} profile has a very clear demarcation between the 7 nm NiFe and 20 nm FeGa layers.

Following these studies, voltage-dependent measurements were carried out to verify the magnetoelastic behavior of these bilayer samples as well as the coherence of the rotation of magnetization with varying thickness. Non-spin-flip scattering measurements were carried out at a small remnant magnetic field of 10 Oe and two voltages, 0 and 400 V, corresponding roughly to 0 and 1000 $\mu\epsilon$, respectively. The results for the 7 nm, 20 nm and 40 nm NiFe samples can be seen in Figure 4-27. All three samples have magnetic anisotropy without any applied voltage, which decreases as the thickness of NiFe increases. The difference in rotation of the magnetization of the FeGa and NiFe layers without applied voltage is 1°, indicating a coherent anisotropy. With applied voltage, the rotation of the magnetization for all samples roughly doubles, though this effect is slightly higher for the 20 nm NiFe sample. The 20 nm and 40 nm NiFe samples showed coherent rotation within +/- 1°, but the 7 nm NiFe sample showed a larger deviation between the layers, which can be attributed to the stronger anisotropy of this sample from the NiFe layer.

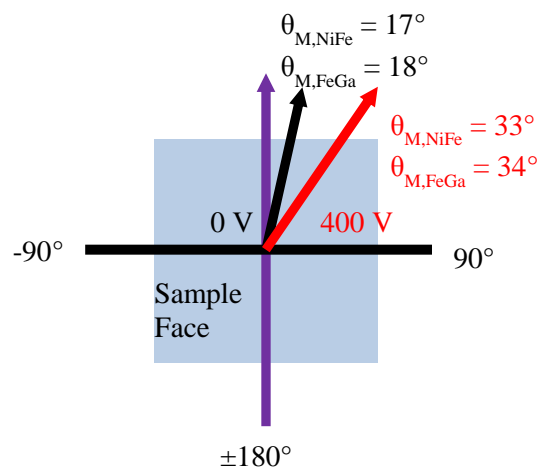
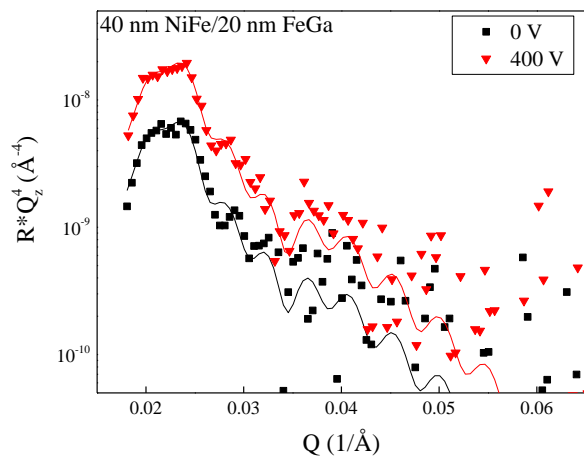
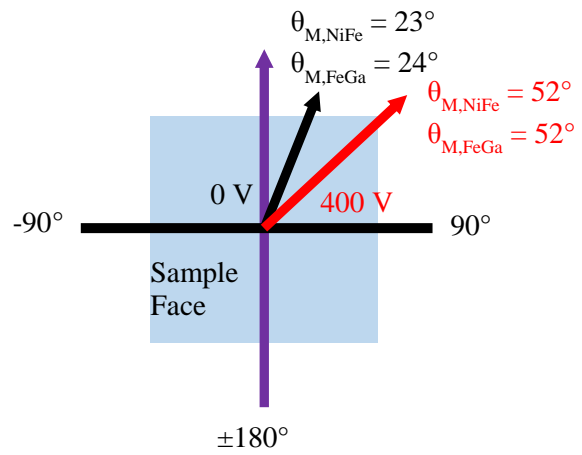
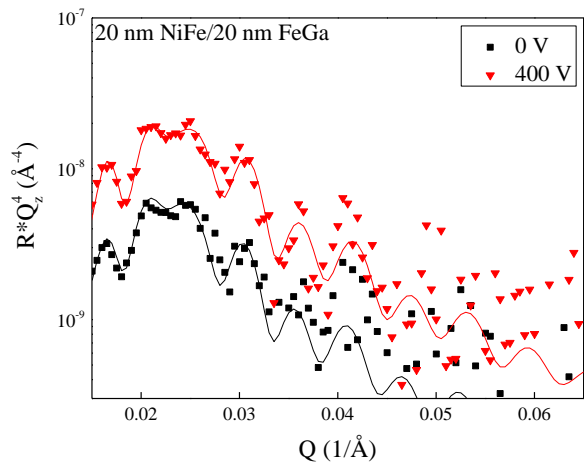
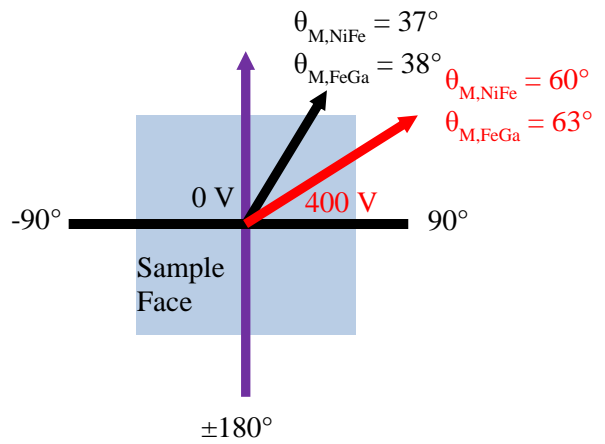
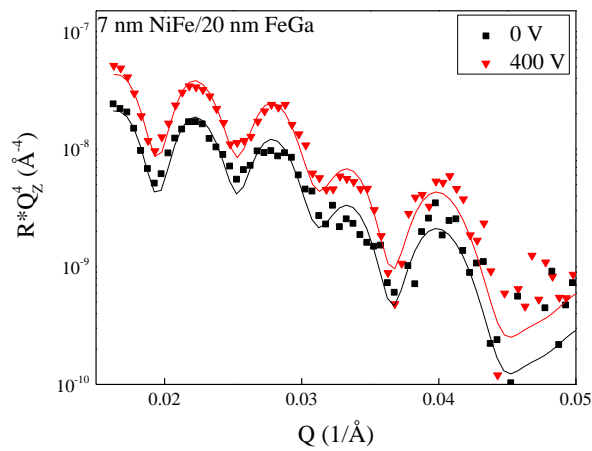


Figure 4-27. (Left) Fitted remnant reflectivity (right) the corresponding magnetization rotation at 0 and 400 V for the 7 nm NiFe, 20 nm NiFe and 40 nm NiFe bilayer samples.

These experiments have demonstrated that for a single NiFe/FeGa bilayer, the magnetization induced by the piezoelectric strain is enough to rotate the magnetization of both layers coherently. Additionally, they showed that NiFe possessed a thickness dependent anisotropy which dictates the magnetization rotation at 0 V. Based on this effect, it is possible that the anisotropy of the NiFe is influencing that of the FeGa, which supports the notion that these layers are indeed exchange-coupled. From here, a superlattice structure was selected based on the evidence of exchange-coupling, as seen in the left panel of Figure 4-28, as well as some polarized neutron reflectivity data of samples grown on Si.

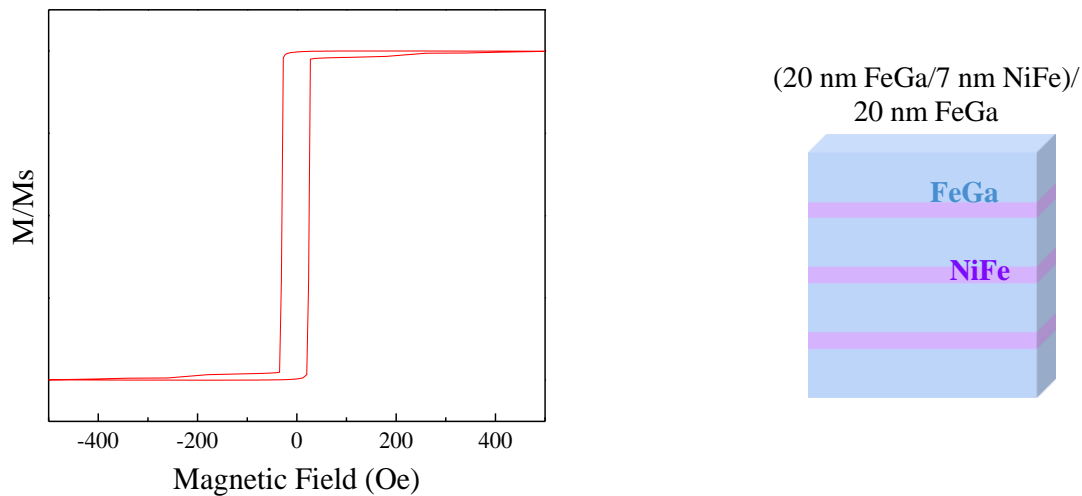


Figure 4-28. Magnetic hysteresis of a 3 BL sample with the structure (20 nm FeGa/7 nm NiFe)₃/20 nm FeGa/Si.

The fitted R_{++} and R_{-} non-spin flip spectra were used to determine the scattering length density profile as shown in Figure 4-29. The reflectivity fits are in good agreement with the experimental data, though there is more noise at higher values of Q . The values ρ_{magnetic} and ρ_{nuclear} for FeGa and NiFe both agree well with reported values, though there is some oxidation at the top layer of FeGa that causes ρ_{magnetic} to decrease.

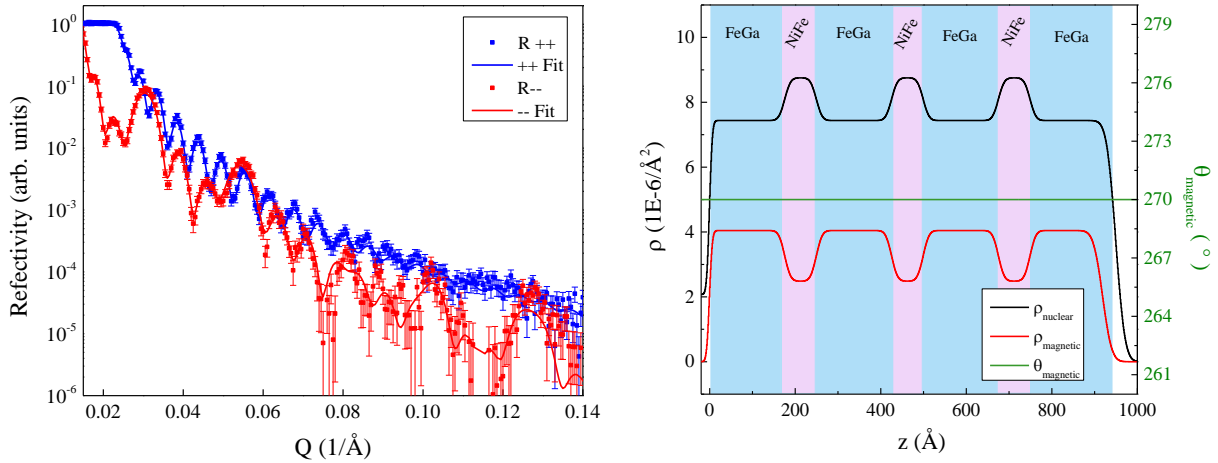


Figure 4-29.(Left) Non-spin flip reflectivity measurements for (20 nm FeGa/7 nm NiFe)₃/20 nm FeGa/Si and (right) the corresponding ρ_{magnetic} and ρ_{nuclear} profiles.

The spin flip spectra, R_{+-} and R_{-+} , were measured and fitted to determine the direction of the magnetization vector at a remnant field of 10 Oe and can be seen in the left panel of Figure 4-30. The sample demonstrated a fairly strong anisotropy, most likely from the NiFe layers, which led to a coherent magnetization rotation of 16° from the applied field of 10 Oe. With the confirmation that the magnetization of the superlattice rotates with applied magnetic field, its ability to rotate with strain was investigated.

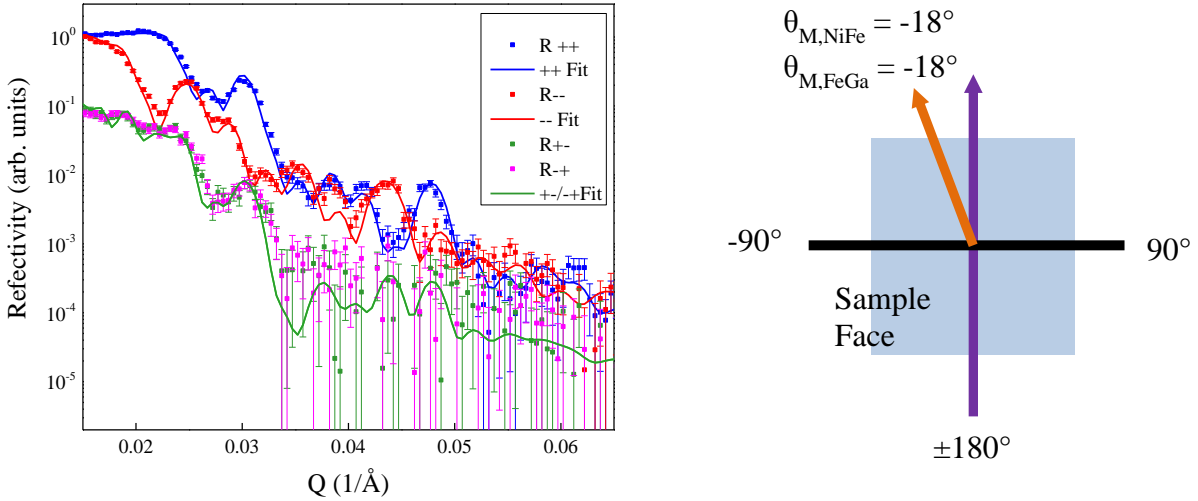


Figure 4-30. Spin-flip (R+- and R+) and non-spin flip (R++ and R- -) spectra and fits (left) and a schematic of the rotation of the magnetization vector at 10 Oe.

A sample with the structure (20 nm FeGa/7 nm NiFe)₃/20 nm FeGa was grown on a prepoled 50 nm Pt/5 nm Ti/PMN-PT (011)/10 nm Ti/125 nm Au substrate at room temperature with residual stresses minimized and a growth rate of 3 nm/min. Non-spin flip reflectivity measurements were taken at a saturating field of 1000 Oe and fitted to determine the ρ_{magnetic} and ρ_{nuclear} profiles profile as seen in Figure 4-31. Fitting the profile for this sample proved complicated for several reasons. First, the roughness of the PMN-PT led to a rough interfacial Ti adhesion layer that is almost of the order of the entire layer thickness. Atomic force microscopy of the PMN-PT substrates purchased confirm an RMS of roughly 2.3 nm over a $1 \times 1 \mu\text{m}$ area. The second difficulty of this fitting was due to the top FeGa layer, where both ρ_{magnetic} and ρ_{nuclear} diminished halfway through the film, so it was treated as two separate layers in the fitting process. Finally, both ρ_{magnetic} and ρ_{nuclear} were found to be significantly lower compared to the same sample grown on Si, which can be attributed to roughness propagated from the PMN-PT.

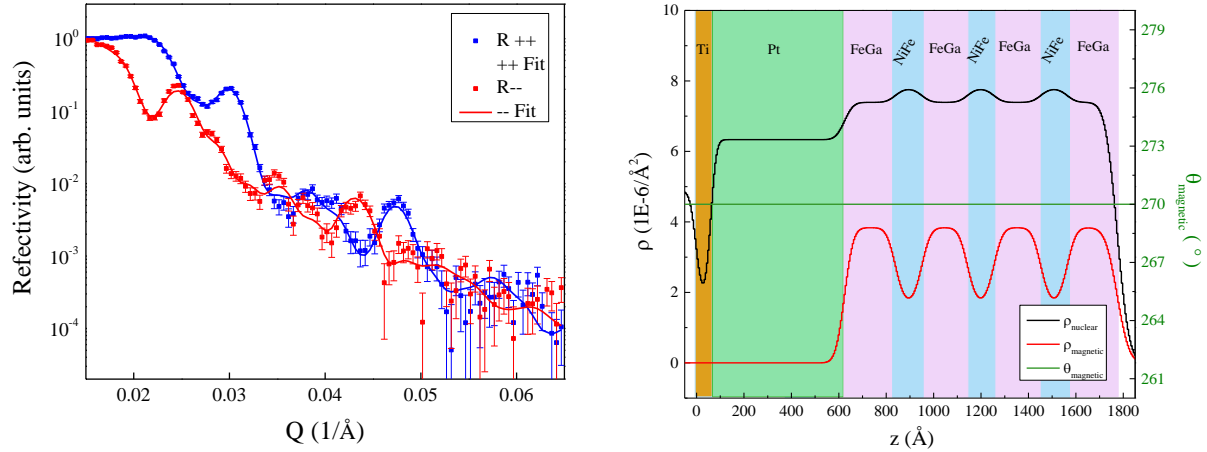


Figure 4-31. (Left) Reflectivity measurements on (20 nm FeGa/7 nm NiFe)₃/20 nm FeGa/50 nm Pt/5 nm Ti/PMN-PT (011)/10 nm Ti/125 nm Au) (right) and the corresponding ρ_{magnetic} and ρ_{nuclear} profiles.

With the baseline parameters determined, the effect of strain on the magnetic hysteresis of this sample was assessed. Since the PMN-PT (011) provides a uniaxial strain profile with applied voltage, the magnetic hysteresis was measured with strain field parallel and perpendicular to the applied magnetic field, H , which can be seen in Figure 4-32. Both measurements indicate a coherent rotation and show complementary behavior: parallel strain makes the easy in-plane axis magnetically harder and perpendicular strain makes the axis easier.

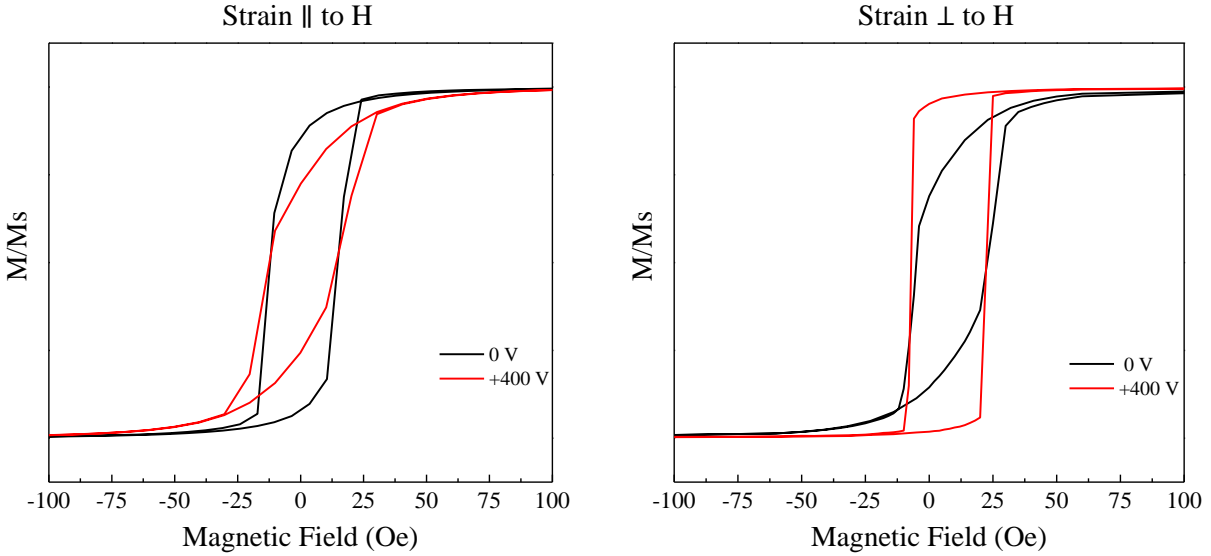


Figure 4-32. Poled magnetic hysteresis measurements with (left) strain parallel to the applied magnetic field and (right) perpendicular to the applied magnetic field.

Remnant reflectivity measurements were carried out to observe the coherence as well as the magnitude of the magnetization rotation in this superlattice structure. The spin flip data in the top panel of Figure 4-33 shows a change in intensity when plotted in terms of reflectivity (R) times Q^{-4} versus Q . The physical model that provided the best fit indicated that all of the layers were rotating coherently with applied strain. The magnetization angle extracted from the model is shown in the bottom panel of Figure 4-33, which shows an increase of rotation as the voltage increases. After applying 400 V, the magnetization rotation vector is found to be 45° from the applied magnetic field. Conversely, the sample was rotated to 45° from the normal plane to determine if there was an 8-fold anisotropy in the rotation vector. The spin flip components were measured as a function of voltage after rotating the sample by 45° with respect to the applied magnetic field. The magnetization shows that when the voltage is increased to 400 V, the magnetization vector rotates further from the normal plane. Non-coherent rotation models were also explored, however they are not consistent with the experimental data.

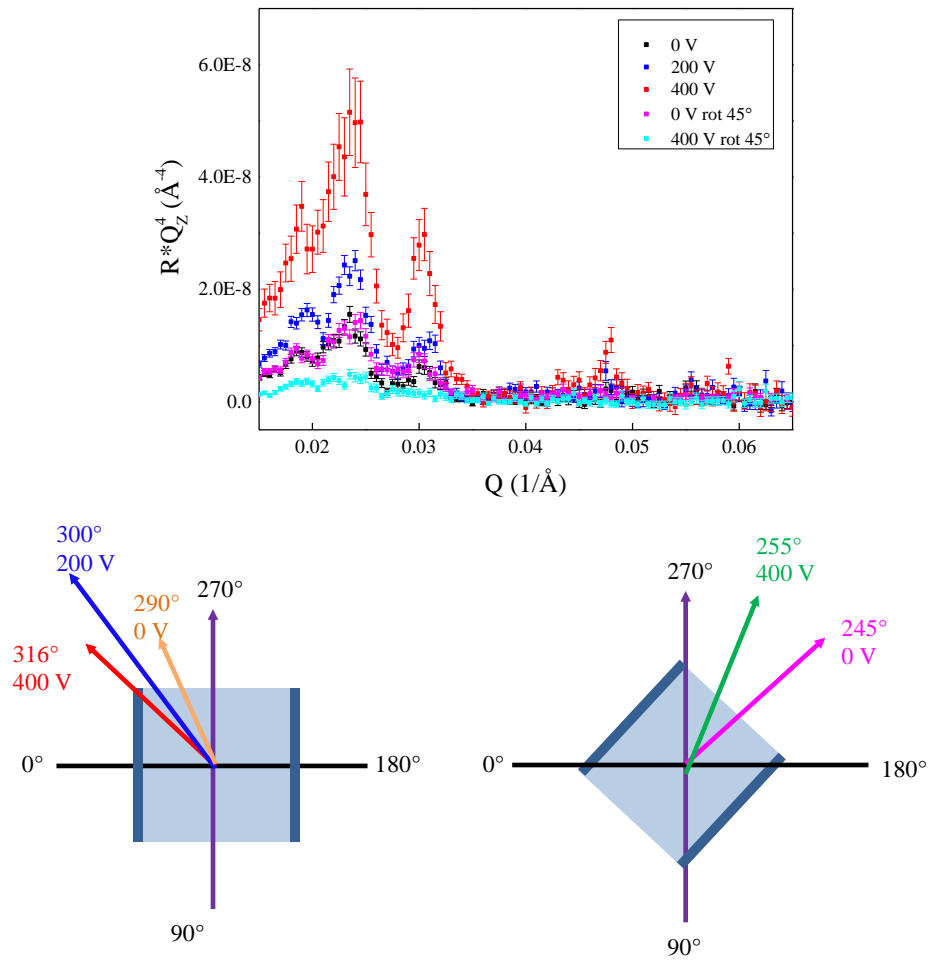


Figure 4-33. (Top) Spin-flip scattering for FeGa (20 nm FeGa/7 nm NiFe)₃/20 nm FeGa superlattice as a function of applied voltage (bottom) and the corresponding magnetization rotation in two different sample positions.

For the case of strain parallel to applied field, the voltage control of the magnetization rotation appears to be deterministic and linear, as shown in the left panel of Figure 4-34. Only two measurements were taken when the sample was rotated by 45°, but the trend appears to be similar.

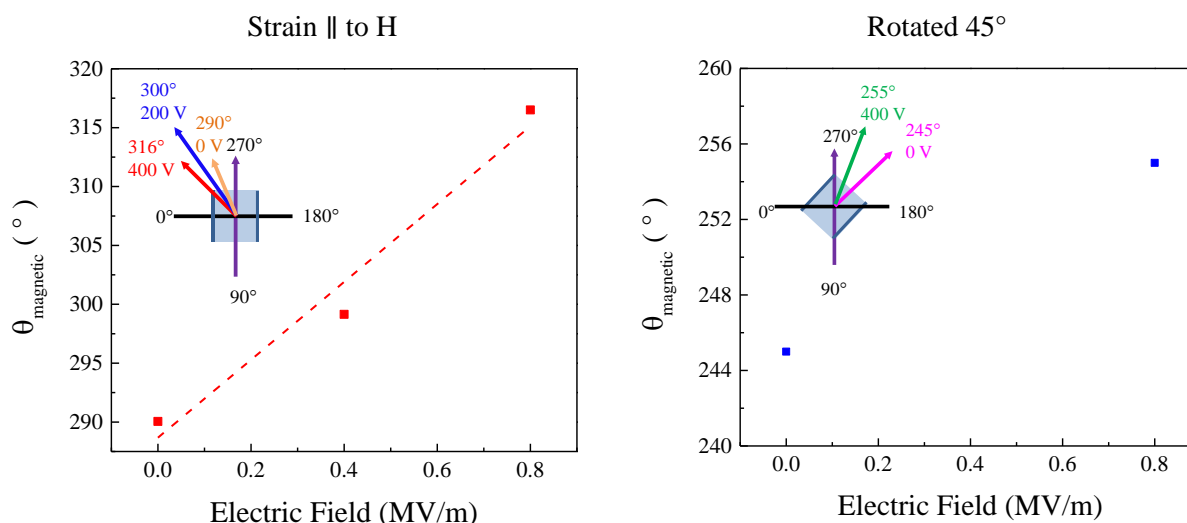


Figure 4-34. Degree of magnetization of rotation with electric field for the cases of (left) strain parallel to the applied magnetic field and then (right) rotated by 45°.

From these studies, all samples showed coherent rotation of magnetization with applied magnetic field. The three single BL samples measured showed coherent rotation for NiFe layer thicknesses up to 40 nm, well-beyond the exchange length of either material. The magnetization induced by strain in the FeGa layer combined with the small remnant field leads to coherent rotation, regardless of the layer thickness. This indicates that these heterostructures are viable candidates for integration into a multiferroic antenna, and that the coupling is deterministic and strong even with thick layers.

Chapter 5 : Multiferroic Device Characterization

With the magnetic properties optimized and the coherent rotation of the magnetization verified, FeGa/NiFe heterostructures were incorporated into two different antenna devices to determine their functionality in devices. Integration into SAW devices showed that FeGa/NiFe multilayers are able to absorb 17% of the energy of an acoustic strain wave. A FeGa/NiFe multilayer integrated into a BAW structure demonstrated a narrow FMR linewidth of 35 Oe and a high permeability of up to 1000 at 3.1 GHz

5.1 Integration into Surface Acoustic Wave Antenna

As discussed in Chapter 2, SAW characterization was used primarily for quantifying the high frequency magnetoelastic behavior of the FeGa/NiFe multilayers. To this end, two samples were fabricated: a 50 nm thick sample with the structure of $(4.2 \text{ nm FeGa}/5 \text{ nm NiFe})_5/4.2 \text{ nm FeGa}$ and a 100 nm thick sample with the structure of $(8.3 \text{ nm FeGa}/10 \text{ nm NiFe})_5/8.3 \text{ nm FeGa}$. The magnetic properties were measured via VSM to determine the easy axis as well as the magnetization. The sample with much thinner layers showed perpendicular magnetic anisotropy (PMA), as shown on the left panel in Figure 5-1.

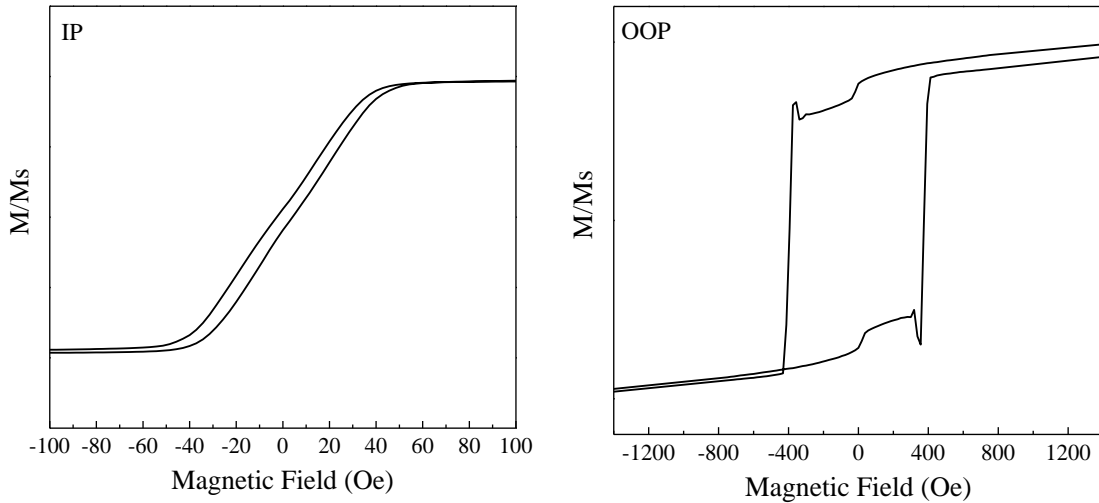


Figure 5-1. (Left) In-plane and (right) out-of-plane hysteresis loops for a (4.2 nm FeGa/5 nm NiFe)₅/4.2 nm FeGa (5 BL_(SAW1)) sample that shows perpendicular magnetic anisotropy.

Magnetometry for the 100 nm sample showed strong in-plane anisotropy and exchange-spring like behavior out-of-plane as shown in Figure 5-2. The thicker layers did not fully couple with one another as they did in the thinner sample.

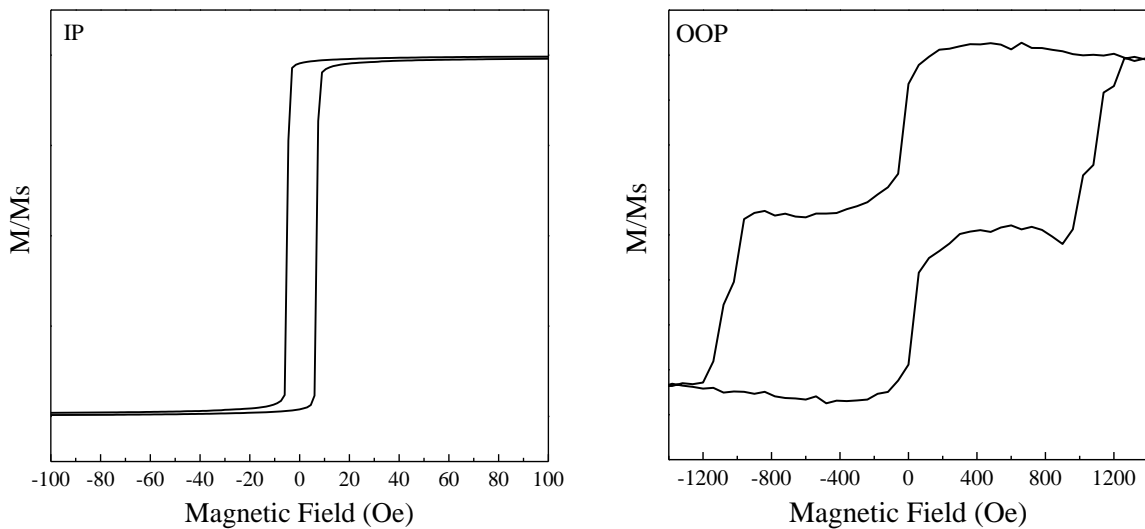


Figure 5-2. In-plane (left) and out-of-plane (right) hysteresis loops for a (8.3 nm FeGa/10 nm NiFe)₅/8.3 nm FeGa sample (5 BL_(SAW2)) that shows exchange-spring behavior.

The 5 BL_(SAW1) sample was measured via the ADFMR technique as described in Chapter 2. The magnetic field was swept from -100 to 100 Oe, well past the saturation field for this sample. All measurements using this technique are taken in-plane. The frequency selected for this sample was 1.433 GHz and the plot of field-dependent absorption can be seen in Figure 5-3. Since this sample showed PMA, absorption at 0° and 90° with respect to the applied magnetic field was expected and observed. The maximum absorption was -0.8 dB, corresponding to roughly 17% absorption of the acoustic wave energy via the magnetic material at 1.433 GHz. One interesting phenomena is the emergence of small dips that vary depending on the applied field. The dips appear to move out from the center radially, with some degree of twisting. This test setup was designed for in-plane measurements exclusively, and the dynamic magnetoelastic behavior could not be extracted for this thinner sample.

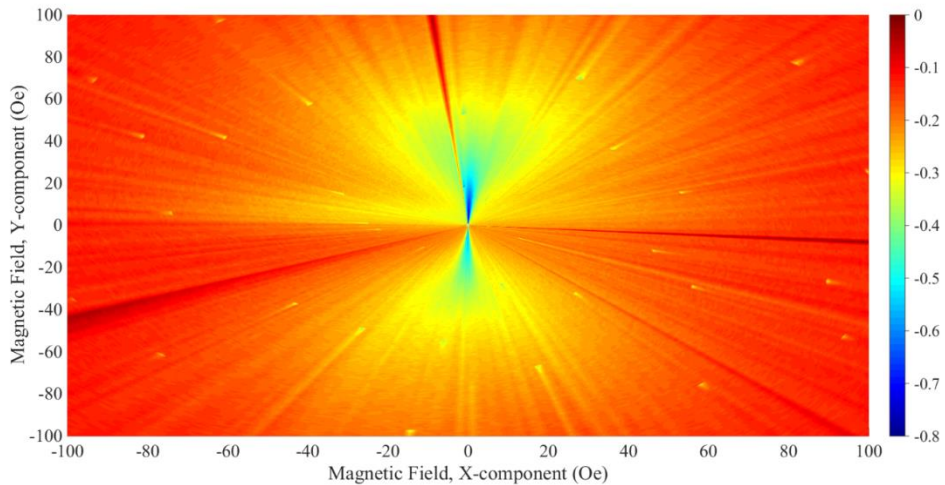


Figure 5-3. Absorption of acoustically driven FMR spectra as a function of X and Y components of magnetization for a (4.2 nm FeGa/5 nm NiFe)₅/4.2 nm FeGa sample.

The 5 BL_(SAW2) sample was measured at 1.433 GHz with fields swept from -500 to 500 Oe in-plane. Since magnetic hysteresis measurements showed that this film had in-plane anisotropy, the field-dependent absorption showed asymmetric 4-fold lobes as shown in Figure

5-4. The maximum absorption for this sample was -0.6 dB, corresponding to 13% absorption of the acoustic wave energy, much lower than that of nickel. Though this was surprising because of FeGa's higher magnetostriction, the magnetoelastic energy decreases with increasing saturation magnetization, and so this is another aspect that must be considered.

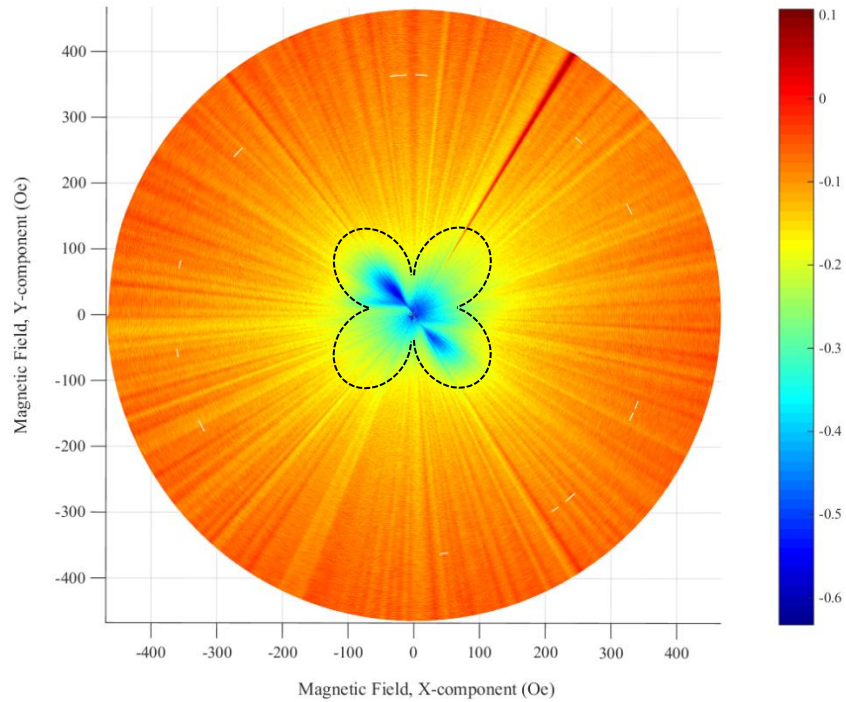


Figure 5-4. Absorption of acoustically driven FMR spectra as a function of X and Y components of magnetization for a (8.3 nm FeGa/10 nm NiFe)₅/8.3 nm FeGa sample. The dashed lines are a visual guide for the 4-fold lobes.

5.2 Integration into Bulk Acoustic Wave Antenna

A 385 nm 12 BL_(BAW) sample with the structure of (25 nm FeGa/5 nm NiFe)₁₂/25 nm FeGa was grown for integration into a multiferroic BAW antenna. Residual stress were optimized by varying the sputtering conditions. In-plane magnetic hysteresis measurements showed strong in-plane anisotropy with low coercivity of 4 Oe and high magnetization of 1180 emu/cc, indicating sufficient magnetic softness and magnetization.

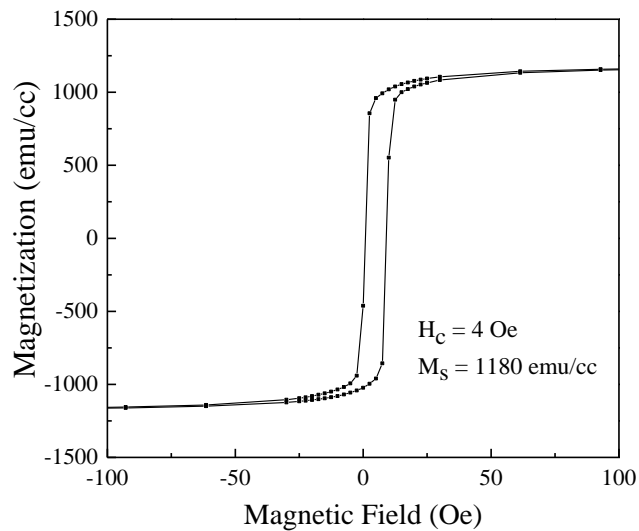


Figure 5-5. In-plane magnetic hysteresis of a (25 nm FeGa/5 nm NiFe)₁₂/25 nm FeGa with a coercivity of 4 Oe and a saturation magnetization of 1180 emu/cc.

Stripline measurements were performed in order to assess the high frequency magnetic properties as a function of both frequency and field. The permeability of the sample was determined to be 1000 at a bias field of 93 Oe and the FMR linewidth at 3.5 GHz was determined to be 35 Oe. Both of these properties verify that these multilayers would perform well in a multiferroic antenna.

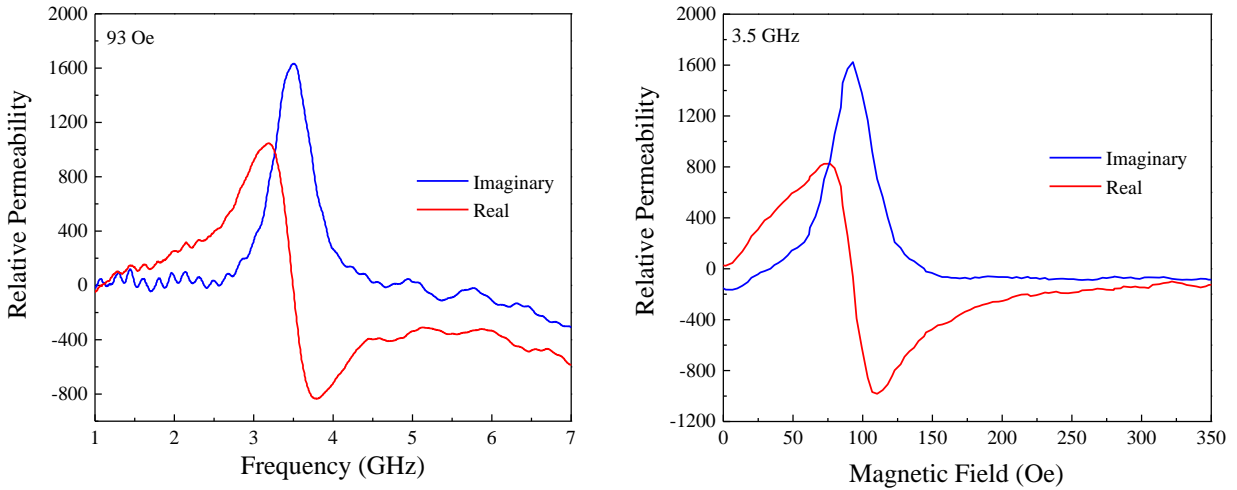


Figure 5-6. Broadband permeability measurement of a (25 nm FeGa/5 nm NiFe)₁₂/25 nm FeGa sample at a bias field of 93 Oe (left) and a variable field measurement at 3.5 GHz (right).

Residual stresses in the AlN layer led to the devices buckling and fracturing at the anchor points and so these measurements were performed on samples deposited at the same time. Though device failure occurred for these samples before the transmission coefficients could be measured, the properties measured indicated that these multilayers would have likely been able to convert the incident EM wave into an acoustic wave.

Chapter 6 : Summary

The ability to control the properties of magnetostrictive ferromagnets is desirable for high-frequency multiferroic applications. In this work, two material systems, FeGaB and FeGa/NiFe multilayers, were developed and evaluated as candidates for integration into a multiferroic antenna.

The first thrust of this work focused on developing sputter-deposited $(\text{Fe}_{75}\text{Ga}_{25})_{1-x}\text{B}_x$ (where $0.11 < x < 0.19$) alloys, which served as a benchmark for high-frequency magnetoelastic materials. Doping with boron reduced the magnetocrystalline anisotropy, the major loss mechanism in FeGa, by disrupting the crystal structure. Using this doping method, the coercivity was reduced dramatically compared to FeGa, from 55 Oe to 18 Oe or 70%. FMR linewidth was reduced as well, from 600 Oe to 210 Oe, a change of 70 % as well. A thickness dependence of these magnetic properties was observed due to shape anisotropy. FeGaB maintained a relatively high value for saturation magnetostriction of $50 \mu\epsilon$. However, the linewidth was significantly higher than the target value of 40 Oe, so the multilayer approach for tuning the magnetic properties was considered.

The tunability of FeGa/NiFe composites was investigated to take advantage of their complementary magnetic properties: the low loss and magnetic softness of NiFe and the high degree of magnetomechanical coupling of FeGa. FeGa/NiFe multilayers were grown in a variety of geometries and to explore the effect of layer thickness on the magnetic properties. Holding total thickness at 100 nm and the same amounts of both phases, it was found that a layer thickness of around 10 nm allowed for the optimal softness and FMR linewidth, while maintaining a large magnetostriction. The ability to tune magnetic properties with easily controllable parameters, such as layer thickness and number, is valuable for developing strain-

coupled multiferroic composites. This tunability was determined to originate from the size of magnetic domains in the films. As the thickness of the layers was decreased from 25 nm to 5 nm, the in-plane domain size increased from 20 μm to over 100 μm in size, indicating that the thinner layers restrict the out-of-plane domain formation.

The deterministic rotation of magnetization with applied magnetic field and applied strain was evaluated via polarized neutron reflectometry. Because these multilayers are composed of a magnetoelastic phase (FeGa) and less magnetoelastic phases (NiFe), it is critical to verify that the layers rotate coherently with applied strain before they were integrated into a device. Magnetometry measurements indicated the magnetization of the multilayers were rotating coherently, so the thickness dependence on this effect was evaluated for single bilayer films with varying thicknesses of the less magnetoelastic NiFe, ranging from 7 – 40 nm. For all samples, there was little variation in the rotation of the magnetization of either layer, indicating coherent rotation even for fairly thick layers, indicating a robust material system.

Device functionality was assessed by integrating multilayer samples into two different antenna architecture. A surface acoustic wave (SAW) structure was used to probe the ability of the material to absorb a strain wave from piezoelectric LiNbO_3 . Two samples, 5 $\text{BL}_{(\text{SAW}1)}$ and 5 $\text{BL}_{(\text{SAW}2)}$, were evaluated and absorbed up to 17% of the acoustic energy from the strain wave. A bulk acoustic wave (BAW) structure was used study how the material could convert the energy from an electromagnetic wave into an acoustic wave. A thick 12 $\text{BL}_{(\text{BAW})}$ sample was integrated into a device and showed a low FMR linewidth and high permeability, but the devices failed due to stresses.

This work provided the proof of concept that both doping and interfacial engineering are viable approaches for tuning the magnetic properties of FeGa, and could be extended to other

magnetoelastic systems. Multilayer magnetic materials are a promising alternative to single-phase ferromagnetic materials as well as doped material systems for resonator or sensor applications. The low coercivity, high permeability, and high strain sensitivity of these samples make them promising candidates for high frequency, strain-coupled multiferroic systems.

Moving forward, these FeGa/NiFe multilayers can be integrated into second generation BAW devices that have been optimized to mitigate residual stresses to determine how well these multilayers can convert an EM wave into an acoustic wave. Subsequently, other material systems can be explored, such as TbFe₂, a material with largest room temperature magnetostriction, to determine if magnetic multilayers are a viable approach for tuning properties of materials other than FeGa.

Appendix

A. Operating Procedures

A.1: Ulvac JSP 8000 Sputtering Tool

Safety Precautions

1. Do not override or bypass any safety interlocks at any time. Only people who are certified or are in supervised training may operate this tool. Always handle hazardous materials carefully and safely. The Preparation Chamber door has several pinch points and so it
2. Conductive targets should be installed in the DC cathodes (C3/C4) and insulating ones should be installed in the RF cathodes (C1/C2)

A.1.2. Emergency shutdown

1. The red emergency switch is on the front of the control cabinet. Press this switch immediately in case of emergency. This will shutdown the whole system.

A.1.3. Maintaining vacuum integrity

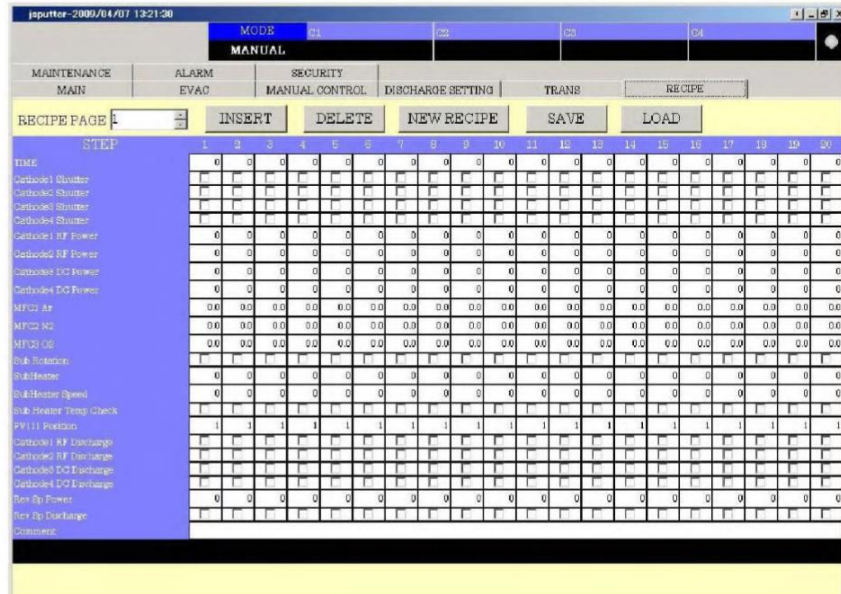
1. Never touch any part(s) inside the chamber or part(s) going into the chamber with ungloved hands or contaminated gloves.
2. Handle wafer and wafer piece carrier with appropriate vacuum tools or gloved hands.
3. Avoid unnecessary touching/handling of chamber parts and vacuum system tools, even with gloves on.
4. Clean any area or tool which will contact vacuum chamber parts by wiping with lint-free wipes and isopropyl alcohol.
5. The vacuum chamber should not be subjected to excessive atmospheric exposure; pre-deposition preparation should be done in a timely manner to avoid such exposure.
6. A cleanroom mask must be worn while the chamber is open.
7. Load only clean substrates and clean substrate holder/fixtures into the vacuum chamber.
8. The system is designed to process semiconductor wafers with no films that outgas. Any non-standard substrate such as plastics or unbaked photoresist, must not be put in the system without the area engineer's approval.

A.1.4 Startup Checklist

1. Verify the previous experiments using the tool were successful.
2. Record the base pressure on the log sheet (should be $< 2 \times 10^{-6}$ torr before beginning an experiment, and if pumping down overnight it should be $< 1 \times 10^{-6}$ torr).
3. Verify the cooling water is on and that the tool is in AUTO mode.

A.1.5. Creating a recipe

1. Click the RECIPE tab to enter the recipe editing window
2. Click LOAD for a list of available recipes. All recipes are stored under “Colin Rementer” and organized by material. Current folders are as follows: Misc, Al₂O₃, FeGa, NiFe, FeGa/NiFe, and TbFe₂.



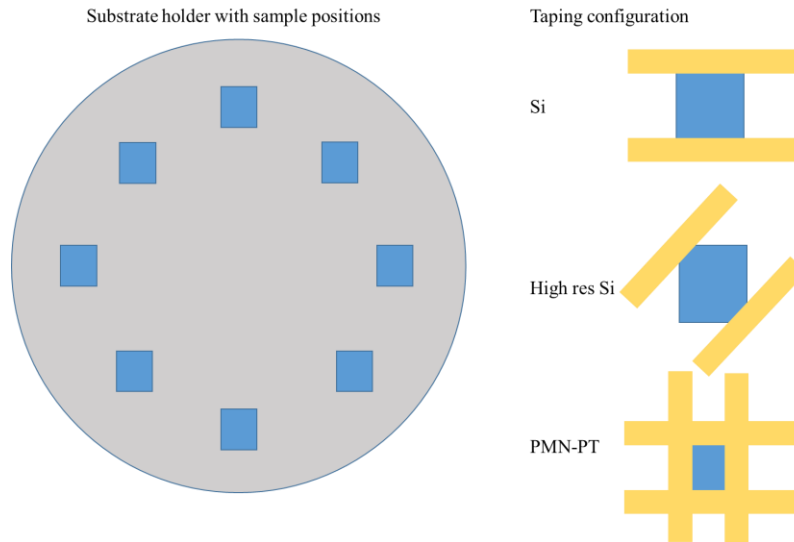
3. Select the appropriate recipe and edit the parameters as needed. The process parameters that will impact film quality directly are power, argon flow rate, and the substrate temperature. Generally, the plasma should be ignited with 50 sccm of argon flow and 100 W power by checking the “Cathode Discharge” box specific to the material during that step.
4. For insulating targets, the power should be ramped up slowly in 20 W increments to avoid thermal shock that may lead to cracking the target.
5. Ensure that substrate rotation is checked for every step of the process, or there will be an error.
6. Prior to each run, the target should be run with the shutter closed to remove the surface oxidation or cross-contamination from other targets. This time should be at least 15 minutes if the target has just been installed and 5 minutes otherwise.
7. Ensure that during the deposition step the corresponding cathode shutter box is checked.

A.1.6. Heated deposition

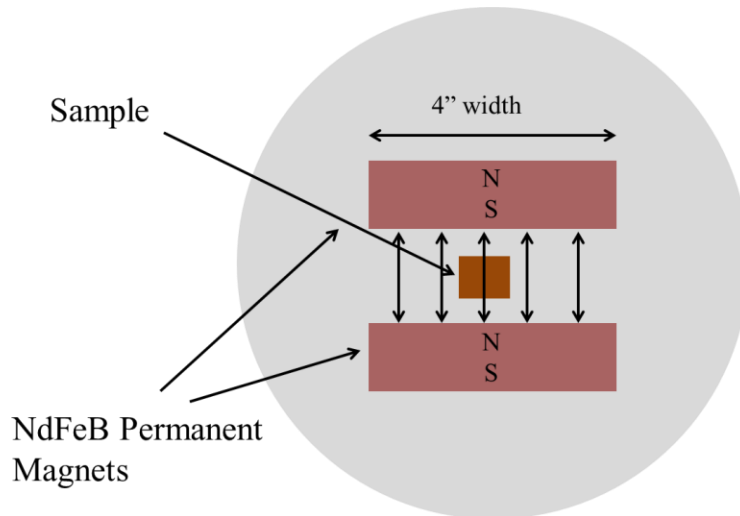
1. Heat in 25°C increments with a step length of 200 seconds.
2. Set the “Sub Heating Speed” to 10
3. On every step but the first heating step, check the “Sub Heating Temp Check” box so that the temperature setpoint will be reached.
4. After deposition, the substrates take 8 hours to cool.
5. When changes to the recipe are complete, save it. If modifying from another recipe, make sure to “Save As” a new file name.

A.1.7. Mounting a sample

1. The 8 inch substrate holder can hold up to four 4 inch wafers, but the most consistent uniformity is achieved when the samples are positioned halfway between the center and edge around the holder. Sample placement suggestions are shown below.

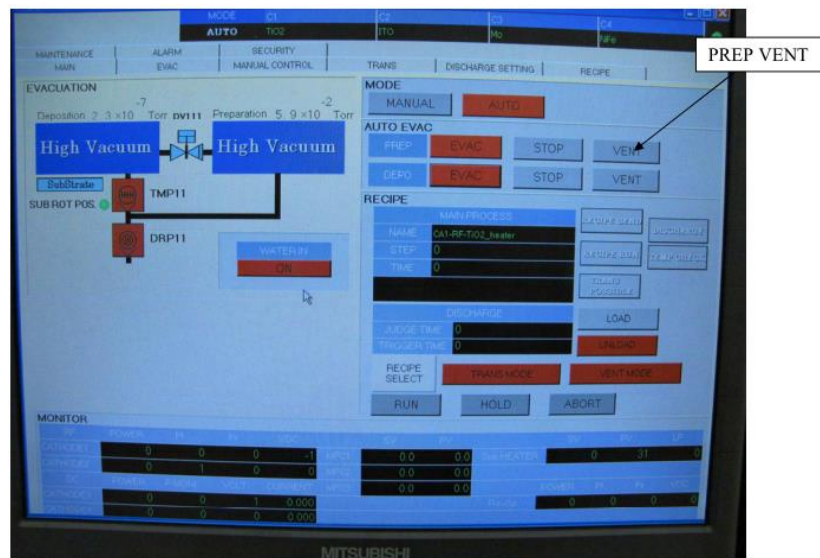


2. Mount the samples with Kapton™ tape for depositions below 150°C in the configuration shown above depending on the substrate.
3. If a deposition is carried out above 150°C, use the set screws and plates in the blue Tupperware.
4. If the substrate is flaking metal, it can be cleaned by carefully scraping the surface with a razor blade and vacuuming the particles with the CHA vacuum. Otherwise, contact the engineer in charge for help cleaning it.
5. If *in situ* magnetic biasing is desired, use the substrate located on the second to last shelf in the cabinet next to the sputtering table. It is a 6 inch aluminum plate that fits into the outer ring of the high temperature substrate holder. The samples can be positioned between the magnets in various positions to adjust the field from 50 Oe up to 1000 Oe. Verify the field with the magnetometer and position samples accordingly. This substrate CANNOT be used for heated depositions.

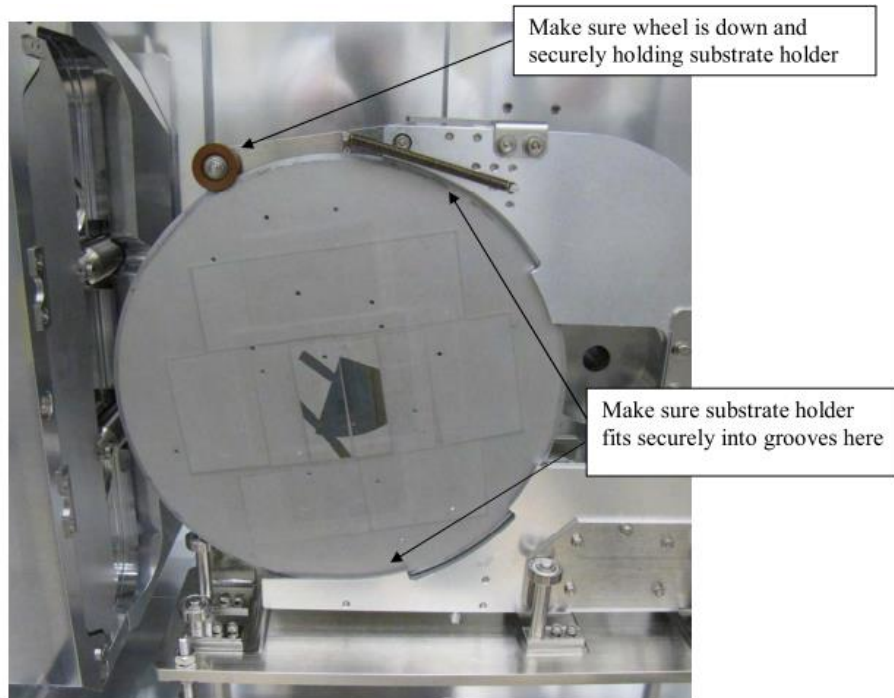


A.1.8. Loading the substrate

1. Sign in on Labrunner to disable the interlock, which will prevent the preparation chamber from fully venting
2. Select the MAIN tab, click PREP VENT then YES to the pop-up window



3. After the preparation chamber vents fully, indicated by the ATM PRESSURE sign, use the two latches to open the chamber.
4. Make sure the door does not swing closed, as this will require the interlock to be reset.
5. Remove the substrate holder and load the new one, making sure the wheel is down and that it fits securely into the transfer arm. **If the wheel is not in place, the substrate will fall in the deposition chamber and will require the system to be vented.**



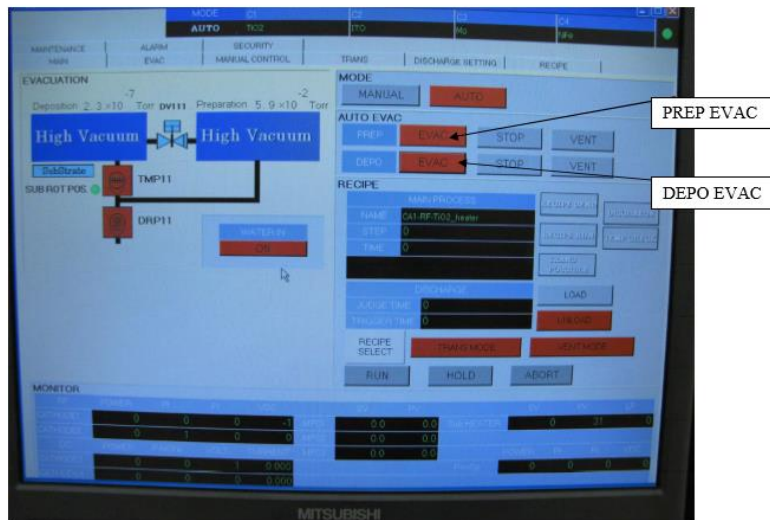
6. Check the O-ring around the chamber door for debris and wipe if necessary
7. Close the door and secure the latches.
8. From the ALARM tab, click ALARM RESET, then YES in the pop-up
9. Ensure that the red warning has changed to black.

A.1.9. Deposition

1. Click the MAIN tab.
2. From the ALARM tab, click ALARM RESET, then YES in the pop-up.
3. Select TRANS MODE and VENT MODE.
4. TRANS MODE will dictate if the substrate holder will be transferred to the preparation chamber after. VENT MODE will dictate whether or not the preparation chamber will vent once the substrate holder has been transferred to it. For overnight runs and air sensitive samples, turn off VENT MODE.
5. Click RECIPE SELECT and load the desired recipe. Listing the recipes by date modified will make this easier.
6. Verify the desired recipe by the NAME box.
7. Click RUN to begin the process.
8. The tool will pump down the preparation chamber (<100 mTorr), load the sample into the Deposition Chamber, pump down to the predeposition process base pressure (5×10^{-6}

torr), deposit material, unload sample back to the Preparation Chamber and finally vent the Preparation Chamber.

9. If you are present when the machine is running, copy the deposition parameters in to the logbook. Verify that the shutters open fully by peering into the viewport on the left side of the chamber.
10. Once the deposition is completed and the preparation chamber is vented, open both latches and remove the substrate.
11. Replace with the empty substrate, close the door and latches, then reset the alarm.
12. On the MAIN tab, select PREP > EVAC then YES in the pop-up
13. Wait until pumpdown (< 100 mTorr) and for the EVAC field to turn red
14. Select DEPO > EVAC, then YES in the pop-up to resume pumping the deposition chamber.



A.1.10. Troubleshooting

1. Discharge Error Alarm

- 1) Recipe error: There is an incorrect value for power or pressure that makes the plasma unsustainable (generally very low values for either). Adjust this and try to rerun the recipe.
- 2) Shutter issue: When carrying out multilayer depositions, the shutters opening and closing can result in the plasma to cut out at very low deposition pressures. Adjust the pressure to make sure the targets ignite individually.
- 3) Power supply: It's possible that the power supply was switched off accidentally by a CHA user vacuuming their chamber. Check to make sure all are on and operational.
- 4) Electrical short: There is a short between the cathode and the target. This can be caused by a flake of metal attracted to the strong magnets behind the target. Verify the issue by restarting the run and looking at the current and voltage for each cathode. If the current goes very high (> 1 A), a short has occurred, the deposition chamber will need to be vented and the cathodes need to be inspected by ISNC technicians.

2. Sub Rotate Alarm

- 1) Recipe error: The simple case is that the substrate rotation box in the recipe isn't selected for one of the steps.
- 2) Serious issue: Contact ISNC technician if it's not a recipe error.

A.2 SQUID Magnetometry

A.2.1. Safety Precautions

1. Long pants and close-toed shoes are required to enter the SQUID room
2. Avoid the area marked with red tape as there is a small magnetic field that exists due to the electromagnet.
3. If refilling liquid He, ensure that insulated gloves are used to avoid cryogenic burns.

A.2.2. Startup

1. Take the system out of standby mode and set to the desired temperature.
2. If going to fields over 1 T, ensure that the He level is over 50%.

A.2.3. Preparing a sample

1. Cleave a piece of sample that is roughly $5 \times 5 \text{ mm}^2$.
2. This size can be used for both in-plane (IP) and out-of-plane (OOP) measurements.
3. If only IP is needed, cleave a sample that is $5 \times 6.5 \text{ mm}$, which can fit in the straw without any additional tape.
4. Cut a straw in half (use clear plastic drinking straws with no bend).
5. IP sample mounting:
 - 1) Take one straw half and rotate it so the cut end is away from the sample.
 - 2) Cut a 6 cm piece of 1 cm wide Kapton™ tape and lay it with the adhesive side facing up.
 - 3) Place the straw slightly less than halfway down the tape.
 - 4) Place the sample on its edge so it is touching the edge of the straw.
 - 5) Place the other half of the straw touching the other edge and then wrap the edges of the tape around.
 - 6) Place another 6 cm piece of tape on the top of the sample and wrap the edges.

In-plane sample mounting



6. OOP sample mounting
 - 1) Take one straw half and rotate it so the cut end is away from the sample.
 - 2) Cut a 6 cm piece of 1 cm wide Kapton™ tape and lay it with the adhesive side facing up.
 - 3) Place the straw halfway down the tape.
 - 4) Place the sample on its edge so its face is touching the edge of the straw.
 - 5) Place the other half of the straw touching the back side and then wrap the edges of the tape around.
 - 6) Place another 6 cm piece of tape on the top of the sample and wrap the edges.

Out-of-plane sample mounting



A.2.4. Loading the sample

1. In the SQUID program window, select Sample > Remove. This will vent the sample space.
2. Remove the black cap and using the threaded top portion, remove the flexible sample rod.
3. If it has another users sample on it, place the sample by the keyboard of the computer
4. Fix the sample to the bottom of the sample rod and place the small black end piece on the end of the straw to prevent the sample from falling into the instrument.
5. Insert the sample rod into the chamber and then press the small black button.

A.2.5. Centering the sample

1. Set a saturating magnetic field.
2. Center the sample position by clicking Center > RSC.
3. Initialize the transport of the sample.
4. Run a centering scan. Based on the position of the sample described in the previous section, the center should be around 3.5 cm.

A.2.6. Running a scan

1. Input desired parameters for collecting data points in the sequence file.
2. Click on Play to start SQUID measurement.

A.2.7. Refilling liquid He

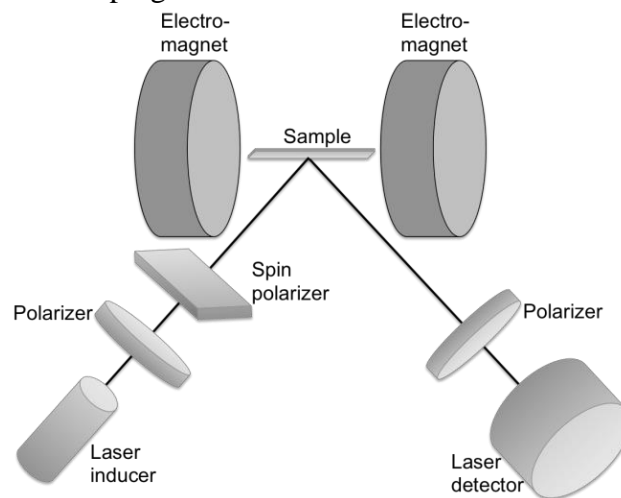
1. Check the remaining percentage of liquid helium, refill liquid helium into SQUID system if the percentage is below 50%.
 2. To refill liquid helium, firstly attach the pressured Helium gas cylinder to the liquid helium tank, in order to provide back pressure to accelerate the refilling process
 3. Vent the helium gas in the tank (note: due to the helium liquid-gas equilibrium)
 4. Vent the helium gas in SQUID and open the inlet (note: due to the helium liquid-gas equilibrium).
 5. Take off the cap on the liquid helium tank, connect the tank and SQUID with the metal tube and secure the connections (note: gloves needed to prevent frostbite).
 6. Close the venting valve and open the valve connected to helium gas cylinder on the tank.
 7. After the connection is secured, the refilling process should begin simultaneously.
 8. The refilling rate should be around 2%/min; tune the flow controller of the cylinder to attain the desired rate.
 9. Turn off the cylinder valve when the filling percentage reaches 91%, wait until the percentage slowly increases to 100%.
 10. Loosen the connections, pull out the metal tube and isolate the helium cylinder from the tank
 11. Cap the SQUID and the tank back, remembering to open the venting valve of the tank
- Notes: Temperature should be slightly increasing as He is refilled

A.2.8 In situ voltage apparatus

1. Deposit top and bottom electrodes for the sample to be measured.
2. Verify the electrical leads in the poling apparatus are connected throughout the length before attempting to attach the sample.
3. If there is a no connection, it will need to be rewired.
4. Determine where the sample should lie in the straw once the wiring is complete. If the wires are not long enough, longer pieces can be cut and attached to achieve this
 - 1) High voltage, non-magnetic wire is available in the SQUID room.
5. Cut one short length of black wire and one short length of white wire and strip both ends
6. Attach two white (+ V) wires, one from the poling sample holder and one of the short lengths, to the top side of the sample using Kapton™ tape. Verify the connection with a multimeter.
7. Repeat step 5 with the back side of the sample with black (ground) wires.
8. Insert the sample into a straw and carefully load into the SQUID.
9. Attach the electrical leads from the high-voltage power supply and run the desired scans.

A.3 Magneto-optic Kerr Effect (MOKE) spectroscopy

1. Before turning on the electromagnets, make sure that they are fastened as tightly as possible to prevent the poles from pulling towards each other due to strong attractive forces.
2. Fix the sample onto sample holder and place the sample holder in between the two electromagnets (*note: be careful not to contact the holder with the electromagnet*).
3. Turn on the laser beam by turning the key on the laser control box.
4. Setup the MOKE measurement equipment on the laser table as shown below, align the laser inducer, polarizer, spin polarizer and laser detector properly.
5. On the electromagnet power supply, turn on the primary power switch of the electromagnets first and then turn on the switch for the individual electromagnet.
6. Adjust the location and angle for the detector to detect the reflected laser beam, if the detector is aligned properly, the intensity of the in-phase reflected light on the lock-in amplifier should be reasonably high (*note: the bar should be around 50%*) and at the same time, the out-of-phase reflected light intensity should be as low as possible.
7. If the intensity of the in-plane reflected light is still low, tune the sensitivity of it by pressing the arrow bottoms in the SENSITIVITY box at the left until the reading becomes normal.
8. If the lowest value of the out-of-plane reflected light intensity is not close to zero, press the AUTO bottom in the CALIBRATE box at the right to re-calibrate it.
9. Start the MOKE measurement by setting different parameters in the MATLAB command window and press start sweeping.



A.4. Electron Spin Resonance (ESR) Spectroscopy

A.4.1. Sample insertion

1. Clean the outside of your sample. Usually wiping it with a tissue is sufficient. But take a close look to check whether the sample may need more substantial cleaning. It is of utmost importance that you keep the inside of the cavity clean!
2. Select a collet that has an appropriate size opening for your sample. Your sample should be slightly loose in the collet when the nut is not tightened down on it yet should be held firmly when the nut is tightened.
3. Remove the collet nut from the top of the cavity. Remove the blank collet and replace it with the collet you have chosen for your sample. Replace the collet nut but do not tighten it down all the way. This will allow you to adjust the position of the sample. Check to see whether there is a Teflon pedestal inserted into the bottom of the cavity. The pedestal is often used to hold a sample in the center of the cavity.
4. Hold up the sample to the front of the cavity to determine how deeply it needs to be inserted into the cavity. Once the sample height is set properly, tighten the top collet nut until it gently squeezes your sample to hold it firmly in place. Securing the sample firmly in the collet will reduce microphonic generated noise.

A.4.2. Manual cavity tuning

1. Select MW (Microwave Bridge Control) on the toolbar.
2. In the MW window, select TUNE.
3. Set the attenuation to 25 dB. Select TUNE and adjust the FREQUENCY slider to place the resonant dip in the center of the display.
4. Adjust the SIGNAL PHASE slider to maximize the depth of the tuning dip and to make the dip look as symmetric as possible.
5. Select OPERATE. If the needle in the AFC meter jumps to either edge, you will have to go back to TUNE and center the dip more accurately. Once the AFC meter is OK, re-center the needle by carefully adjusting the FREQUENCY slider.
6. Adjust the iris to center the needle of the diode meter.
7. Set the microwave attenuation to 50 dB. You may find it necessary to adjust both the AFC frequency and the iris in order to keep the AFC and diode meters from going into the red zones as you change the microwave attenuation.
8. With the microwave attenuation at 50 dB, adjust the bias to center the diode meter rather than using the iris. Increase the microwave power by reducing the attenuation. Adjust the iris and AFC frequency to keep both the diode and AFC meters are centered.
9. Repeat the iris and AFC adjustments as necessary until you reach an attenuation setting of 10 dB.
10. At 10 dB of microwave attenuation, adjust the signal phase to maximize the diode current. An increase in diode current means that the diode meter will move to the right.
11. Adjust the iris to center the diode current.
12. You should now be able to adjust the microwave attenuation between 10 dB and 50 dB with virtually no change in either the AFC or diode meters.
13. Adjust the microwave attenuation for the desired microwave power to be used for the experiment. For best stability, leave the system in TUNE or OPERATE for about 30 minutes before acquiring data.
14. Close the MW window.

A.4.3. Acquiring a spectrum

1. Create a new Spectrum Window, if necessary. This is the first icon in the tool bar.
2. Open the Experiment Parameter dialog box. Adjust the parameters as necessary.
3. Close the Experiment Parameter dialog box.
4. To acquire a spectrum, select the RUN icon. The acquired spectrum should appear in the spectrum window.

A.4.4. Sample removal and shutdown

1. Open the Microwave Bridge Control dialog box. Switch the bridge to STANDBY.
2. Close the dialog box. Loosen the collet and remove the sample from the cavity.
3. Replace the sample collet with a blank collet to help keep the microwave cavity clean.
4. Open the Interactive Spectrometer Control window, which appears as an **I** in the tool bar.
5. Set the Sweep Width to zero. Then set the Center Field to zero.
6. Choose File in the menu bar and then Exit.

A.4.5. Optimizing parameters

1. Before optimizing parameters allow time for the spectrometer to warm up and stabilize. Retune if necessary.
2. Carefully position your sample in the cavity.
3. Set the center field and spectral width such that the spectrum will fit in the spectrum window.
4. Adjust the receiver gain to see all the details of your spectrum. Increasing the conversion time will help resolve weak lines in the presence of intense lines. However, longer conversion times result in longer sweep times.
5. A longer time constant will help filter out noise. However, too long of a time constant can also filter out signals.
6. Select a sufficient number of data points to fully resolve your spectrum. Be aware that increasing the "Resolution in X" will increase your scan time.
7. If a "dip" in the peaks is observed, it is likely that the attenuation is too low (high power) and needs to be reduced.

A.4.6. *In situ* poling.

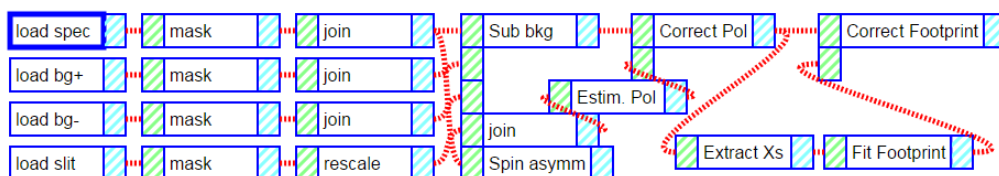
1. Deposit top and bottom electrodes for the sample to be measured.
2. Attach a 6 inch length of high-voltage, non-magnetic, white-coated wire to the top of the sample with Kapton™ tape.
3. Attach a 6 inch length of high-voltage, non-magnetic, black-coated wire to the bottom of the sample with Kapton™ tape.
4. Insert the wired sample into a 4 mm OD ESR tube and run the wires to the high-voltage power supply.
5. Apply the desired voltage and repeat the tuning procedure described above before taking a measurement.

B. Data Fitting and Extraction

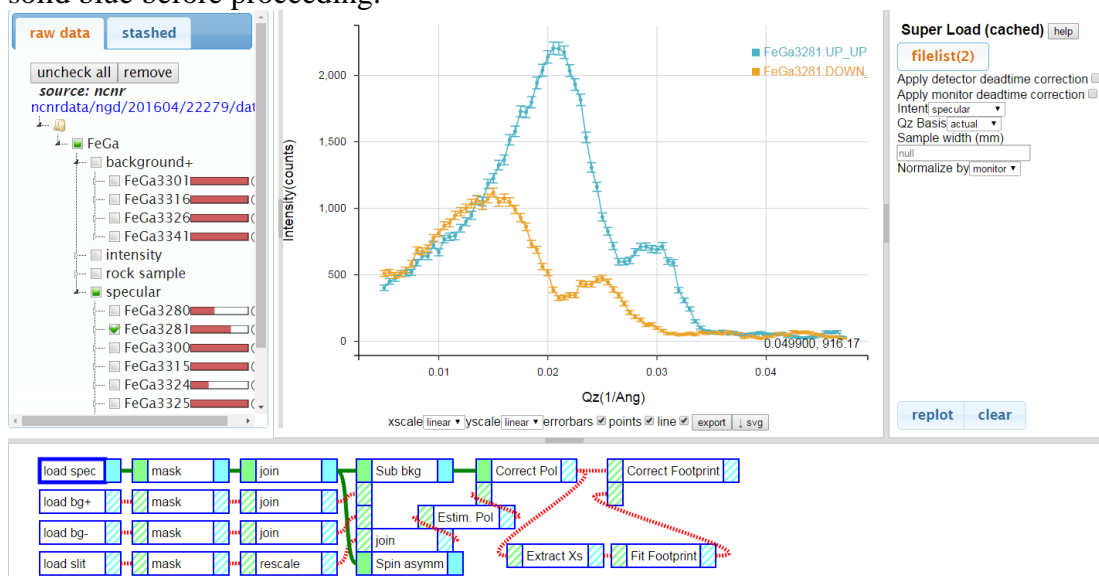
B.1. Polarized Neutron Reflectivity

Polarized neutron reflectivity data requires fitting to a physical model to physical model before information can be gleaned from the results. Before the fitting, the data must be reduced, that is, to linearize the portion of the spectra before the Q-value corresponding to the critical edge. This is the point at which neutrons will begin reflecting from the surface of the sample. This is done through NIST's website, where all scans taken can be accessed remotely and then processed within a browser window. Once this is accomplished, the physical fitting process is done using REFL1D software.

B.1.1. Data Reduction



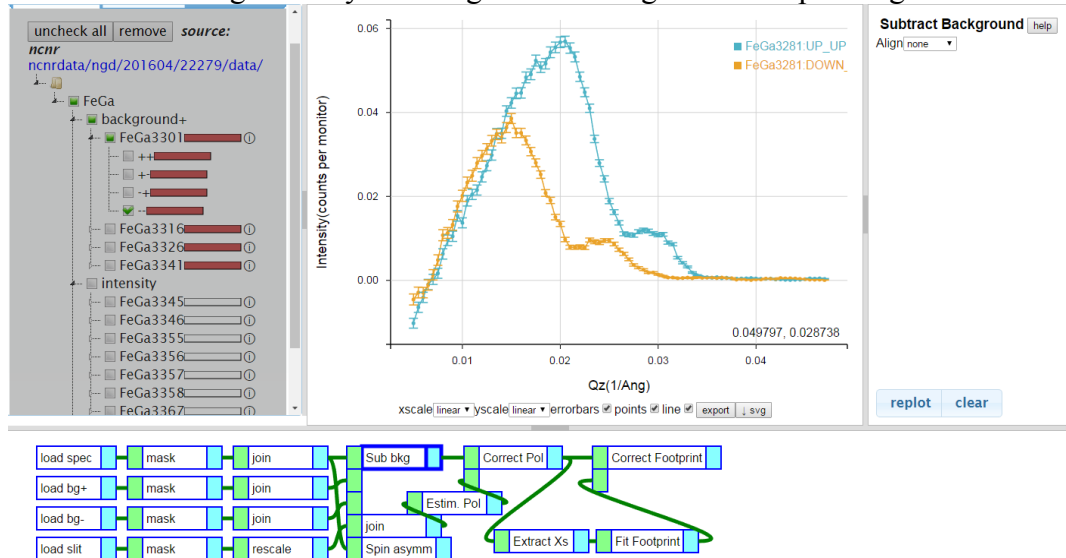
1. Access dataset via the corresponding link and the experiment ID number: http://h3.umd.edu/reflweb/web_reduction_filebrowser.html
2. Select the relevant data file from the dropdown menu from “specular”. Make sure to select “Monitor” under the “Normalize” drop down menu on the right. For each step, once the file is loaded, press the blue box on the right hand side, or ensure that it turns solid blue before proceeding.



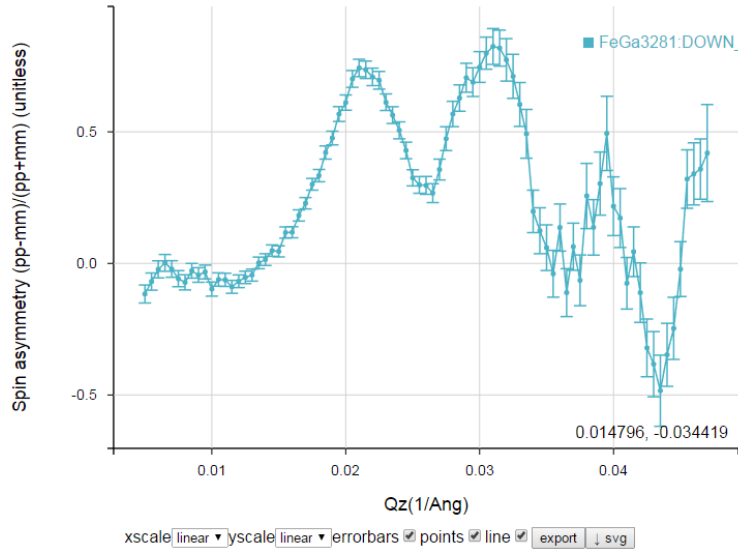
3. Each set of scans needs to have the background removed, which is determined before each run in all flipper configurations, that is, U-U, D-D, D-U, and U-D. Select

“background+” then the appropriate file. Make sure the Qz basis is the detector. Repeat the same procedure for “background-“. For both cases, there should only be one background scan or else an error will occur.

4. Select “load slit” and select the appropriate file from the dropdown under “intensity”. Make sure to only load the specific slit scan and select “Monitor” under the “Normalize” drop-down menu on the right side.
5. The second column, “mask”, is where points for the spec, background and slit can be masked so they do not skew the reduction. Repeat this for each dataset as necessary
6. The third column, join, where the masked points will be removed from the respective files. Select this for each portion.
7. Subtract the background by selecting the “Sub bkg” box then pressing the blue box.



8. Select “join” in the fourth column, then press the blue box.
9. Select “Spin asymm” and press the blue box to generate a plot of spin asymmetry between the two spectra.



10. Select “Estim Pol” to have the program estimate the polarization of the polarizing supermirror and select clip efficiency to automatically ignore points where the flipper efficiency was not high enough. 0.9 is the minimum value for this.

11. Select “Correct Pol” to adjust the spectra accordingly.

12. Select “Correct Footprint” to remove the portion of the scan representing the critical edge.

13. Export the .refl file

B.1.2. Generating Python Script

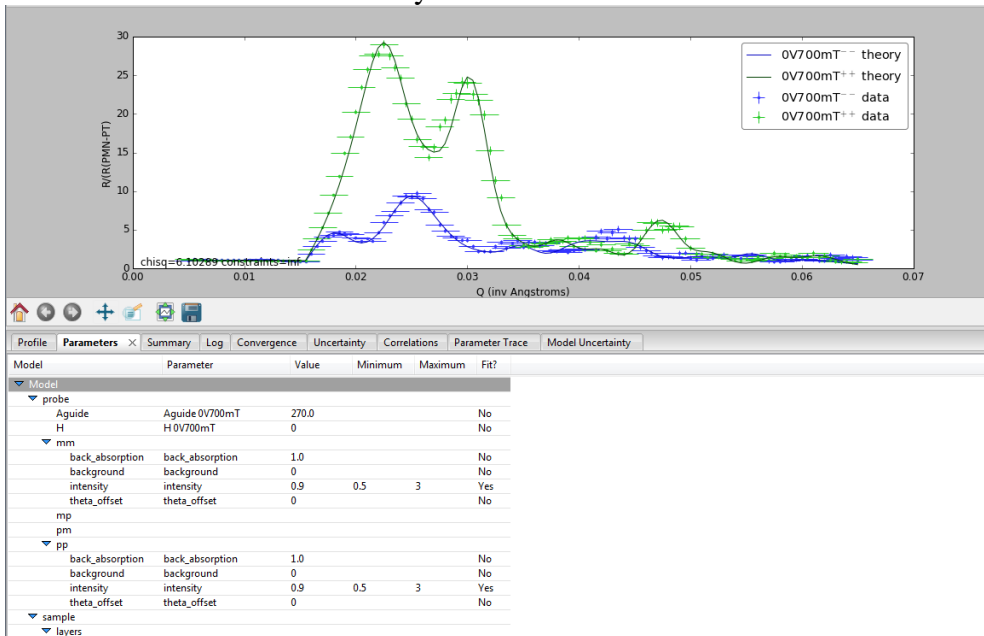
1. Upload the .refl file to the following website to enter structural information to create the Python file that will be used to do more advanced fitting.

https://www.ncnr.nist.gov/instruments/magik/calculators/calcR_mag_d3_dark.html

2. Enter the values for nuclear SLD and magnetic SLD as well as the layer thicknesses. This will change the spectra.
3. Generate the Python script.

B.1.3. Fitting the data with the physical model

1. Download the Refl1D software from the NIST website
<https://ncnr.nist.gov/instruments/pbr/refl1d-0.7.9ag-win32.exe>
2. Run the software and load the Python file



3. Depending on the scan being fitted, each parameter can be varied or fixed independently to achieve the optimal fit.
4. If fitting a non-spin flip measurement, fix the magnetization angle, θ , at 270.
5. If fitting a spin-flip measurement, let the magnetization angle rotate.

B.2 Magnetostriction

Magnetostriction is extracted from magnetic hysteresis measurements taken with and without applied strain. The difference in the area of the hysteresis loops is quantified and correlated to a saturation magnetostriction.

```

function [lambda_s,E_aniso,Hk] = calc_lambda_s(H,M,Hstr,Mstr,E,eps)
%CALC_LAMBDA_S Calculates saturation magnetostriction.
% [LAMBDA_S,E_ANISO,HK] = CALC_LAMBDA_S(H,M,HSTR,MSTR,E,EPS),
% given two volume normalized and linearly corrected magnetic
% hysteresis loops of an unstrained (H, M) and strained
% (H_str, M_str) sample, along with the applied strain and the
% material's Young's modulus, E, will calculate the saturation
% magnetostriction, lambda_s, as
% lambda_s = mu_0*Ms*Hk/(3*eps*E)
% where mu_0 is the permeability of free space, Ms is the
% saturation magnetization, eps is the applied strain, and Hk is
% the effective anisotropy field, calculated as
% Hk = E_aniso/(mu_0*Ms)
% where E_aniso is the anisotropy energy upon magnetization
% along a magnetic hard axis (M_str vs H_str), calculated as
% E_aniso = integral(mu_0*H*dM) from 0 to Ms
% and corrected by subtracting the same quantity except along
% the magnetic easy axis (M vs H).
%
% In order to approximate the anhysteretic magnetization curve,
% each half loop of the magnetization curve is horizontally
% shifted so that it goes through the origin, and the average of
% these two curves is used to calculate the anisotropy energy.
%
% H, M, and E are assumed to be in units of Oe, emu/cc, and GPa,
% respectively, and eps is assumed to be given as an absolute
% value (not in  $\mu\epsilon$ ). All output is given in SI (MKS) units.

% make sure corresponding vectors are the same length
if length(H) ~= length(M)
    error('ERROR: H and M must be the same size');
end
if length(Hstr) ~= length(Mstr)
    error('ERROR: H_strain and M_strain must be the same size');
end

% make all input vectors vertical
if ~iscolumn(H)
    H = H';
end
if ~iscolumn(M)
    M = M';
end
if ~iscolumn(Hstr)
    Hstr = Hstr';
end
if ~iscolumn(Mstr)
    Mstr = Mstr';
end

% convert to MKS units
% 1 Oe = 79.58 A/m
% 1 emu/cc = 1000 A/m
H = 79.58*H;
Hstr = 79.58*Hstr;
M = 1000*M;
Mstr = 1000*Mstr;
E = 10^9*E;

% ensure M-H loop fully saturates in both directions
if -min(M) < 0.95*max(M) || -min(M) > 1.05*max(M)
    warning('Min(M) and max(M) are of unequal magnitude');
end

```

```

end
if -min(Mstr) < 0.95*max(Mstr) || -min(Mstr) > 1.05*max(Mstr)
    warning('Min(Mstr) and max(Mstr) are of unequal magnitude');
end
% ensure strained and unstrained curves have similar Ms
if max(M) < 0.95*max(Mstr) || max(M) > 1.05*max(Mstr)
    warning('Strained and unstrained curves have different Ms');
end

% determine Ms
Ms = max([max(M) max(Mstr)]);

% separate hysteresis loop into regions of increasing/decreasing
% x values
[H_dec, M_dec, H_inc, M_inc] = separate_hysteresis(H,M);
[Hstr_dec,Mstr_dec,Hstr_inc,Mstr_inc] = ...
    separate_hysteresis(Hstr,Mstr);

% fit each half loop with a user defined function
f_MH_dec = fit_MH_curve(H_dec,M_dec);
f_MH_inc = fit_MH_curve(H_inc,M_inc);
f_MHstr_dec = fit_MH_curve(Hstr_dec,Mstr_dec);
f_MHstr_inc = fit_MH_curve(Hstr_inc,Mstr_inc);

% approximate anhysteretic magnetization curve
% shift each half loop through the origin and take their average
f_MH_dec_s = force_through_origin(f_MH_dec);
f_MH_inc_s = force_through_origin(f_MH_inc);
f_MH_anhys = @(x) (f_MH_dec_s(x)+f_MH_inc_s(x))/2;

f_MHstr_dec_s = force_through_origin(f_MHstr_dec);
f_MHstr_inc_s = force_through_origin(f_MHstr_inc);
f_MHstr_anhys = @(x) (f_MHstr_dec_s(x)+f_MHstr_inc_s(x))/2;

% plot approximated anhysteretic M-H curves
figure;
H_plot = min(H):max(H)/1000:max(H);
Hstr_plot = min(Hstr):max(Hstr)/100:max(Hstr);
plot(H,M,'k-',Hstr,Mstr,'r-',H_plot,f_MH_anhys(H_plot),'k--', ...
    Hstr_plot,f_MHstr_anhys(Hstr_plot),'r--', ...
    H_plot,max(M)*ones(size(H_plot)),'k:', ...
    Hstr_plot,max(Mstr)*ones(size(Hstr_plot)),'r:');
xlabel('Magnetic Field [A/m]');
ylabel('Magnetization [A/m]');

% calculate the work done in the approximated anyhysteretic curves
% W = integral(H*dB) from 0 to Bs
% B = mu_0*(M+H)
% => dB = mu_0*dM at constant H
% W = mu_0*integral(H*dM) from 0 to Ms
W_unstrained = mag_work(f_MH_anhys,max(H),max(M));
W_strained = mag_work(f_MHstr_anhys,max(Hstr),max(Mstr));

% calculate E_aniso = W_strained - W_unstrained
E_aniso = W_strained - W_unstrained;

% calculate Hk
% Hk = E_aniso/(mu_0*Ms)
mu_0 = 4*pi*10^-7; % SI units
Hk = E_aniso/(mu_0*Ms);

% calculate lambda_s

```

```
% lambda_s = mu_0*Ms*Hk/(3*eps*E)
%           = E_aniso/(3*eps*E)
lambda_s = E_aniso/(3*eps*E);

end
```

Bibliography

- Abo, G. S., Y. K. Hong, J. Park, J. Lee, W. Lee and B. C. Choi (2013). "Definition of Magnetic Exchange Length." Ieee Transactions on Magnetics **49**(8): 4937-4939.
- Amiri, P. K. and K. L. Wang (2012). "Voltage-Controlled Magnetic Anisotropy in Spin Devices." SPIN **02**(03): 1240002.
- Astrov, D. N. (1961). "Magnetoelectric Effect in Chromium Oxide." Soviet Physics JETP-USSR **13**(4): 729-733.
- Battogtokh, J., S. Kang, Y. Chao, M. J. Wagner, M. Brandys, A. C. Buechele, I. L. Pegg and J. Philip (2009). "Synthesis and characterization of FeGa nanowires." Journal of Applied Physics **105**(7).
- Butera, A., J. Gomez, J. L. Weston and J. A. Barnard (2005). "Growth and magnetic characterization of epitaxial Fe₈₁Ga₁₉/MgO (100) thin films." Journal of Applied Physics **98**(3).
- Cao, H., P. M. Gehring, C. P. Devreugd, J. A. Rodriguez-Rivera, J. Li and D. Viehland (2009). "Role of Nanoscale Precipitates on the Enhanced Magnetostriction of Heat-Treated Gallenol (Fe_{1-x}Ga_x) Alloys." Physical Review Letters **102**(12).
- Cullity, B. D. and C. D. Graham (2009). Introduction to magnetic materials. Hoboken, N.J., IEEE/Wiley.
- Engdahl, G. r. (2000). Handbook of giant magnetostrictive materials. San Diego, CA, Academic Press.
- Fullerton, E. E., J. S. Jiang and S. D. Bader (1999). "Hard/soft magnetic heterostructures: model exchange-spring magnets." Journal of Magnetism and Magnetic Materials **200**(1-3): 392-404.
- Geller, S. and M. A. Gilleo (1957). "The Crystal Structure and Ferrimagnetism of Yttrium-Iron Garnet, Y₃Fe₂(FeO₄)₃." Acta Crystallographica **10**(12): 787-787.
- Hanson, M., O. Kazakova, P. Blomqvist, R. Wappling and B. Nilsson (2002). "Magnetic domain structures in submicron-size particles of epitaxial Fe (001) films: Shape anisotropy and thickness dependence." Physical Review B **66**(14): 144419.
- Hayakawa, K. W. a. S. (1992). Handbook of Sputter Deposition Technology: Principles, Technology and Applications. Park Ridge, NJ, Noyes Publications.
- Hill, C. B., W. R. Hendren, R. M. Bowman, P. K. McGeehin, M. A. Gubbins and V. A. Venugopal (2013). "Whole wafer magnetostriction metrology for magnetic films and multilayers." Measurement Science & Technology **24**(4).
- Hudson, J., S. C. Busbridge and A. R. Piercy (1998). "Magnetomechanical coupling and elastic moduli of polymer-bonded Terfenol composites." Journal of Applied Physics **83**(11): 7255-7257.

Hufner, S. and G. K. Wertheim (1975). "Multielectron Effects in Xps Spectra of Nickel." Physics Letters A **51**(5): 299-300.

Jensen, G. H. S. L. H. (1989). X-Ray Structure Determination: A Practical Guide. Hoboken, NJ.

Jin, H. M., D. S. Sun, C. X. Gao and H. Kim (2007). "Inverted hysteresis loops: Experimental artifacts arising from inappropriate or asymmetric sample positioning and the misinterpretation of experimental data." Journal of Magnetism and Magnetic Materials **308**(1): 56-60.

Kay, E. (1964). "Structural + Magnetic Properties of Sputtered Nife Films Grown in Dc Discharge Environment." Journal of Applied Physics **35**(10): 2936-&.

Kittel, C. (2004). Introduction to Solid State Physics. Hoboken, NJ, Wiley.

Labanowski, D., A. Jung and S. Salahuddin (2016). "Power absorption in acoustically driven ferromagnetic resonance." Applied Physics Letters **108**(2): 022905.

Liu, Y., L. F. Chen, C. Y. Tan, H. J. Liu and C. K. Ong (2005). "Broadband complex permeability characterization of magnetic thin films using shorted microstrip transmission-line perturbation." Review of Scientific Instruments **76**(6).

Liu, Y. Z., Y. Q. Wu, M. J. Kramer, Y. Choi, J. S. Jiang, Z. L. Wang and J. P. Liu (2008). "Microstructure analysis of a SmCo/Fe exchange spring bilayer." Applied Physics Letters **93**(19).

Lou, J., R. E. Insignares, Z. Cai, K. S. Ziemer, M. Liu and N. X. Sun (2007). "Soft magnetism, magnetostriction, and microwave properties of FeGaB thin films." Applied Physics Letters **91**(18).

Lou, J., M. Liu, D. Reed, Y. H. Ren and N. X. Sun (2009). "Giant Electric Field Tuning of Magnetism in Novel Multiferroic FeGaB/Lead Zinc Niobate-Lead Titanate (PZN-PT) Heterostructures." Advanced Materials **21**(46): 4711-+.

Lou, J., D. Reed, C. Pettiford, M. Liu, P. Han, S. Dong and N. X. Sun (2008). "Giant microwave tunability in FeGaB/lead magnesium niobate-lead titanate multiferroic composites." Applied Physics Letters **92**(26).

Lueken, H. (2012). Superconducting Quantum Interference Device Magnetometry. Methods in Physical Chemistry, Wiley-VCH Verlag GmbH & Co. KGaA: 763-795.

Lupu, N., H. Chiriac and P. Pascariu (2008). "Electrochemical deposition of FeGa/NiFe magnetic multilayered films and nanowire arrays." Journal of Applied Physics **103**(7): 07B511.

Nakatani, R., T. Kobayashi, S. Ootomo and N. Kumasaka (1988). "Magnetic-Properties and Magnetic-Anisotropy Dispersion of Fe/Ni-Fe Multilayered Films." Japanese Journal of Applied Physics Part 1-Regular Papers Short Notes & Review Papers **27**(6): 937-941.

- Nan, T. X., Y. Hui, M. Rinaldi and N. X. Sun (2013). "Self-Biased 215MHz Magnetoelectric NEMS Resonator for Ultra-Sensitive DC Magnetic Field Detection." Scientific Reports **3**.
- O'Handley, R. C. (2000). Modern magnetic materials : principles and applications. New York, Wiley.
- Parkes, D. E., L. R. Shelford, P. Wadley, V. Holy, M. Wang, A. T. Hindmarch, G. van der Laan, R. P. Campion, K. W. Edmonds, S. A. Cavill and A. W. Rushforth (2013). "Magnetostrictive thin films for microwave spintronics." Scientific Reports **3**.
- Qiu, Z. Q. and S. D. Bader (2000). "Surface magneto-optic Kerr effect." Review of Scientific Instruments **71**(3): 1243-1255.
- Ranchal, R. and V. Gonzalez-Martin (2011). "Investigation on the structural and magnetic properties of sputtered TbFe(2)/Fe(3)Ga heterostructures." Journal of Applied Physics **110**(5).
- Ranchal, R., V. Gutierrez-Diez and V. G. Martin (2012). "Influence of the TbFe₂ crystallization on the magnetic and magnetostrictive properties of (Fe₃Ga/TbFe₂)(n) heterostructures." Acta Materialia **60**(4): 1840-1845.
- Rugar, D., H. J. Mamin, P. Guethner, S. E. Lambert, J. E. Stern, I. Mcfadyen and T. Yogi (1990). "Magnetic Force Microscopy - General-Principles and Application to Longitudinal Recording Media." Journal of Applied Physics **68**(3): 1169-1183.
- Shastry, S., G. Srinivasan, M. I. Bichurin, V. M. Petrov and A. S. Tatarenko (2004). "Microwave magnetoelectric effects in single crystal bilayers of yttrium iron garnet and lead magnesium niobate-lead titanate." Physical Review B **70**(6): 064416.
- Spaldin, N. A. (2003). Magnetic Materials: Fundamentals and Device Applications, Cambridge University Press.
- Spaldin, N. A. and M. Fiebig (2005). "The renaissance of magnetoelectric multiferroics." Science **309**(5733): 391-392.
- Stenning, G. B. G., L. R. Shelford, S. A. Cavill, F. Hoffmann, M. Haertinger, T. Hesjedal, G. Woltersdorf, G. J. Bowden, S. A. Gregory, C. H. Back, P. A. J. de Groot and G. van der Laan (2015). "Magnetization dynamics in an exchange-coupled NiFe/CoFe bilayer studied by x-ray detected ferromagnetic resonance." New Journal of Physics **17**.
- Stutzman, W. L. and G. A. Thiele (2013). Antenna theory and design. Hoboken, NJ, Wiley.
- Thornton, J. A. (1977). "High-Rate Thick-Film Growth." Annual Review of Materials Science **7**: 239-260.
- Ueno, M. and S. Tanoue (1995). "Magnetic-Properties of Ion-Beam Sputter-Deposited NiFe Ultrathin Films." Journal of Vacuum Science & Technology a-Vacuum Surfaces and Films **13**(4): 2194-2198.

Wang, S. X., N. X. Sun, M. Yamaguchi and S. Yabukami (2000). "Sandwich films - Properties of a new soft magnetic material." Nature **407**(6801): 150-151.

Wang, Y., J. M. Hu, Y. H. Lin and C. W. Nan (2010). "Multiferroic magnetoelectric composite nanostructures." Npg Asia Materials **2**(2): 61-68.

Windischmann, H. (1992). "Intrinsic Stress in Sputter-Deposited Thin-Films." Critical Reviews in Solid State and Materials Sciences **17**(6): 547-596.

Wolstenholme, J. F. W. J. (2003). An Introduction to Surface Analysis by XPS and AES. Hoboken, NJ, Wiley.

Wu, Y. Q., Z. X. Tang, Y. H. Xu, B. Zhang and X. He (2010). "A New Shorted Microstrip Method to Determine the Complex Permeability of Thin Films." Ieee Transactions on Magnetics **46**(3): 886-888.

Xu, J., B. Dai, Y. Ren, Y. B. Wang and X. H. Huang (2015). "Electromagnetic and microwave properties of NiFe/NiFeO multilayer thin films." Journal of Materials Science-Materials in Electronics **26**(5): 2931-2936.

Zhang, B., M. Yang, L. Liu, Q. Zhan and K. Wang (2015). "Magnetism control of FeGa/BTO thin films by Electric-field." 2015 Ieee Magnetics Conference (Intermag).

Zhang, X. S., Q. F. Zhan, G. H. Dai, Y. W. Liu, Z. H. Zuo, H. L. Yang, B. Chen and R. W. Li (2013). "Effect of buffer layer and external stress on magnetic properties of flexible FeGa films." Journal of Applied Physics **113**(17).

Zhao, P., Z. L. Zhao, D. Hunter, R. Suchoski, C. Gao, S. Mathews, M. Wuttig and I. Takeuchi (2009). "Fabrication and characterization of all-thin-film magnetoelectric sensors." Applied Physics Letters **94**(24).